Computational Models For Structural Analysis Of Retinal Images

Submitted by

Djibril Kaba

for the degree of Doctor of Philosophy

of the

Department of Computer Science
Brunel University London

September 2014

Declaration

I, Djibril Kaba, hereby declare that this thesis and the work presented in it is entirely my own. Some of the work has been previously published in journal or conference papers, this has been mentioned in the thesis. Where I have consulted the work of others, this is always clearly stated.

List of Publications

The following publications have been produced as a direct or indirect result of the research that is discussed in this thesis:

Journal Papers:

1. Djibril Kaba, Yaxing Wang, Chuang Wang, Yongmin Li, Xiaohui Liu1, Haogang Zhu and Ana G. Salazar-Gonzalez "Retina Layer Segmentation Using Kernel Graph Cuts and Continuous Max-Flow." Accepted in Optics Express.

2. Salazar-Gonzalez, Ana, Djibril Kaba, Yongmin Li, and Xiaohui Liu. "Segmentation of Blood Vessels and Optic Disc in Retinal Images." IEEE Journal of Biomedical and Health Informatics, Vol.18, No. 6, November 2014.

3. Chuang Wang, Djibril Kaba and Yongmin Li "Level Set Segmentation of Optic Discs from Retinal Images." Journal of Medical and Bioengineering, Vol. 4, No. 3, pp. 213-220, June 2015.

4. Chuang Wang, Djibril Kaba and Yongmin Li "Level Set Segmentation of Blood Vessels and Optic Disc." Under review in Journal of Medical Systems.

5. Djibril Kaba, Chuang Wang, Yongmin Li, Ana Salazar-Gonzalez, Xiaohui Liu, and Ahmed Serag. "Retinal blood vessels extraction using probabilistic modelling." Health Information Science and Systems 2, no. 1 (2014): 2.

Conference Papers:

1. Chuang Wang, Djibril Kaba, Yaxing Wang, Yongmin Li and Haogang Zhu "Automated Layer Segmentation of 3D macular Images using hybrid methods." IEEE Engineering in Medicine and Biology Society. Under review in the IEEE Engineering in Medicine and Biology Society.

2. Chuang Wang, Djibril Kaba and Yongmin Li "Level Set Segmentation of Optic Discs from Retinal Images." International Conference on Biomedical and Bioinformatics Engineering (ICBBE 2014).

3. Djibril Kaba, Ana Salazar-Gonzalez, Yongmin Li, Xiaohui Liu, Liu and Ahmed Serag "Segmentation of retinal blood vessels using gaussian mixture models and expectation maximisation." Health Information Science. Springer Berlin Heidelberg, 2013. 105-112.

4. Ana Salazar-Gonzalez, Djibril Kaba and Yongmin Li. "MRF reconstruction of retinal images for the optic disc segmentation." Health Information Science. Springer Berlin Heidelberg, 2012. 88-99. Best Paper Award.

This thesis is dedicated to my parents

Abstract

The evaluation of retina structures has been of great interest because it could be used as a non-intrusive diagnosis in modern ophthalmology to detect many important eye diseases as well as cardiovascular disorders. A variety of retinal image analysis tools have been developed to assist ophthalmologists and eye diseases experts by reducing the time required in eye screening, optimising the costs as well as providing efficient disease treatment and management systems. A key component in these tools is the segmentation and quantification of retina structures. However, the imaging artefacts such as noise, intensity homogeneity and the overlapping tissue of retina structures can cause significant degradations to the performance of these automated image analysis tools.

This thesis aims to provide robust and reliable automated retinal image analysis technique to allow for early detection of various retinal and other diseases. In particular, four innovative segmentation methods have been proposed, including two for retinal vessel network segmentation, two for optic disc segmentation and one for retina nerve fibre layers detection. First, three pre-processing operations are combined in the segmentation method to remove noise and enhance the appearance of the blood vessel in the image, and a Mixture of Gaussians is used to extract the blood vessel tree. Second, a graph cut segmentation approach is introduced, which incorporates the mechanism of vectors flux into the graph formulation to allow for the segmentation of very narrow blood vessels. Third, the optic disc segmentation is performed using two alternative methods: the Markov random field image reconstruction approach detects the optic disc by removing the blood vessels from the optic disc area, and the graph cut with compensation factor method achieves that using prior information of the blood vessels. Fourth, the boundaries of the retinal nerve fibre layer (RNFL) are detected by adapting a graph cut segmentation technique that includes a kernel-induced space and a continuous multiplier based max-flow algorithm. The strong experimental results of our retinal blood vessel segmentation methods including Mixture of Gaussian,

Graph Cut achieved an average accuracy of 94.33%, 94.27% respectively. Our optic disc segmentation methods including Markov Random Field and Compensation Factor also achieved an average sensitivity of 92.85% and 85.70% respectively. These results obtained on several public datasets and compared with existing methods have shown that our proposed methods are robust and efficient in the segmenting retinal structures such the blood vessels and the optic disc.

Acknowledgement

First of all I would like to express my sincere gratitude to my supervisors, Dr. Yongmin Li (Brunel University), Prof. Xiaohui Liu (Brunel University) for their support, patience and encouragement throughout my PhD research. I would also like thank Brunel University for the funding of my research project.

The work reported in this thesis would not have been possible without the data collected by teams from many different institutes. I would like to thank J.J. Staal and A. Hoover for publishing their retinal photographs publicly. My sincere gratitude to Dr. Ana salazar, Dr. Yaxing Wang (Tongren Hospital, Beijing, China), Dr. Haogang Zhu (Department of Optometry and Visual Science, City University, London, United Kingdom) Dr. Ahmed Sarag for their adivices and for providing the retinal images. Many people have helped by proofreading draft material and providing comments and suggestions, including Chuang Wang, Ahmed Abubakar, Mazin Abdalla, Osita Arusiuka-Hill.

I also thank all my colleages for for their support including Valeria Bo, Neda Trifonova, Mohsina Ferdous, Miqing Li, Liang Hu, Izaz Rahman, Khalid Eltayef and Ahmed Al-Madi.

I thank all my family and friends for their support including Sory Kaba and his family, Louis Drammer (Kingston social service), Raj Bajaj, Karamoko Kaba, Mamadi Kaba, Amara Toure, Amara Pendessa, Saliou Barry, family Burtscher, and family Lederer-Schnetzer and all my family and relatives in Guinea.

Finally, I would like to thank my wife Maria and my beautiful princess Naima Tenen who have been hugely supportive throughout the three years it has taken to achieve this work.

Contents

List of Figures

List of Tables

List of Abbreviations

ACC	Accuracy Rate.
AMD	Adaptive Histogram Equalisation.
Bg	Background.
CAD	Computer-Aided Diagnosis.
CNV	Choroidal Neovascularisation.
CT	Computer Tomography.
CVD	Cardiovascular Disease.
DIARETDB1	Diabetic Retinopathy Database1.
DR	Diabetes Retinopathy.
DRIVE	Digital Retinal Images for Vessel Extraction.
EM	Expectation Maximisation.
FPR	False Positive Rate.
FOV	Field of view.
Fg	Foreground.
FT	Fourier Transformation.
GCL	Ganglion Cell Layer.
GT	Ground Truth.
HSV	Hue and Saturation.
IDF	International Diabetes Federation.
ILM	Inner Limiting Membrane.
IOP	Intraocular pressure.
KNN	K-Nearest Neighbour.
MAD	Mean Absolute Distance.
MLE	Maximum Likelihood Estimators.
MRF	Markov Random Field.
MRI	Magnetic Resonance Image.
OCT	Optical Coherence Tomography.
ONH	Optic Nerve Head.
PCA	Principle Component Analysis.
PPA	Peripapillary Atropy.
RBF	Radial Basis Functions.
RGC	Retinal Ganglion Cells.
RMSE	Root-Mean Square.
RNFL	Retinal Nerve Fibre Layer.
RNFLT	Retinal Nerve Fibre Layer Thickness.
ROI	Region of Interest.
RPE	Retinal Pigment Epithelium.
SVM	Support Vector Machine.
SD-OCT	Spectral Domain Optical Coherence Tomography.
SLO	Scanning Laser Ophthalmoscope.
TD-OCT	Time Domain Optical Coherence Tomography.
TPR	True Positive Rate.

Chapter 1

Introduction

Recently, much of the research in retinal structures analysis has been deployed in retinal image analysis for diagnosis and prevention of ocular diseases including glaucoma and age-related macular degeneration, the third and the first most common causes of vision loss in the developed world. These techniques are also used in the diagnosis of a number of systematic disorders such as diabetes retinopathy, the second most common reason of blindness in the developed world, several cardiovascular diseases such as multiple sclerosis, hypertensive retinopathy and risk of stroke. Thus retinal segmentation methods assist ophthalmologists and eye diseases experts by reducing the time required in eye screening, optimising the costs as well as providing efficient disease treatment and management systems [PP93], [EGSEB11].

Early retinal structures detection methods are defined in terms of the structures they segment. The vessel segmentation includes the pixel processing based and vessel tracking based methods [FCS+03] and the optic disc segmentation methods consist of the deformable-based and the shape-based template matching methods [CLX+13]. Even though, the use of these methods in retinal disease diagnosis has been seen to evolve swiftly in the recent years. The evaluation of the retinal structures (blood vessels, optic disc and Retinal Nerve Fibre Layer) can be complex and requires time and attention. An accurate and efficient detection of changes occurring on retinal

structures during the development of diseases remain one of the main issues in retinal image segmentation. Several segmentation algorithms, based on the early approaches, fail to extract the complete structure, due to the quality of the images (poor contrast, intensity inhomogeneity or noise). Many of these methods are also source dependent, therefore they cannot perform well on images from different sources.

This study brings together the different fields of image segmentation, image processing, data analysis and ophthalmology, along with many others such as signal processing and statistical modelling, all of which make important contributions to the extraction of the retina structures. The focus of this project is to address issues in the segmentation of the retina structures considered to be the most important indicators of retinal and cardiovascular diseases, which include:

- Accurate segmentation of retinal blood vessel network in the fundus retinal images.
- Detection and segmentation of the optic disc in the retinal photograph with no restrictions on the shapes, sizes and locations of the optic disc.
- Boundary detection of the retinal fibre layers in the optic coherence tomography (OCT) image captured around the optic nerve head for glaucomatous evolution.

The proposed methods could be used to support a non-intrusive diagnosis in modern ophthalmology for early detection of retinal diseases, treatment evaluation or clinical study.

1.1 Retinal Image Analysis and Early Detection of Retinal Diseases

At this stage, it is important to highlight the necessity of performing this research and acquire some knowledge about the retinal image analysis. The high cost associated with eye examination and the increased number of retinal photographs to be

analysed are the key motivation for the introduction of automated image analysis in modern ophthalmology. The adoption of more sophisticate retinal imaging tools in ophthalmology has dramatically increased the amount of image data produced in retinal imaging evaluation. The amount of retinal image generated by these imaging tools has overwhelmed the clinicians ability to fully and accurately evaluate it. In addition to this ever-increasing image data, clinicians are forced to perform the image analysis by hand, which can be time consuming and tedious. Often the results of this analysis are subjective and open to human error. Therefore, the need for reliable computerised techniques in retinal image analysis is substantial. This can reduce the time required for retinal imaging exams and increase the accuracy of results. Furthermore, the automated methods can allow the use of Teleophthalmology for detection and grading of retinal diseases in remote regions worldwide [GUFG+02]. Since screening and disease management processes can be different, they both need effective and reliable quantitative retinal image evaluation techniques capable of providing meaningful information of any retinal specific imaging test.

Early diagnosis and timely management of retinal diseases have been shown to prevent or reduce blindness in patients with retinal disorders such as glaucoma, age-related macular degeneration and diabetic retinopathy [BMDC00], [KMFL92], [AGS10].

During this retinal diseases detection process, the images of a patients retinas are captured either with a fundus camera or OCT imaging tools, then an automated image analysis application is used to evaluate the images in order to provide meaningful results about the condition of the patients eye.

While it is shown that early detection and timely management of retinal diseases is able to prevent loss of vision and blindness, an increasing number of patients with retinal complications such as diabetic retinopathy, glaucoma and age-related macular degeneration do not undergo any form of eye exams. This scenario is due to the costs related with the screenings and the lack of a more effective automated diagnosis method [NASC14]. Guidelines reported by the American Diabetes Association showed that over

50% of diabetes patients in US did not receive any form of exam. However the number of retinal images produced has increased with the adaption of telemedicine [CWB+07] and the deployment of more sophisticated image tools [HIF+10]. In the UK only, more than 1.7 million diabetes patients were provided with diabetic retinopathy screening between 2007−2008 [AGS10]. In addition to detecting retinal diseases, it is necessary to highlight the importance of retinal image analysis in determining risk factors associated with cardiovascular diseases. Retinal images are used to measure retinal blood vessel properties (arterial to venous diameter ratio) that can provide information about the risk for hypertension, myocardial infract or stroke [LWMW08], [AGS10].

The challenge facing modern Ophthalmology today is to provide effective and reliable automated image analysis tools to make the early diagnosis widely accessible by cutting the cost and manpower needed while maintaining a high quality of diseases detection processes.

1.2 Retinal Structures Extraction

As explained earlier, the morphology of the retina structures is the key indicator of retinal diseases as well as cardiovascular complications. Eye experts spend a great deal of time and energy to evaluate these structures in retinal photographs. However, the segmentation tools can allow an automated analysis of retinal photographs so that only images with retinal complications are reviewed by eye experts. Several segmentation methods have been developed including:

- Location and segmentation of retinal blood vessel networks.
- Location and segmentation of fovea.
- Location and segmentation of the optic disc.
- Segmentation of abnormalities (haemorrhages, neovascularisations, drusen, nerve fibre infracts, lesions ect).

This study focuses only on the segmentation of retinal blood vessel networks, optic disc and the RNFL. Many different algorithms have been published for the segmentation of these structures in recent years. These algorithms perform the segmentation based either on the pixel intensity, colour, texture or prior information about the shape and size of the retina features. It is important to note that most of these methods fail to provide a complete segmentation of the retinal structures due to the imaging artefacts such as noises, intensity inhomogeneity, the poor contrast between the retina features and the image background, the variety of the image sources or the designing of the different algorithms of the methods. All these concepts will be explained in more details in the next chapters.

The current challenges in retinal image analysis can be expressed as follows:

- Accessibility of retinal image analysis tools capable of accurately locating and segmenting retinal structures that can be affected by the diseases regardless of their shapes, sizes, locations and the image conditions (poor contrast, intensity inhomogeneity or noises) and their sources.
- Lack of quantitative indices reflecting the retina structures morphology.
- Lack of analysis tool applicable of segmenting retinal structures from different sources.
- Unavailability of efficient image analysis tools (fast in processing the images).

1.2.1 Challenges in Retinal Blood Vessel Networks Segmentation

Various retinal blood vessel segmentation methods have been implemented, but the similarities among these methods are not obvious as different terms are used for the same approaches. For example, detector correlation, kernel convolution and template matching all define the same concept. But all these methods can be classified either as pixel based approaches or as vessel tracking based approaches. An accurate segmentation of the blood vessel networks is one of the most important steps of retinal diseases

analysis. This is because the vessel tree is the starting point of many of other detection operations such as optic disc segmentation [FGR04], retinal image registration [RHdC04], retinal pathologies segmentation and quantification [JWA03]. However, an accurate segmentation of the retina blood vessel network is a complex task for many reasons including the intensity inhomogeneity, the poor contrast between the vessels and the background, the presence of noise in the image and the change in vessel width, shape and brightness.

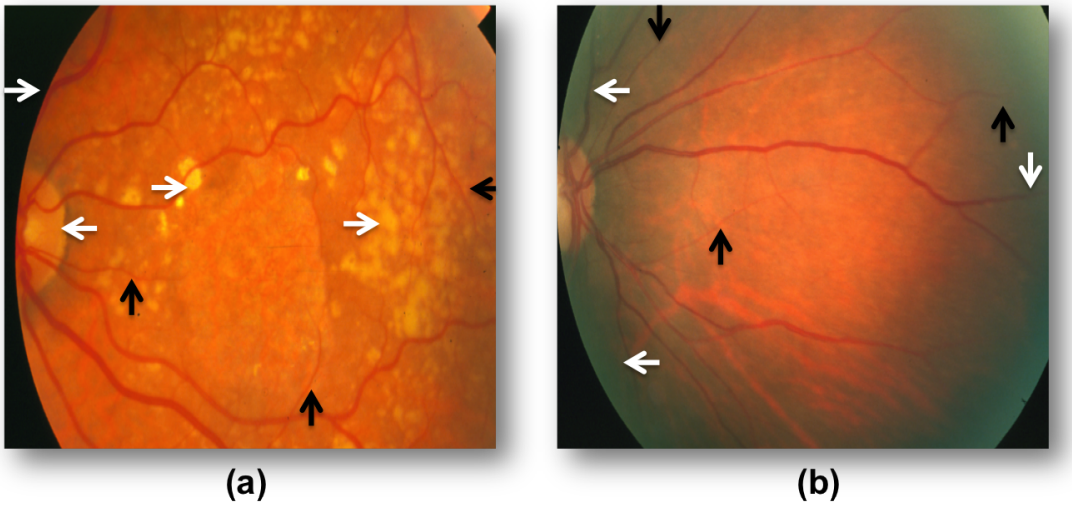

Figure 1.1: Illustration of retinal blood vessel segmentation. (a) White arrows show the boundary of the retina, the boundary of the optic disc and the pathologies, black arrows indicate narrow and low contrast blood vessels. (b) White arrows highlight the variation of the image intensity and black arrows show the thin vessels with low contrast. All the above may cause errors in vessel networks segmentation.

In addition to these factors, the presence of pathologies such exudates and lesions causes a significant degradation to the performance of the automated blood vessel segmentation techniques. Figure 1.1 shows the illustration of some challenges of the retinal blood vessel segmentation. These challenges can be summarised as follows:

- The intensity inhomogeneity of retinal images, cause an overlap between vessel pixels and background pixels intensity distribution.

- Poor contrast between the vessels and the background with some background noise.
- A wide range of vessels widths, which consist of narrow and large vessels.
- The overlapping tissues, including the optic disc, the retina boundary and pathologies cause significant degradation to the automated vessels segmentation methods.
- Narrow blood vessels often appear darker making the segmentation difficult.
- Wider blood vessels can often show some bright strip passing through the centre making difficult to automatically distinguish neighbouring vessels.

1.2.2 Challenges in Optic Disc Segmentation

Optic disc morphology is a key indicator of the presence of glaucomatous damage. The glaucomatous damage is mainly detected by identifying the changes in shape, colour or depth in the optic disc [LC03]. The optic disc detection is usually performed in two stages, the localisation of the optic disc position and the detection of the disc boundary. The optic disc segmentation methods in the literature are grouped into three major approaches, which include pixel classification based methods, deformable-based methods and template based methods [CLX+13]. We will provide more detailed explanation and limitations of the methods in the coming chapters.

An automated segmentation of the optic disc can be complicated, even impossible at times due to the following changes:

- Obstruction of the blood vessel in the optic disc region.
- Ill define boundaries of the optic disc.
- Intensity variations around the optic disc boundaries due to pathological changes and imaging artefacts.
- Variety of disc shapes and boundaries.

- Distractions caused by retinal pathologies.

Figure 1.2 shows some sample images to illustration the above conditions.

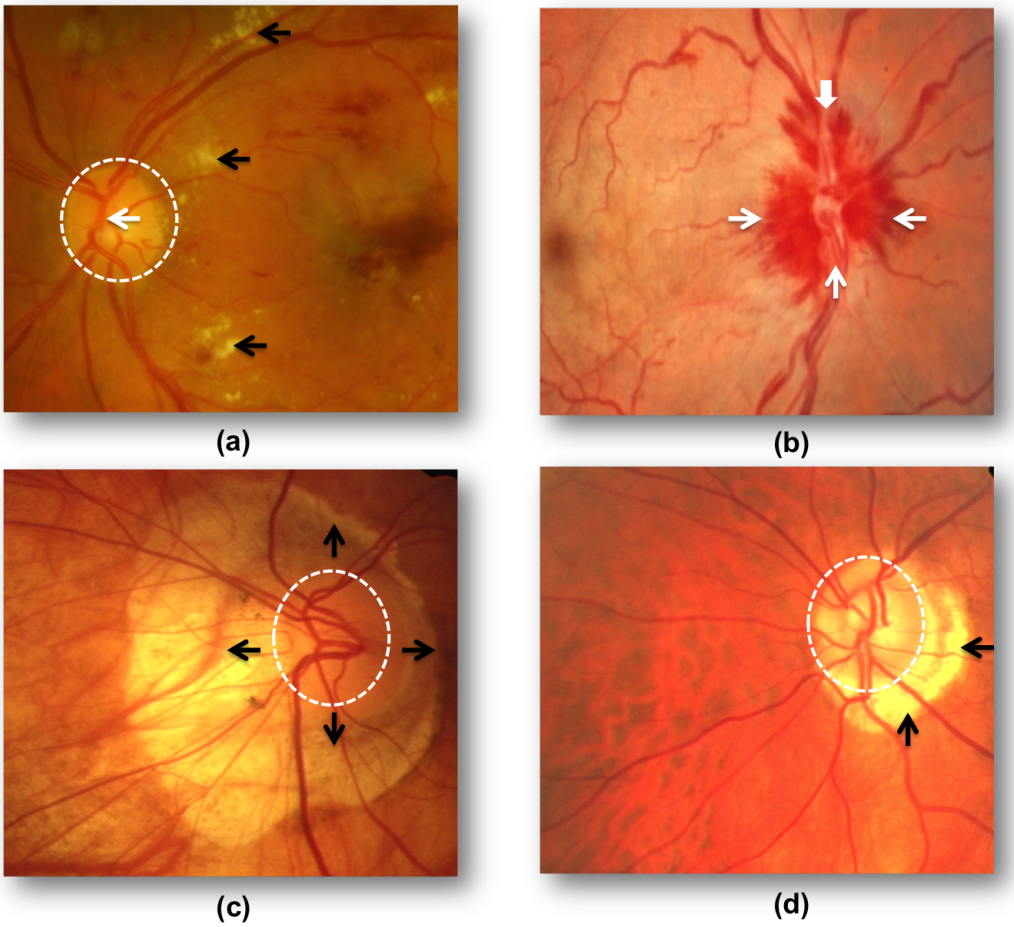

Figure 1.2: Illustration of retinal optic disc detection. (a) Dashed white circle defines the boundary of the optic disc, white arrows shows the intrusion of vessels in the optic disc region and black arrows indicate bright lesions. (b) White arrows show the optic disc completely covered by haemorrhaging. (c) Dashed white circle highlights the boundary of the optic disc, which is distorted by the swelling shown by the black arrows. (d) Ill-defined disc boundary shown by the dashed circle and intensity variation near the optic disc due to atrophy indicated by the black arrows. All of which cause errors in the segmentation.

1.2.3 Challenges in RNFL Detection

The adaptation of OCT imaging in ophthalmology has allowed direct visualisation and assessment of the retina and its different layer structures. Recently a combination of OCT imaging techniques and image analysis methods have been used in glaucomatous damage diagnosis by segmenting and measuring the RNFL thickness [MHMT10], [AGS10]. Most of the early methods were solely based on pixel intensity variation processing operations along A-scan profile [KBR01] and other segmentations techniques using image gradients, prior layer shape information and many other constraints to perform the segmentation of the layers. These methods include active contours, graph cut and machine learning approaches.

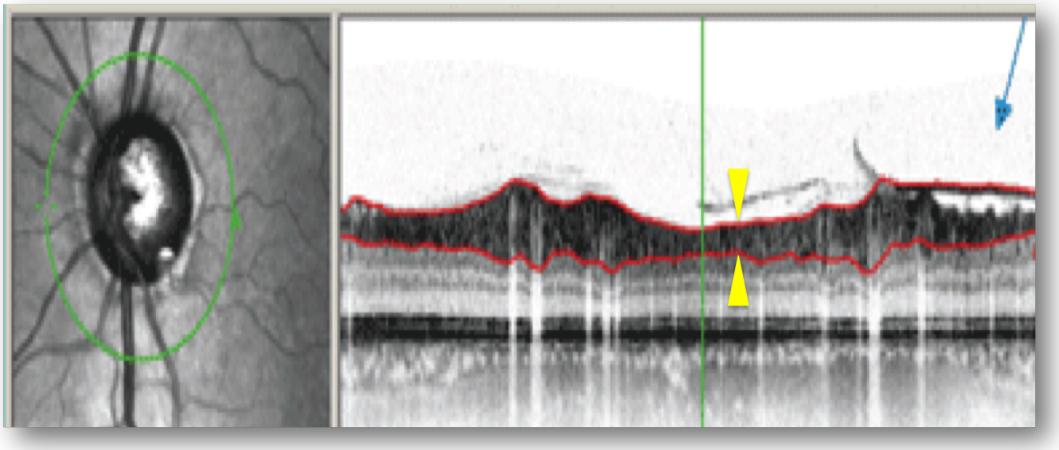

Figure 1.3: Illustration of RNFL detection in noisy OCT scan. Left: green circle indicates the scan of the retina. Right: shows the detection of the RNFL thickness indicated in yellow with the segmentation lines in red, the blue arrow highlights the segmentation error. [Sco10].

Even though, the use of OCT imaging in glaucoma evaluation has been seen to evolve rapidly in recent years, an accurate automated segmentation of the retinal structures layers can be complex and remain the main issue in the diagnosis of the retinal OCT scan. Many of the above automated methods for retinal layer detection often fail

due to the corruption of OCT scans by non-Gaussian noise [SXY99], the high variance of pixel intensity values across OCT scans [KBR01], the motion artefacts and the decrease of scan quality during the scanning operations [SSPF07]. The affect of noise and poor scanning quality on an automated RNFL detection method is shown in Figure 1.3.

1.3 Contributions

When this project began, retinal image analysis was a research topic that had already influenced a large number of medical image analysis research groups worldwide. With the deployment of more sophisticated retinal imaging systems, many segmentation algorithms have been implemented to extract the structures of the retina, known to hold some key information of the retinal and systemic diseases. These techniques have often been used to assist ophthalmologists and eye experts to perform efficient and reliable retinal disease assessment and management.

Retinal blood vessel segmentation techniques were applied on fundus retinal images to extract the vessel networks, optic disc and pathologies. The RNFL extraction methods have also been used on a variety of fundus and OCT photographs of the retina to provide more meaningful information about retinal diseases. In attempting to apply these methods to real life retinal images, noise, intensity inhomogeneity, algorithmic complexity, and many other imaging artefacts all became key obstacles to be overcome in automated retinal structures segmentation.

To tackle the above issues, the existing techniques require more robust image processing operations as well as incorporation of some prior knowledge about different retina structures. Focus was placed on noise estimation operations that were used to improve the appearance of features in the image. A careful selection and combination of processing techniques was conducted to allow more complete extraction of the different retinal structures. This research incorporates some of the previous work in image segmentation to guide the development of novel segmentation methods designed

to provide and accurately extract the structures in retinal photographs.

The work proposed in this thesis is by no means complete, but it provides the essential knowledge in segmenting the structures of the retina to allow more complete use of the retinal image analysis tools to day-to-day work in modern ophthalmology. The main contributions of this thesis can be summarised as follows:

- One of the key contributions of this study is the implementation of unsupervised techniques , which have achieved similar results as supervised techniques. Unlike many supervised retinal structures segmentation methods, which can achieve a great segmentation performance but often dependent on the image dataset and training set (manually labelled structures), our segmentation methods are capable of achieving good results in retinal photographs from different sources without the need for a specific training operation. Using our proposed methods could reduce the time and the work required for traditional supervised retinal structures segmentation.

- Removal of noise in retinal image. Imaging artefacts such noise and intensity inhomogeneity cause significant degradation to the performance of automated segmentation. Thus careful pre-processing experiments were conducted on fundus and OCT retinal photographs, to define a unique processing operation capable of reducing noise and other imaging artefacts in both type of images without corrupting the image information as seen with some mathematical image processing operators. The combination of pre-processing techniques such as bias correction, which is often used on CT images to move noise and distance transform were used to enhance the appearance of the retinal structures while keeping the image information. This process allows a more complete segmentation of the target structures.

- Incorporation of prior information about the retina structure. One of our main contributions was to incorporate prior information of the retina structures and

the flux of vectors into the graph cut energy formulation to perform the segmentation of the structures. Since the boundaries of some of the retinal structures are ill-defined, the incorporation of this knowledge into the graph energy formulation can guide the detection operations of the target structure. This allows the segmentation of thin blood vessels and provides an optimal solution during the detection of the optic disc boundaries.

- The extraction of overlapping tissues. The intrusion of retinal blood vessel into the optic disc region known as overlapping tissue has caused many of the failures seen in optic disc segmentations by breaking the disc boundaries. The proposed methods address this issue by either discriminating the blood vessels using Markov random field reconstruction or by incorporating them using the graph cut with compensation factor. We believe that both methods can be useful in other applications of the overlapping tissue segmentation.

- Accurate location of the optic disc in the fundus retinal image. The location of the optic disc is one of the key steps for the detection of its boundaries. Most the optic disc segmentation methods ipn the literature use the brightness feature of the optic disc to locate its position, this technique can falsely locate the position of the disc, when the retinal images exhibit pathologies such as bright lesions, drusen or swelling. We address this problem by adapting the method presented in [WSK+10] using segmented blood vessel networks and the intensity of the optic disc to find the convergence point of the blood vessel networks, which represents the centre of the optic disc.

- Robust detection of RNFL in the OCT scan around the optic nerve head. Since the boundaries of RNFL can be ill-defined due to the shadows of the blood vessels and the intensity variation across the scans, the proposed method detects the layers by incorporating a kernel-induced space into a graph segmentation. This maps the original scan into a higher dimensional kernel space to allow better layer

detection. Prior knowledge of the RNFL and the RPE was used to accurately detect the RPE known to be the most difficult layer to segment.

1.4 Thesis Outline

This section provides a guide to the contents of each chapter within this thesis. Each chapter is an independent section of research in its own right. They will follow the same format, which includes the detailed introduction of the problem, the explanation of the techniques used and the experimentation results. As with all traditional research, the chapters in this thesis collectively provide an evolution of ideas, following an unravelling story into the use of the computer-aided diagnosis in modern ophthalmology.

Chapter 2 provides general background knowledge that is relevant to each chapter. It includes general materials relating to the computer-aided diagnosis and the current imaging tools employed to capture the photographs of the retina. It also provides brief introduction to the eye anatomy, the retinal and systemic diseases including glaucoma, diabetic retinopathy, age-related macular degeneration and cardiovascular disorders.

Chapters 3 and 4 will introduce the segmentation of retinal blood vessel networks. Chapter 3 provides the retinal blood segmentation using the pixel processing based method, which combines the bias correction, adaptive histogram equalisation and distance transform with a probabilistic modelling algorithm to extract the vessel tree. While chapter 4 improves the vessel extraction using the graph cut segmentation technique.

Chapter 5 will introduce the detection of retinal optic disc. In this work, we provide two different methods including the Markov random field (MRF) reconstruction and graph cut with compensation factor. MRF reconstruction performs the optic disc segmentation with removing the blood vessels in the disc region, while the latter performs the same segmentation by incorporating the blood vessel using local information of the vessels pixels.

Chapter 6 was introduced to provide more efficient evaluation of glaucomatous damage in addition to the methods proposed in chapter 5. Unlike latter methods, this technique is applied on the OCT scan, which provides more detailed photography of the retina structures. The retinal layers are detected on OCT circular scans including RNFL thickness.

Chapter 7 provides discussions of the work proposed in this thesis and highlights future research directions currently under investigation.

Part I

Background

Chapter 2

Some Background

This chapter provides a thorough background of the retinal structures analysis. The literature on this particular topic is vast, but we will highlight the most relevant to this study.

2.1 A brief introduction to Retinal Image Analysis

Rapid advances in technology and its application in medical imaging have improved the quality of health care through earlier diagnosis of diseases and limiting the use of invasive treatment techniques such as surgery. Computer-aided diagnosis (CAD) has become one of the most important and widely used fields within medical imaging technology and diagnosis radiology [Doi07], [GM96], [VGtHRV01], [KXM+96], [MDC+90], [GSP+02], [FU01]. Recently the number of research publications on subjects related to CAD has significantly increased due to the demand in medical image analysis tools [Doi14]. The basic concept of CAD in modern health care systems is to use a computer algorithm to output information as a second opinion to physicians and health care specialists performing complicated diagnosis [Doi14],[Doi07]. To identify or prevent diseases affecting the brain, retina, bones, chest, breast, liver, lung, kidney and the vessel network systems.

The images of these organs are acquired through machines such as computed tomography (CT), X-rays, Magnetic resonance (MRI), ultrasound, fundus camera, and optical coherence tomography camera. The images are analysed by health professionals or image analysis algorithms in CAD to make a meaningful decision about the progress of the diseases and make treatment evaluations [Doi14]. These analysis methods are known to be non-intrusive approaches. Several research applications in the medical image analysis field have been deployed in medical care for diagnosis and prevention of diseases like breast cancer, diabetic retinopathy, glaucoma, arthritis, cerebral, tumours, kidney dysfunctions, lung diseases to cite few [Doi07],[CDV+90], [EGSEB11], [FU01], [LLS+05], [GSP+02], [SLS+05]. A key component in the CAD tools is the segmentation, quantification and registration of medical image structures but each technique may be used for a specific task, and there are no generic techniques for the wide ranges of tasks. For example various segmentation methods have been deployed for detection and quantification of different lesions in medical imaging [PP93], [EGSEB11]. These methods have helped health specialists improve the quality of the diagnosis process.

In this study, we will provide segmentation methods for detection and analysis of retinal diseases. The proposed methods could be used to support a non-intrusive diagnosis in modern ophthalmology for early detection of retinal diseases, treatment evaluation or clinical study. Before we explore different segmentation methods and the nature of research, which have been done in this review, it was important to highlight the necessity of performing this research and acquire some knowledge about the imaging tools and eye diseases we are trying to detect using some computer algorithms.

2.2 A Brief Introduction to retinal Diseases

The retina is a light sensitive layer cell at the back of the eye that generates a neural signal for vision, as seen in Figure 2.1. The function and structure of the retina allows for non-invasive observation of retinal disorders and diseases that affect blood

circulation and the brain. These diseases include glaucoma, retinal occlusion, macular degeneration, and diabetic retinopathy, hypertensive retinopathy and multiple sclerosis just to mention a few.

Before we explore different methods and the nature of research which has been done in this review, it is important to highlight the necessity of performing this research and briefly describe the eye anatomy and the diseases we are trying to detect using computer algorithms.

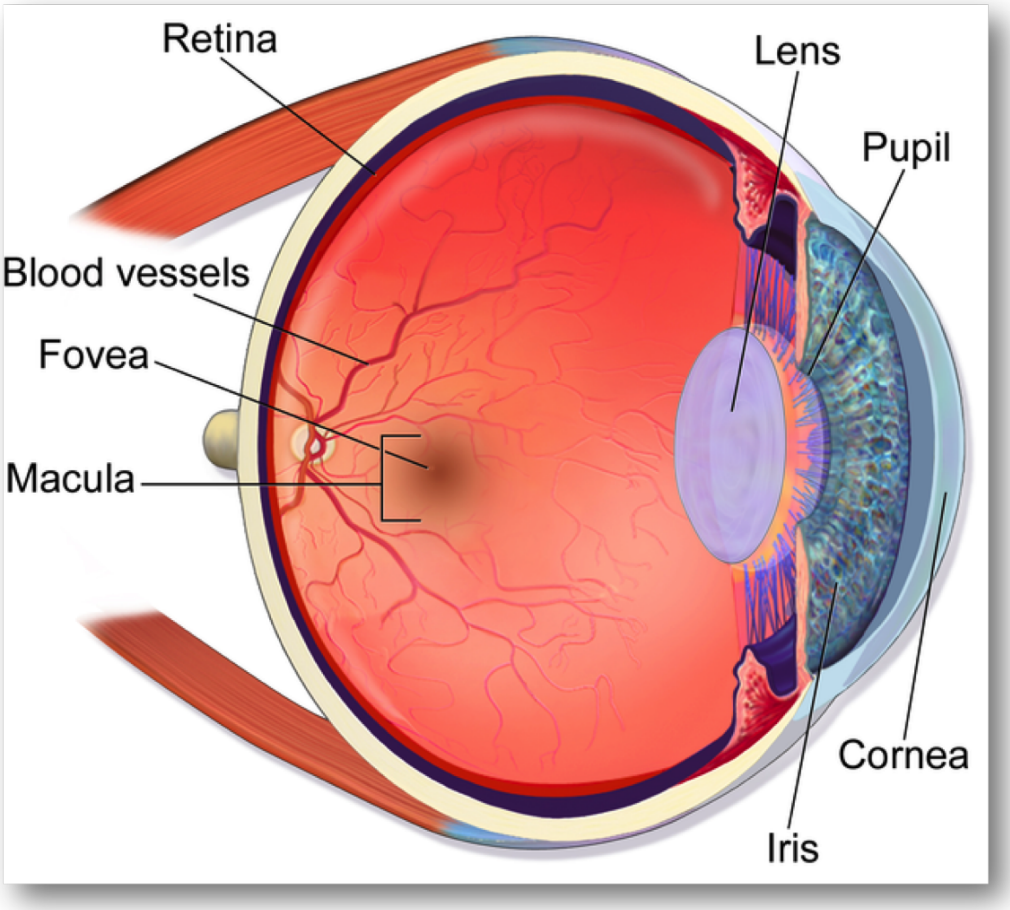

Figure 2.1: Illustration of eye anatomy showing a cross-sectional view of the eye and its structures from [wik14a].

2.2.1 Eye Anatomy

To assess and manage the progress of retinal abnormalities, it is very important to understand the function of all the different tissues of the eye. A cross-sectional view of the eye and its structures are shown in Figure 2.1. The visible parts a human eye consists of

- A transparent cornea about $8mm$ of diameter at the front of the eye, this allows the light to enter the eye.
- A white opaque sclera normally about $12mm$ of diameter is the outer layer of the eye which provides resistance to both internal and external forces and preserves the shape of the globe.
- A coloured iris (brown, green, blue or mix of these colours), which expands and contracts to let the right amount of light-ray into the eye.
- Finally a black pupil, which channels the light-ray to the lens.

When a ray of light passes through the visible parts of the eye and reaches the lens, the lens optically directs the light into the interior chamber to the vitreous before reaching the retina layer. The retina is mainly supported by the retina pigment epithelium, the choroid and the sclera. Approximately 65% of the retina blood supply passes through the choroid and 35% through the retina vasculature network [AGS10], Figure 2.2(b) shows the illustration of the retinal layers. The retina and the choroid consist of the following layers:

1. The internal limiting membrane: it separates the retina from the vitreous;
2. The retinal nerve fibre layer: axons of the ganglion cells through which the visual signal is transmitted to the visual cortex;
3. The ganglion cell layer: the nuclei or the cell bodies of the ganglion cells;

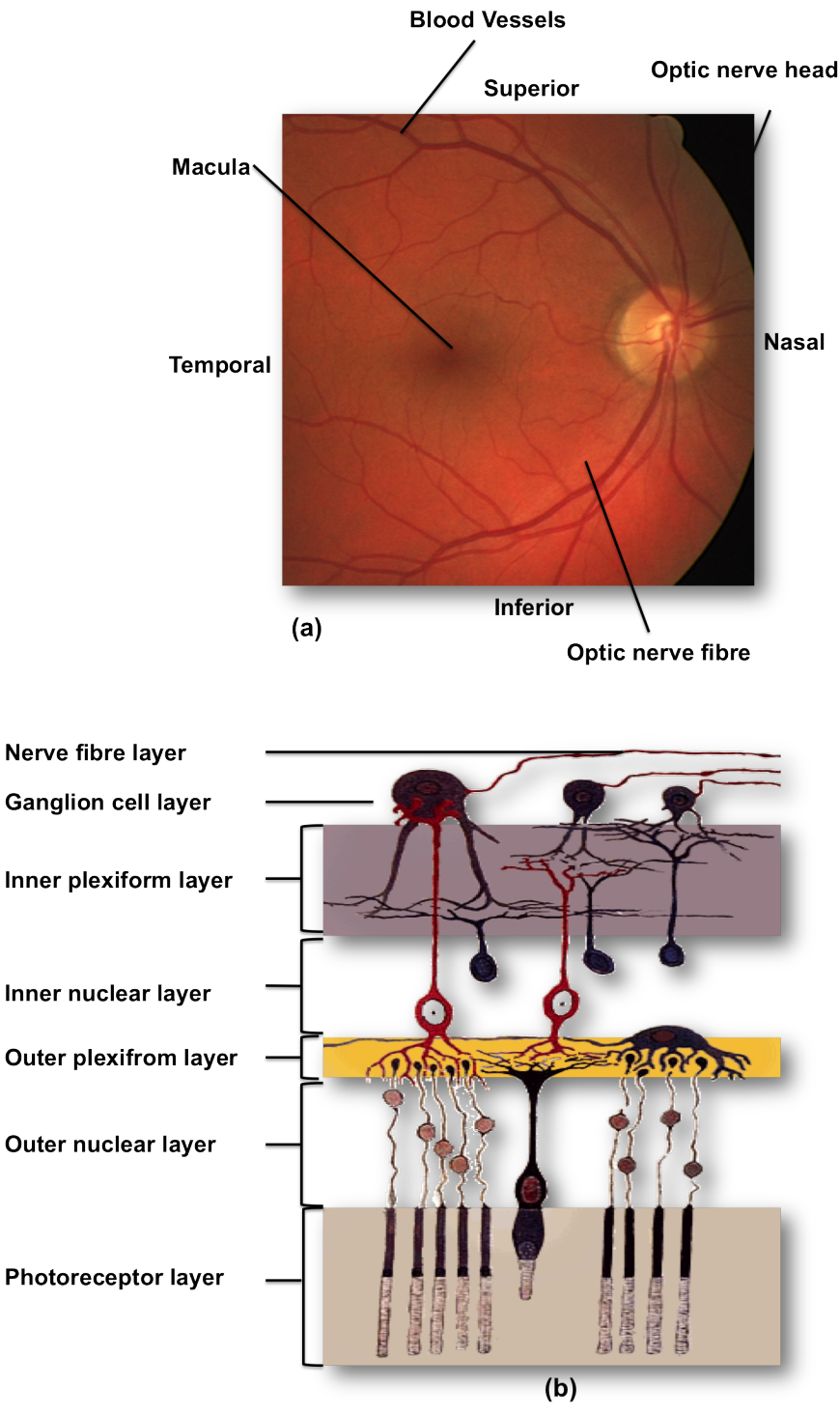

Figure 2.2: **(a)** Fundus photograph of the retina showing different structures of the retina. **(b)** Illustration of cellular layers of the retina form [Wik14b].

4. The inner plexiform layer: The axons of the bipolar cells, dendrites of the ganglion cells;
5. The inner nuclear layer: the nuclei or cell bodies of the horizontal cells, the bipolar cells;
6. The outer plexiform layer: The horizontal cell dendrites and the inner segments of the photoreceptors (rods and cones);
7. The outer nuclear layer: the cell bodies of the photoreceptors rods and cones;
8. The external or outer limiting membrane;
9. Photoreceptor, bacillary layers: the inner and outer segments of rods and cones photoreceptors;
10. The pigmented epithelium.

Below the pigmented epithelium there are 4 other layers, from the outside to the inside of the retina:

1. The Bruchs membrane: limiting the pigmented epithelium from the choroid;
2. The choriocapilaris or capillaries of the choroid;
3. The large choroid blood vessels or choroid plexus;
4. The sclera: the white part of the eye.

After passing through the anterior chamber of the eye and the retina. The light continues travelling through all the layers until it reaches the rods (the photoreceptor layers). Once at the photoreceptor layers, the luminance of the light activates the rods and the cones. This produces a chemical reaction with the cones and the rods causing a propagation of neural signal that stimulates bipolar cells. The process activates the retina ganglion cells (RGCs) and the signal passes through the axons of the ganglion

cells or retinal nerve fibre layer (RNFL) and optic nerve to reach the visual centre at the back of the brain via the optic nerve head (ONH). At this point, the neural signal undergoes further processing in the visual cortex of the brain before vision take place. At this stage it is important to provide some information about retinal diseases and the damage they cause on the structure and the function of the retina.

2.2.2 Retinal Diseases

Many diseases originate either from the eye (glaucoma, macular degeneration), cardiovascular network (hypertension, multiple sclerosis or risk of stroke) can be noticeable in the retina [AGS10]. It is estimated that 37 millions people globally are blind caused mainly by cataract, glaucoma, diabetic retinopathy and age-related macular degeneration [FR05]. A non-invasive retinal imaging techniques can be use to assess and manage many of these diseases including

Glaucoma

Glaucoma ruins the vision by damaging the optic nerve that carries visual signals to the brain and it is considered to be the second highest cause of permanent blindness worldwide [QB06] [TNPD95]. In 2002, the number of people blinded by glaucoma was projected to be 4.5 million worldwide, and this number is estimated to increase to 11.2 million by 2020 [BGLR08]. According to the World Health Organization 2020 the number of people with glaucoma will reach 79.6 million by 2020. Less than 50% of those affected by glaucoma in the developed world are not aware of their conditions due to the silent progress of the disease [QB06]. In the UK alone there are more than $500,000$ suffering from glaucoma and it is estimated that 67% of those are undetected. This number is must higher in developing countries with over 90% of people affected by glaucoma are not being aware of it [Moo14a].

Glaucomatous damage is a disease with no cure and its causes are not fully known. However some studies have shown that, glaucoma can be caused by the increase of

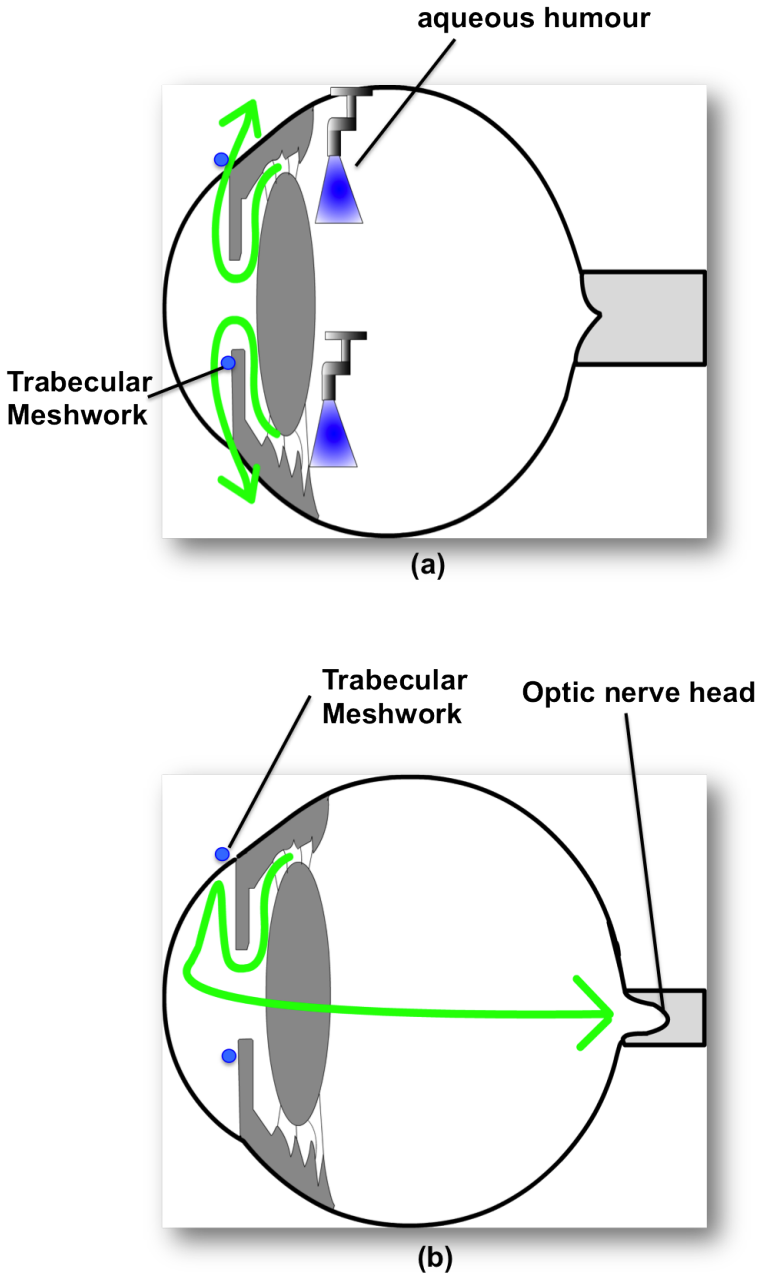

Figure 2.3: Schematic drawing of glaucomatous damage. **(a)** The aqueous humour in blue flowing around the front the eye's chamber as shown by the green arrow to the drain trabecular meshwork (blue dots). **(b)** The aqueous humour flowing into the eye's anterior chamber as the trabecular meshwork is blocked exerting pressure on the optic nerve head and damaging the nerve from [Gla13].

eye pressure, which can damage the ganglion cells and their axons and if not treated can lead to irreversible vision loss. Thus glaucomatous damage is characterized by a structure change leading to functional damage [QAG82]. The increase of the intraocular pressure (IOP) is often associated with clear watery fluid known as aqueous humour, which flows through the eye's anterior chamber to nourish tissues in the eye and keeps the eye healthy (correctly sending visual information to the brain), as illustrated in Figure 2.3(a). The IOP rises when this fluid is trapped in the eye chamber, caused by a blockage of the drainage system (trabecular meshwork) located between the iris and the cornea. This can exert a great pressure on the optic nerve head damaging the ganglion cells and their axons, see Figure 2.3(b). High IOP is known to trigger the glaucomatous damage, but several researchers have also shown that people with normal IOP may also suffer from glaucoma. In all cases high IOP is considered as a risk factor for glaucomatous damage, together with other factors such as age, high myopia and family history.

Early detection and management of glaucoma has been shown to reduce the risk of irreversible visual loss by glaucomatous damage [HLB+02] [BLHH07]. Since the glaucomatous damage directly affects the structures of the optic nerve head (ONH) by cupping the optic disc, as seen in Figure 2.4(d). The damage can be assessed through a 2-D fundus retinal photography or a 3-D structural view of the retina tissue in an OCT image. This evaluation is performed by defining the ratio of the optic disc cup and the neuroretinal rim region (cup to disc ratio) [AGS10]. A direct measurement of the retinal RNFL thickness can also provide key structural changes of the RFNL by glaucomatous damage. Moreover typical glaucoma assessments includes tonometry, perimetry, ophthalmoscope, gonioscopy and pachymetry. All these examinations manage glaucoma with IOP lowering drops or through surgery in some refractory conditions. Further information about glaucoma can be found in [QB06] and [BLHH07].

Diabetes

Diabetic retinopathy is an ocular manifestation of diabetes which causes damage to the retina. Diabetes mellitus is a chronic disease caused by a high level of sugar (plasma glucose over 7.0 mmol/l) in the blood, which damage blood vessels, nerve cells as well as the kidneys, heart, brain and the retina (diabetic retinopathy) [AGS10]. American diabetes association [WRG+04] has estimated the number of people living with diabetes to be 171 million worldwide in 2000, approximately 2.8% of the world population. This number will rise to 366 million by 2030 around 4.4% of the world population. More research from the International Diabetes Federation (IDF) has estimated the number of people living with diabetes to be 382 million worldwide in 2013, this number will rise to 592 million in 2035 [ABC+13]. The causes of diabetes are not fully known but they are partially linked to life style, unhealthy diet, obesity, genetic background and lack of exercise.

There are mainly two types of diabetes (type 1 and type 2). Type 1 diabetes is generally found in young adults or children, known as Juvenile or insulin dependent diabetes. According to figures approximately 1 in 300 people in the UK live with type 1 diabetes. This chronic disease can progress very rapidly sometimes within days or weeks since the pancreas stops producing insulin. Type 1 diabetes is considered to be an autoimmune disease, as the patients immune system produces antibodies to attack the beta cells in the pancreas responsible of making the insulin in the body [HSKG13], [ADD+98] , this reaction in the body of the patient can destroy the beta cells. It is understood that a reaction in the body triggers the immune system to produce those antibodies. However the cause of this phenomenon is not known to date but the results of some studies have shown that a virus is responsible for triggering the immune system into creating the antibodies to destroy the cells that generate insulin and type 1 diabetes is often linked to different genetic and environmental factors [HSKG13], [ADD+98]. The deficiency of insulin secretion means that type 1 diabetes patients require continuous insulin replacement therapy. Unlike type 1, type 2 diabetes often affects people over

the age of 40, but can sometimes develop in younger people. About 90% of all diabetes cases are of type 2 and it is common in people who are overweight [MPLK11]. Type 2 diabetes develops gradually and the patients still produce insulin but not enough for all the bodys needs or the cells in the body are unable to properly use the insulin made by the pancreas. This is known as no-insulin-dependent diabetes or maturity onset [OKS+82], [RBDO76]. Unlike type 1 diabetes, in type 2 diabetes patients often do not need insulin treatment to survive. The causes of type 2 diabetes are various and this type of diabetes is likely to decrease in the future since the identification of individual pathogenic processes and genetic deficiencies allows better distinction among them. Nevertheless patients with this type of diabetes are generally obese and obesity alone can causes some level of insulin- resistance [ADD+98],[KGG+81]. Usually type 2 diabetes develops unnoticed for many years as the hyperglycemia progresses gradually at the earlier stages and it is not sufficiently severe for the patients to notice symptoms of the diabetes [Zim92]. However patients can be at high risk of having microvascular and macrovascular complications [AS95], which can also result in diabetic retinopathy.

Diabetic retinopathy (DR) is considered to be the second most common cause of vision loss in the developed world. DR damages the blood vessel networks in the retina, causing an insufficient blood supply in the retina, which can lead to conditions such as the proliferative diabetic retinopathy (bleeding of new blood vessels) and diabetic macular edema (damage of photoreceptors) [AGS10], as seen in Figure 2.4(c).

Every patient living with diabetes is at risk of developing DR. The WHO estimated that over 75% of patients with diabetes for more than 20 years will develop some form of DR [Org06]. With the increases in number of people with diabetes, the DR is likely to become the leading cause of vision loss worldwide in the next 20 years with severe impacts in the poorest countries [ABC+13]. However vision loss or blindness cause by DR can be prevented through early diagnosis of the disease using non-invasive retinal imaging techniques [KS00], [LWMW08].

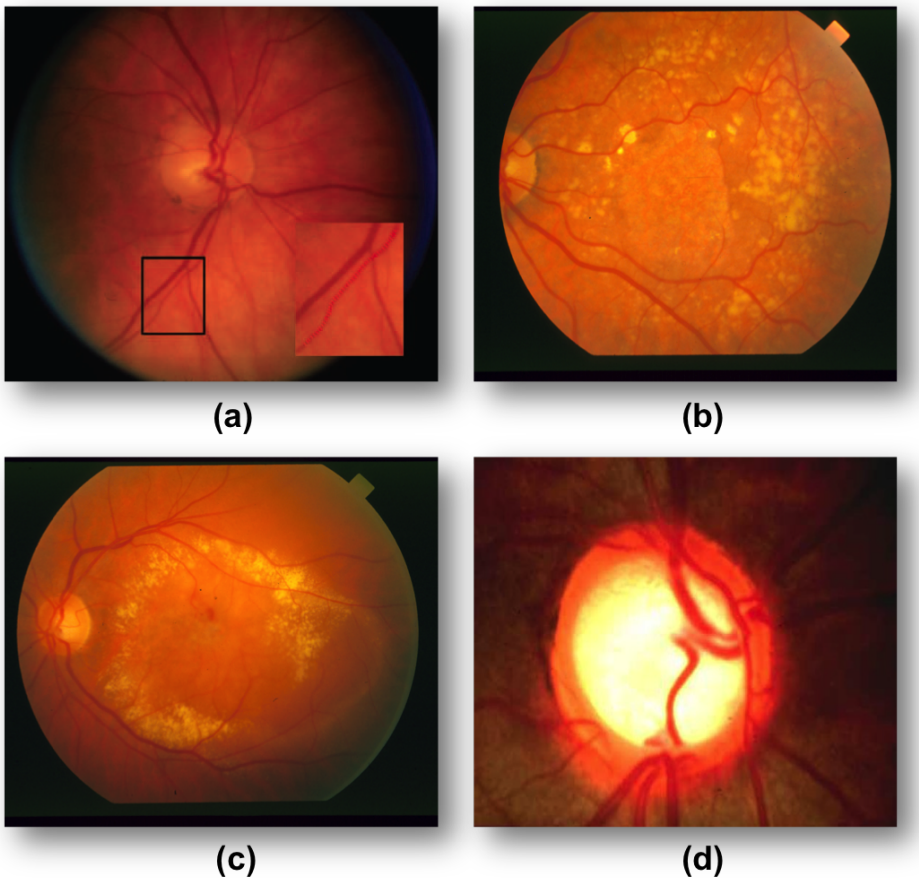

Figure 2.4: Diseases of the retina. **(a)** Fundus photograph of the retina of hypertension patient showing narrow retinal arteriole [LWMW08]. **(b)** Age-macular degeneration fundus retinal photograph with yellow-orange spots. **(c)** Fundus photograph of diabetic retinopathy showing deep yellow hard exudate. **(d)** Fundus photograph of glaucomatous damage showing change in optic nerve head [Ocu14].

Age-Related Macular Degeneration (AMD)

Age-related macular degeneration is considered to be the leading cause of blindness in the developed world. In the US only over 11 million people live with AMD. This number is estimated to 22 million by 2050 [Mac14]. AMD is the cause of vision loss fro 54% of all bling people in America [FOM+04] and the risk of the AMD increases from 2% for adults ages (50-59) to 30% for those over 75 of ages. The cost of this chronic ocular disease is estimated at US343 billion globally and its severity can reduce

the possibility of employment by 61% and salary by over 39% [AGS10]. There are two forms of AMD including the dry AMD and wet AMD (choroidal neovascularisation).

- Dry AMD is the early stage of AMD disorder, about 90% of AMD patients develop a dry AMD. This form of AMD is causes by a build up of waste material under the macular region and thinning of the retina around the macular area, which can led to dangerous form of AMD (late AMD) causing gradual damage of vision acuity [moo14b].

- Wet AMD also known as choroidal neovascularisation (CNV); represents approximately 10% of AMD cases and causing 90% of legal blindness amount AMD patients [Mac14]. This form of AMD is characterised by ingrowth of abnormal blood vessels underneath the retina. These vessels can leak blood and fluid within or below the retina causing severe permanent partial visual loss (central vision) when blood and fluid reach the centre of the macular, as seen in Figure 2.4(b). In most cases of severe wet AMD, the vision loss is not total and the AMD subject can see through the periphery of the retina. The late AMD caused by the thinning of the retina known as geographic atrophy can cause blindness through loss of macular tissue without any bleeding of unhealthy blood vessels [moo14b].

Both forms of AMD can be detected through a dilated eye exam, visual acuity test, fundoscopy and more importantly fundus photography. While the dry AMD can be slowed through some dietary supplements [AGS10], a severe progress of wet AMD can be stopped with intravitreal injections of anti-vascular (anti-VEGF) growth medicine such as ranibizumab [SLF+06], [LMS+12].

Cardiovascular Diseases (CVD)

Cardiovascular diseases are disorders that affected the blood vessels and the heart. These disorders included [WHO14]:

- Cerebrovascular disease. This affects blood vessels that transport blood into the brain.
- Peripheral arterial disease. This abnormality occurs when the blood vessel networks supplying the legs and the arms are dysfunctional.
- Deep vein thrombosis and pulmonary embolism. This occurs when blood clots in the leg vein affecting the lungs and the heart if not treated.
- Rheumatic heart disorder. This is caused by rheumatic fever (from streptococcal bacteria) damaging the heart valves and muscle.
- Congenial heart disease. Occurs when the heart structure are malformed from birth. Strokes and heat attacks are usually severe cardiovascular disorders. These diseases are generally caused by a blockage of blood supply into the brain or heart. This blockage is usually caused by a deposit of fat on the inner walls of the blood vessels that carry blood to the brain or heart.

Cardiovascular diseases are considered to be the leading caused of death globally [A+11]. Approximately 17.3 million people died from cardiovascular diseases in 2008, around 30% of all global deaths [A+11]. Amount these 17.3 million were caused by coronary heart disease and 6.2 million were caused by stroke [MPN+11], this number is estimated to reach 23.3 million by 2030 [A+11], [ML06]. Cardiovascular diseases can be detected in the retina as they change the structures of the retina blood vessel networks,as seen in Figure 2.4. For example, Atherosclerosis and hypertension can affect the ratio between the diameter of the retina arteries and veins (A/V ratio) [AGS10], [WSK+04]. The risk of stroke and myocardial infraction increases when the A/V ratio decreases, caused by the widening of the veins and thinning of the arteries [WSK+04], [HBK+99].

Furthermore, systemic cardiovascular disorders can also cause arterial and venous occlusions leading to bleeding in the retina. Most of the cardiovascular diseases can

be assessed using retinal imaging techniques. Several computer algorithms have been developed to measure the retina vascular calibre [LWMW08]. These tools can also be used to assess retinal vessels structures including vessel angle and tortuosity, the length to diameter ratio of vessel networks, which appear to carry prognostic information about the risk of cardiovascular diseases [LWMW08], [WWH+06], [PAM+06].

2.3 Introduction to Retinal Imaging Tools

The ocular structures allow us to see the retina non-invasively through the pupil. Thus with proper imaging tools, we can perform non-invasive observation and imaging of the retina tissue [AGS10], illustrated in Figure 2.1. Jan Mery a French physician produced the first image of the retina using a cat. This discovery allowed various researches in the retina imaging domain until 1853 when the first human retina image was published by a Dutch ophthalmologist Van Trigt. With the advance of the technology, today modern ophthalmology is equipped with more sophisticated retina imaging tools including fundus photography, optical coherence tomography (OCT) and fluorescein angiography. These techniques are described below.

2.3.1 Fundus Imaging

Fundus imaging is one the most popular imaging tools. It is extensively used for large-scale diagnosis of age-related macular degeneration, glaucoma and diabetic retinopathy [AGS10], [ZZM+02], [SQY+08]. The fundus imaging provides a 2-D representation of the 3-D retina tissues using reflected light onto an image plane.

Different Fundus Imaging Techniques

There are various retinal-imaging techniques. Most popular fundus imaging includes the following techniques [AGS10].

- Fundus photography: To analyse retinal diseases, the image is obtained through

a projection of reflected light from the retina onto a 2-D image plane. With the fundus photography, the intensity of the images are defined by the amount of reflected light from the retina of a specific waveband. This includes red-free photography.

- Colour fundus retinal photography: Unlike a red-free photography the intensities of the colour fundus retinal image are defined by the amount of reflected light of red (R), green (G) and blue (B) waveband.
- The large choroid blood vessels or choroid plexus.
- Stereo fundus photography: In this image, the pixels intensities are defined by the amount of reflected light from separate view angles for depth resolution.
- Hyper-spectral imaging: It is used for retinal diseases examination. With this imaging technique, we can obtain the spectrum for each pixel in the retinal image. It uses multiple wavelengths of light to capture an image of the retina. The pixels intensities of the image are defined by the amount of reflected light of various specific wavelength bands.
- Scanning laser ophthalmoscopy (SLO): This technique is generally used for diagnosis of retinal diseases such glaucoma, age-related degeneration and other retinal pathologies. This imaging method uses confocal laser scanning microscopy with vertical and horizontal scanning mirrors allowing the scanning of any specific area of the retina. The pixels intensities of the image generated by this tool can be presented by the amount of the reflected single wavelength laser light gained in a time period.
- Adaptive optics SLO: The imaging model uses a diode laser to generate light, which is combined into a single mode optical fiber. The pixels intensities values are defined by the amount of optically confined reflected laser light.

- Fluorescein angiography and indocyanine angiography: This imaging tool uses a fluorescent dye and a specific camera to inspect the circulation of the retina. The examination is performed by injecting the sodium fluorescein into the subjects circulation and the image is generated by capturing the emitted fluorescence using blue light [BAS+88]. The intensities of the image are defined by the amount of reflected light from the fluorescein injected into the circulation.

Figure 2.5(a) shows a Topcon TRC-NW8 Non-Mydriatic Retinal Camera. This camera provides clean and more detailed high-resolution colour and monochrome image of the entire retina at true 45% field of view (FOV).

Challenges in Fundus Retinal Imaging

The projection of light through the pupillary plane (pupil, iris) to illuminate the retina has always been the main technical challenge in retinal photography [Gul10], [AGS10]. The structure of the retina makes it dark internally, therefore to capture the image of the retina, internal illumination is required. This process is very complicated to achieve due to the small opening of the iris and the size of the pupil. This makes it difficult to separate the incoming light to illuminate the retina and the reflected light from the retina causing an overlap of the two beams, which diminishes or eliminates image contrast. Path separation mechanisms in the pupillary plane have been used to address this problem, which create a small optical opening (few millimetres) between the two lights. However this imaging architecture is technically challenging, making the retina photography tools expensive and difficult to operate [AGS10].

Although the separation of the two paths (incoming and reflect lights) remains the key problem in retinal imaging, the progress of the technology has made the fundus photography more accessible and less dependent on highly skilled ophthalmic photographers. It has allowed the transition of film based imaging to digital imaging [MS93]. Consequently the communication and the archiving systems have dramatically improved. This has also introduced the electronic health records system in modern oph-

Figure 2.5: Retina imaging tools. **(a)** Topcon TRC-NW8 Non-Mydriatic Retinal Camera can produce high resolution color and monochrome images of the retina and the anterior segment with a 45 degree field of view [Top14]. **(b)** Volk Pictor is a non-mydriatic fundus portable digital imaging device that provides a variety of imaging capabilities including ophthalmic-posterior, ophthalmic-anterior segment, otoscopic and dermatoscopic [Vol14]. **(c)** F-10 confocal digital ophthalmoscope from NIDEK provides high-contrast images of every detail of the retina and choroid [Las14]. **(d)** Heidelberg Spectralis HRA + OCT is a Fourier Domain Optical Coherence Tomography system equipped with ultra-high speed and high resolution OCT retina scanner that can capture the 3-D images of the retina [Hei].

thalmology [CBM+08], [AGS10]. Progress has also been seen in the manufacturing of fundus cameras with the invention of non-mydriatic fundus imaging tools, digital infrared fundus camera and mini-fundus cameras as shown in Figure 2.5(b) allowing

more effective diagnosis of retinal diseases.

2.3.2 Optical Coherence Tomography (OCT) Imaging

Recently with the progress of the technology, the OCT image techniques including Heidelberg Retinal Tomography (HRA+OCT, Heidelberg Engineering, Germany) and the retinal thickness analyser (HRA+OCT, Talia Technology Inc., Tampa, Florida, USA) have become the most powerful imaging tools for diagnosis and management of retinal disorders in modern ophthalmology [JC04]. The OCT can capture a cross-sectional tomographic of the retina as well as the 3-D representation of the retina. This imaging tool has been used in the treatment and management of retinal diseases such glaucoma, choroidal neovascularisation, macular edema, vitreomacular traction and diabetic retinopathy [JC04].

This photography tool was introduced by team of scientists in 1991 [HSL+91], since then the OCT has been used in ophthalmic applications for diagnosis and management of retinal diseases [SIL+93], [Pod14]. The OCT technology combines the tomography and the Michelson interferometry techniques to capture detailed images of the retina structures [HSL+91]. The principle of the OCT is based upon low coherent light interferometry (white light interferometry) with a depth-scanning ability [FMW88] [Rie00] , which can provides images with a resolution of up to 500 micrometres. Since the resolution in depth or axial depends on the optical bandwidth of the near-infrared light instead of the optical aperture, the OCT has becomes the best imaging tool to examine the tissue of the retina, which has a total thickness between 300-500 micrometres micrometres [HSL+91], [AGS10].

To capture a cross-sectional and volume image of the retinal tissues, the low-coherence near-infrared light of the OCT is split into two arms by a beam splitter, which include a sample arm and a reference arm. The sample arm is projected to the retina through the pupillary plane while the reference arm (usually a mirror) is moved back and forth to create a continuous and changing distance with the beam splitter.

The reflected light from the retinal tissue layers and the reference arm are combined to generate an interference pattern. The combination of the two lights occurs only if the distance between the low-coherence near-infrared light source and the retinal tissue layers is equal to the distance between the same light source and the reference mirror [JC04]. The interference pattern is processed into a signal (reflectivity profile) also known as A-scan or axial depth scans, which includes all the information (location of structures and special dimensions) about the retinal tissue layers. A two-dimensional cross sectional image (B-scan) is produced by combining a series of A-scans and a three-dimensional retinal image may be achieved by a series of stacked and connected B-scans. Figure 2.6 shows a schematic representation of a time-domain OCT (TD-OCT) imaging system setup. More information and comprehensive detail about the OCT imaging tools can be found in [JC04].

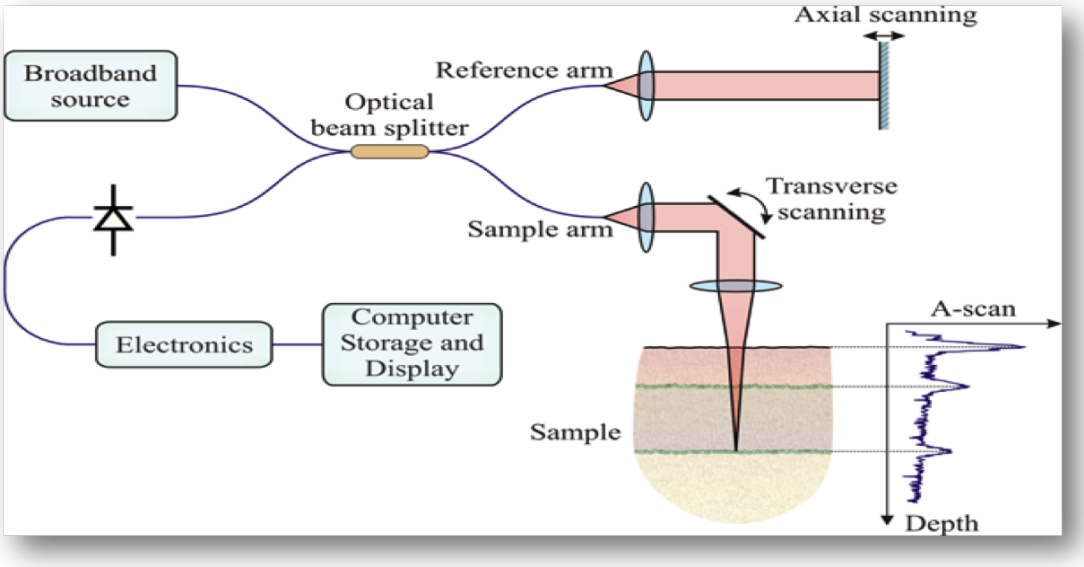

Figure 2.6: A schematic diagram of a time-domain OCT (TD-OCT) imaging system [Sch14].

The OCT image can provide clear distinction between different retinal tissue layers because the intensity of the reflected light is usually different for each retinal tissue

layer. The OCT images are available on grayscale (highly reflected light-beam from the tissues appears brighter than less highly reflected light-beam) and colour where different colours represent different degree of reflectivity [JC04]. In most of the current commercially available OCT imaging tools, highly reflective tissues are represented in bright colours, usually red and white. Those with low reflectivity are shown with dark colours such as black and blue, while those with intermediary reflectivity are represented in green [JC04]. The resolution of the OCT images depends on the axial plane (z axis) and the transverse plane (x-y axis). The axial plane affects the OCT image resolution when a short wavelength (cannot reach thick tissues) is used to capture retinal tissues that contain a high level of water such as vitreous and cornea. Axial resolution can be improved partially using adequately long wavelength light, allowing better penetration of light into the retinal tissue layers. In addition to the wavelength, axial resolution can also be enhanced by a light-beam with a broader spectral bandwidth capable of producing a short coherence incident light-beam [HSL+91]. Most of the current OCT scanners use a low coherence super-luminescent light-beam diode source with 820nm.

The transverse plane (x-y axis) resolution usually depends on the number of scans on the x-axis rather than on wavelength. Current commercially available OCT imaging tools use sophisticated scanning mode capable of producing 512 separate scan points in the x-axis compared to 100 scan points of early OCT scanners. The use of better light detectors and high speed scanning capability have significantly improved the transverse resolution.

Commercially available OCT scanners include the time-domain OCT (TD-OCT) and the Fourier or spectral domain (SD-OCT). Stratus OCT (Carl Zeiss Meditec Inc., Dublin, CA, USA) is one the most popular TD-OCT scanners for retinal imaging in clinical applications. This imaging tool has an axial resolution $\leq 10\mu m$ and a lateral resolution of $20\mu m$ and can acquire 400 A-scans per second, which are joined to form a two-dimensional cross sectional image (B-scan). These A-scan are captured at different depths using a mobile reference arm. This mobile reference arm tends to reduce the

speed of the imaging; consequently the number of A-scans is reduced to prevent error in retinal tissue mapping when the patient blinked during the imaging process. Due to its low speed in image acquisition, TD-OCT can only provided the retinal nerve fibre layer thickness (RNFLT) measurements in a line scan and it cannot generate a 3-D RNFL structures [SHA+95], [HSL+91].

To address these limitations, the Fourier or spectral domain SD-OCT [WLK+02], [And] was developed with faster scan capability that provides the most comprehensive structure of the retina. With these new capabilities, the OCT scanner possesses a powerful tool that allows a 3-D image of the retina to be formed in routine clinical scans. Unlike the TD-OCT scanner, the SD-OCT uses a stationary reference mirror arm and a high-speed camera spectrometer to record interference signal of the reflected scattered light-beam from all the tissue points simultaneously. The special information of the image is generated by the Fourier transformation (FT) of the interference signal and with no mobile reference and high signal processing power, the scan speed of the SD-OCT scanner is approximately 50-100 times faster than a typical TD-OCT [And]. The current generation of SD-OCT scanners can capture $100,000$ A-scans per second with an axial resolution of $3-5\mu m$ and this number can be increased to $250,000$ A-scans per second with axial resolution of $5-10\mu m$ [And]. A high-resolution SD-OCT Spectralis HRA+OCT (Heidelberg Engineering, Germany) is widely used SD-OCT scanner. It combines the Spectralis HRA and Spectralis OCT, capable of producing retinal scans with fluorescence, angiography and OCT. Figure 2.5(d) shows an image of SD-OCT Spectralis HRA+OCT. The high-resolution SD-OCT Spectralis has $7\mu m$ depth resolution with a $14\mu m$ lateral resolution, it captures around 40000 A-scans per second and 50 B-scans per second.

Both SD-OCT Spectralis and Stratus OCT can provide single, circle and star scans as shown in Figure 2.7(a-c). The single and star scans are often used to analyze retinal disorders affecting the macular region such as age-related macular degeneration, macular hole and retinal detachment. The circular scan is use to assess and manage

glaucoma by analysing the retinal nerve fibre layer thickness. The RTVue 100 scanner (Optovue, Fremont, CA, USA) and Spectralis HRA+OCT (Heidelberg Engineering, Germany) can provide a 3-D volume of the retinal image with 513 by 101 A-scans around the macular or the optic nerve head (ONH). Figure 2.7(d) shows the 3-D volume scan of the retina around the macular acquired by the Spectralis HRA+OCT (Heidelberg Engineering, Germany).

While both the fundus and OCT scanners provide objective information for the diagnosis of retinal diseases, the interpretation of those images remains subjective especially when manual planimetry (evaluating images by hand) is used to assess the images. Reports of several studies [VSS92], [MZB+05], [Lic76], [JC04] have shown great variation in retinal image evaluation among experts in retinal disorders. Therefore reliable automated or semi-automated methods for quantitative assessment of retinal images are attractive in computer-aided diagnosis.

In the next chapters, a review will outline automated methods for retinal diseases analysis including retinal blood networks segmentation, optic nerve head detection and retinal nerve fibre thickness assessment using fundus and OCT images. These methods could allow ophthalmologist or retinal diseases experts to perform mass population vision examinations for early detection and management of retinal disorders. This could also prevent and reduce the number of vision disorders and many microvascular diseases as well as reducing the cost of eye screening around the world.

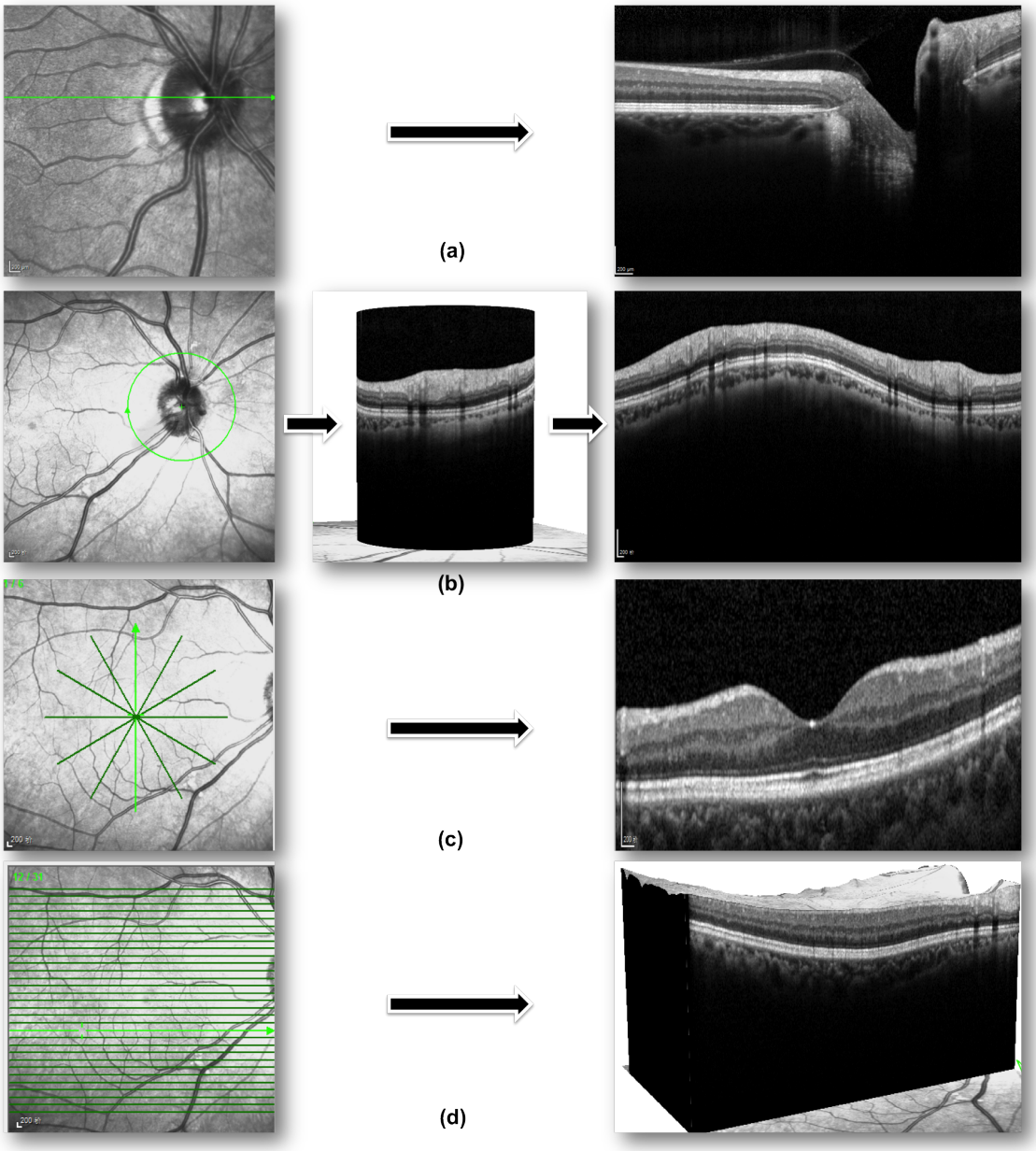

Figure 2.7: Different types of retina scanning indicated by the green arrows on the retina. **(a)** Single scan. **(b)** Circle scan. **(c)** Star scan. **(d)** 3-D scan.

Part II

Contributions

Chapter 3

Retinal blood vessels extraction using Mixture of Gaussians

This chapter contains our first contribution.

3.1 Introduction

The segmentation of the blood vessel network in the retina allows ophthalmologist and eye care specialists to perform large population vision screening exams for early detection of retinal diseases and treatment evaluation. This non-intrusive diagnosis in modern ophthalmology could prevent and reduce blindness and many cardiovascular diseases around the world. An accurate segmentation of retinal blood vessel (vessel diameter, colour and tortuosity) plays an important role in detecting and treating symptoms of both the retinal abnormalities and diseases that affect the blood circulation and the brain such as haemorrhages, vein occlusion, neo-vascularisation. However, the presence of pathologies such as haemorrhage, lesions and swelling in diseased retinas as shown in Figure 3.1(c-d) causes errors in the segmentations. In addition to the pathologies, the intensity inhomogeneity and the poor contrast of the blood vessels in the retinal photographs cause a significant degradation to the performance of

automated blood vessel segmentation techniques. The intensity inhomogeneity of the fundus retinal image is generally attributed to the acquisition of the image under different conditions of illumination as illustrated in Figure 3.1(a). Therefore, a reliable and robust automated method for retinal blood vessel is attractive in computer aided-diagnosis.

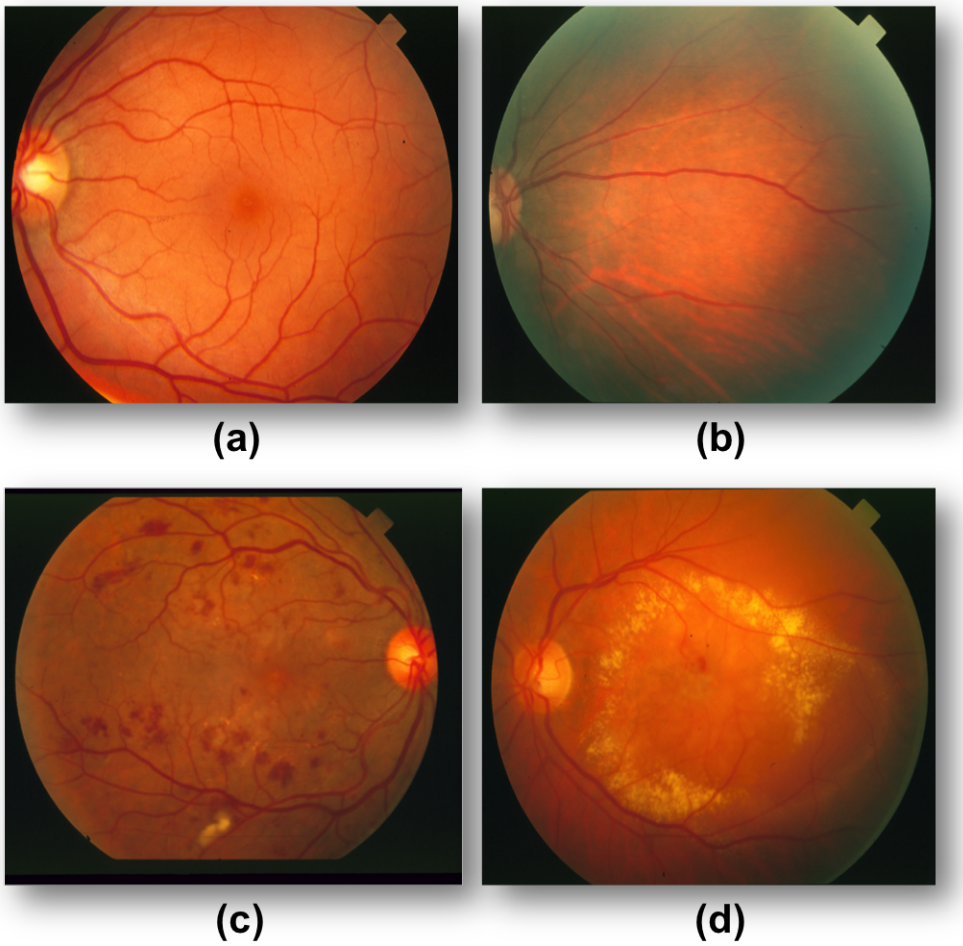

Figure 3.1: Example of fundus retinal photographs. **(a)** Healthy retinal image with well defined blood vessels. **(b)** Retinal image with intensity inhomogeneity. **(c) - (d)** Images of retinas containing lesions.

3.2 Previous Works

The retinal blood vessel segmentation is one of the most challenging problems in retinal image analysis. The morphology of the retinal blood vessel is an important structural indicator for assessing the presence and severity of retinal diseases such as diabetic retinopathy, hypertension, haemorrhages, vein occlusion and neo-vascularisation. Furthermore, the relative diameters of arteries and veins are a very important indicator of the risk of systemic diseases such as stroke [AGS10]. Thus an accurate segmentation of the retinal blood vessels has become more important in modern Ophthalmology. Several automated and semi-automated techniques have been deployed to segment the blood vessels in the fundus retinal images. The segmentation of the retinal blood vessels can be divided into two different approaches: the pixel processing based methods and tracking based methods [FCS+03].

3.2.1 The Pixel Processing Based Approach

The pixel processing based approach uses a two-pass operation to perform the extraction of the vessel trees from fundus retinal images. The first step of the algorithm consists of enhancing the appearance of the blood vessel using image processing techniques including morphological techniques and adaptive filtering. The second step of the operation is to find the blood vessel structures using thinning or branch point operations. This operation locates and classifies each pixel in the retinal image as a vessel pixel or background pixel.

The pixel processing based approach analyses every pixel in the image and classifies them by applying multiple operations on each pixel. Some pixel processing techniques use neutral networks and frequency analysis to define each pixel in the image as a vessel pixel or a background pixel. Typical pixel processing based approaches are published in the following:

Hoover et al. [HKG02] proposed a new framework to extract blood vessel from

fundus retinal images. The proposed method included two steps: the first step consists of using a set of twelve directional kernels to enhance the appearance of the blood vessels. And the second step applied the threshold-probing operation to classify each pixel in the enhanced image as vessel pixel or a background pixel. The technique was evaluated using the STARE dataset, which was collected by Hoover and his team. The STARE dataset is publicly available for research and it includes experts hand labelling of the blood vessels for evaluation of the segmentation results. The dataset is also used in this work to evaluate the blood vessels segmentation results of our methods.

Mendoca et al. [MC06b] presented a novel automated segmentation of the retinal blood vessels by combining the detection of centrelines and morphological reconstruction. The first operation in this segmentation technique is the extraction of vessel centrelines, which are then used to guide the second operation of the segmentation (vessel filling). A combination of four directional differential operators and vessel-derived features are used to classify vessel centreline pixels. Finally the vessel is extracted using an iterative region growing method.

Staal et al. [SAN+04a] proposed a supervised retinal blood vessel segmentation in two dimensional colour retinal images. The method uses images primitives, which are formed from image ridges. The images ridges are first grouped into sets that approximate straight-line elements. The first step of the algorithm is the selection of features that are classified by finding the probability of a line element belonging to a vessel. The line elements are used to partition an image into patches by grouping pixels to the closest line element. Feature vectors are then computed for every pixel, which uses properties of the patches and the line elements. The classification of the feature vectors is performed using a kappa NN-classifier and sequential forward feature selection.

Soares et al. [SLC+06a] proposed an automated segmentation of the retina vessel trees using a supervised approach. The algorithm used a feature vectors consisting of the pixel's intensity and two-dimensional Gabor wavelet transform responses taken at

multiple scales. The Gabor wavelet transform is used to enhance the appearance of the vessels in the image. After feature vector selection based on the pixel's intensity, the segmentation is obtained by classifying each image pixel as vessel or non-vessel. This operation is performed using a Bayesian classifier with class-conditional probability density functions defined as Gaussian mixtures. The probability distributions used by the algorithm are derived based on a training set of experts hand labelled pixels.

Chaudhuri et al. [CCK+89b] presented a method for detecting the retinal blood vessels in the fundus retinal images. This technique is one of the first automated methods for the segmentation of the retina vascular trees. The algorithm performs the detection of the vessels pixels using an operator for feature extraction generally based on both the optical and the special proprieties of the blood vessels. To produce an accurate segmentation result, the algorithm uses a Gaussian shaped curve to approximate the grey-level profile of the cross section of a blood vessel. The piecewise linear segment of the blood vessel in the retinal image is detected with the application of a matched filter. For these operations, 12 different kernels were used to search for vessel segments through all the possible directions of blood vessels.

Zana et al. [ZK01] proposed an automated segmentation of the retinal blood vessels based on mathematical morphology and curvature evaluation for the detection of vessel-like patterns. In this algorithm, a blood vessel is defined as bright pattern, which is piece-wise connected, and locally linear. A mathematical morphology is used to enhance the vessels and reduce the noise in the image. This operation is followed by the separation of vessels from analogous background patterns using a cross-curvature evaluation.

3.2.2 The Vessel Tracking Based Approach

The second approach to vessel segmentation is referred to as vessel tracking, vectorial tracking or tracing [FCS+03]. In contrast to the pixel processing based approach, the tracking method detects first initial vessel seed points, and then track the rest of the

vessel pixels across the image by measuring the continuity proprieties of the blood vessels. Unlike the pixel processing based approach, this approach is used as a single pass operation, where both the detection of the vessel structures and the recognition of the structures are generally performed simultaneously .

The tracking based approach included semi-automated tracing and automated tracing. In the semi-automated tracing methods, the user manually selects the initial vessel seed points. These methods are usually used in quantitative coronary angiography analysis and they generally provide accurate segmentation of the vessels. In fully automated tracing, the algorithms automatically select the initial vessel points and most methods use Gaussian functions to characterise a vessel profile model, which locates a vessel point for the vessel tracing. They are computationally efficient and more suitable for retinal image processing. Some examples of the tracking based approaches for blood vessel segmentation are listed below:

Maritiner-perez et al. [MPHT+07a] proposed a segmentation method of blood vessels from red-free and fluorescein retinal images. This method is based on multi-scale feature extraction, which uses the first and second spatial derivatives of the image intensity that provides information about vessel topology. A multiple pass region growing procedure is applied to segment the vessels using both vessel feature information and spatial information. The multiple pass regions growing operation is performed using the local maxima over scales of the magnitude of the gradient and the maximum principal curvature of the Hessian tensor. The use of multiple pass regions growing allows this approach to segment blood vessels of different widths, lengths and orientations.

Xu et al. [XL10] proposed a method to segment retinal blood vessels to overcome the variations in contrast of large and thin vessels. The first step the algorithm is the segmentation of the blood vessels using adaptive local thresholding. The large connected components in the binary image are selected as large vessels. The pixels of the remaining components in the binary image including thin vessels are classified as vessel pixels and background pixels using Support Vector Machine (SVM). The

tracking growth algorithm performs the detection of the thin vessel segments to produce a complete blood vessels network.

Zhou et al [ZRSC94] presented the detection and quantification of retinopathy using digital angiograms. The algorithm used in the segmentation combined a matched filter and an adaptive densitometric vessel tracking operation. A matched filter with a prior knowledge of retinal vessel properties is applied to automatically define the boundaries of the blood vessels. The midline of the vessel is then tracked using an adaptive densitometric tracking operation based on local neighbourhood information. This tracking technique is designed in such way that it achieves high computational performance in regions where the vessel is relatively straight.

Poletti et al [PR14] proposed a fully automated method for the extraction of retinal blood vessels using graph search retinal vessel tracking. The first step in this segmentation method is the correction of the luminosity and contrast in the retinal images. A seed point is defined to identify a set of points as the starting nodes for a simultaneous searches operation. This operation is performed by means of search trees, where each search is rooted at a seed point. During the search operation, when two trees meet, the shortest path that connected them is recorded and set as a new starting point for a new search. The segmentation is completed by a final step connecting vessel segments. After the identifications of the vessel axes, the vessel diameter is extracted.

Chutatape et al [CZK98] presented an algorithm for retinal blood vessel detection and tracking using matched Gaussian and Kalman filters. The segmentation algorithm included scanning and tracking. A second order derivative Gaussian matched filter is applied on the retinal image to identify both the centre point and width of a vessel in its cross sectional profile. The next possible location of the blood vessel segment is estimated using an extended Kalman filter. A simple branching algorithm is applied during the tracking to identify the branching in the vessel trees. A combination of scanning and tracking algorithms work reasonably well in the detection of the blood vessels as more complete vessel networks were detected by this technique.

Grisan et al [GPG+04], proposed an automated extraction of the vascular tree in the retinal image, based on a sparse tracking method. The algorithm starts by pre-processing pixels in the image to identify a set of seeds to be used as the stating point of the tracking operation. The tracking operation is performed by moving along the vessel to analyse and subsequently create a vessel cross sections using a means of a fuzzy c-means classifier. This process defines the vessel centre and direction of the vessel. A greedy algorithm connects the vessel segments found in the tracking operation.

Both pixel processing and tracking approaches have their own advantages and limitations over one another. The pixel processing approaches can be categorised into unsupervised and supervised methods. They provide a complete extraction of the vascular structures in the retinal image since they search all the possible vessel pixels across the whole image. In the literature, the evaluation of retinal vessel segmentation based on the accuracy and sensitivity has proved that pixel processing supervised methods generally outperforms other methods [NSvG+04]. However the supervised methods need a set of manually labelled retinal vessel images as a training dataset to achieve a higher segmentation results. Unsupervised methods of the pixel processing generally produce very good segmentation results but the presence of noise and lesions in some retinal images causes a significant degradation in their performance as the enhancement operation may pick up some noise and lesions as vessel pixels. This could lead to false vessel detection in the recognition operation. This problem is also shared by some supervised methods. Furthermore, the pixel processing approaches are computationally expensive and require special hardware to be suitable for large image dataset.

On the other hand, the tracking approaches are computationally efficient and much faster than the pixels processing methods because they perform the vessel segmentation using only the pixels in the neighbourhood of the vessels structure and avoid the processing of every pixel in the image. Nevertheless, these methods lack in extracting a complete vascular network in the case where there are discontinuities in the vessel

branches. Additionally, the semi-automated tracking segmentation methods need a manual input, which requires more time.

In this work we provide an automated pixel processing based blood vessel segmentation method, that include Probabilistic Modelling algorithms. The proposed method uses the bias correction, adaptive histogram equalisation (AHE) and distance transform in pre-processing operations to enhance the appearance of the blood vessel networks. This method could be used as tools for automated eye screening, image registration and treatment evaluation for retinal diseases.

3.3 Methods

In this section, we discuss automated segmentation of retinal blood vessel in the fundus retinal image using Mixture of Gaussians algorithm. We use the Mixture of Gaussians algorithm because it is one of the most powerful methods, which allows to find maximum likelihood solutions for models with latent variables [DLR77]. The method uses the bias correction operation [TAC+10a] as pre-processing operations to remove all the fundus imaging artefacts including noises and intensity inhomogeneity. It also removes from the image some affects of pathologies such as lesions and swelling. An AHE and distance transform are applied for further blood vessels enhancements in the images. This second pre-processing step allows the segmentation of narrow blood vessels. Figure 3.2 shows an overview diagram of the proposed segmentation method.

3.3.1 Bias Correction

One of the major issues associated with fundus retinal images is the intensity inhomogeneity across the images, which causes a significant degradation to the performance of automated blood vessels segmentation techniques. The intensity inhomogeneity of the fundus retinal image is generally attributed to the acquisition of the image under different conditions of illumination. In order to overcome such a problem, we use the

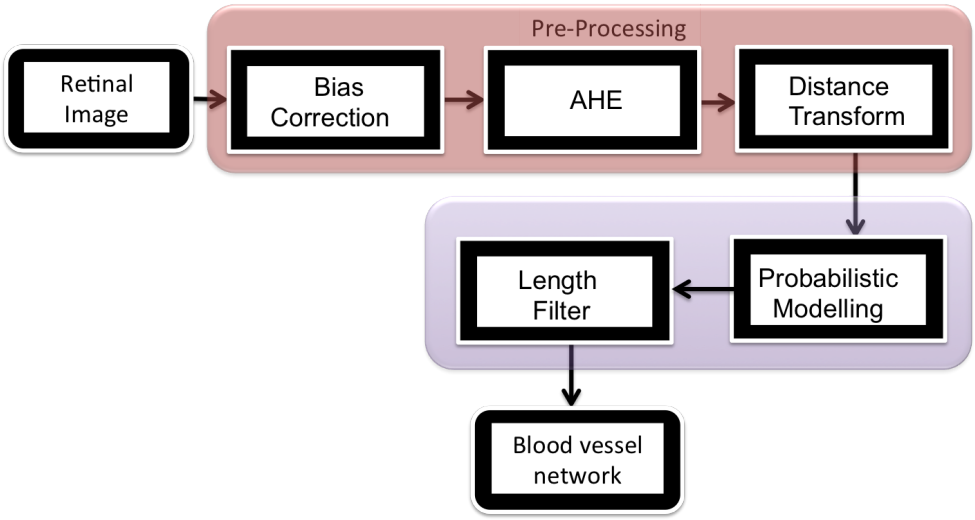

Figure 3.2: Algorithm of the Mixture of Gaussians.

N4 algorithm of bias correction presented in [TAC+10a] which is a modified version of the original bias correction proposed N3 algorithm [SZE98] that includes a modified iterative update within a multi-resolution framework. If we consider a noise free retinal fundus image $v(x)$, defined as

$$\hat{v}\left(x\right) = \hat{v}'\left(x\right) + \hat{f}\left(x\right) \tag{3.1}$$

where $v'\left(x\right)$ is the uncorrupted image, $f\left(x\right)$ is the bias field and $\hat{v}\left(x\right) = \log v\left(x\right)$, $\hat{v}'\left(x\right) = \log v'\left(x\right)$ and $\hat{f}\left(x\right) = \log f\left(x\right)$. The following iteration solution derived in [SZE98] is used to define the uncorrupted image at the n^{th} iteration as

$$\hat{v}'\left(x\right) = \hat{v}\left(x\right) - \hat{f}\left(x\right)$$

$$\hat{f}\left(x\right)_r^n = S^*\{\hat{v}'\left(x\right)^{n-1} - E[\hat{v}'\left(x\right) \mid \hat{v}'\left(x\right)^{n-1}]\} \tag{3.2}$$

$$\hat{v}'\left(x\right)^n = \hat{v}\left(x\right) - S^*\{\hat{v}\left(x\right) - E[\hat{v}'\left(x\right) \mid \hat{v}'\left(x\right)^{n-1}]\} \tag{3.3}$$

where $\hat{f}(x)_r^n$ is the estimated residual bias field at the n^{th} iteration and $E[\hat{v}'(x) \mid \hat{v}'(x)^{n-1}]$ is the expected value of the true image given the current estimate of the corrected image and it is defined in [SZE98]. $S^*\{.\}$ is referred as the B-spline approximator or the smoothing operator.

The iterative solution used to perform the bias correction is given in (3.3), where $\hat{v}(x) = \hat{v}'(x)^0$ and the initial bias field estimate $\hat{f}(x)_e^0$ is equal to zero. The first iteration yields

$$\hat{v}'(x)^1 = \hat{v}(x) - \underbrace{S^*\{\hat{v}(x) - E[\hat{v}'(x) \mid \hat{v}(x)]\}}_{\hat{f}(x)_r^1}$$

$$\hat{v}'(x)^2 = \hat{v}'(x)^1 - \underbrace{S^*\{\hat{v}'(x)^1 - E[\hat{v}'(x) \mid \hat{v}'(x)^1]\}}_{\hat{f}(x)_r^2}$$

$$\hat{v}'(x)^3 = \hat{v}'(x)^2 - \underbrace{S^*\{\hat{v}'(x)^2 - E[\hat{v}'(x) \mid \hat{v}'(x)^2]\}}_{\hat{f}(x)_r^3}$$

$$\vdots$$

$$\hat{v}'(x)^n = \hat{v}'(x)^{n-1} - \underbrace{S^*\{\hat{v}'(x)^{n-1} - E[\hat{z}(x) \mid \hat{v}'(x)^{n-1}]\}}_{\hat{f}(x)_r^n} \tag{3.4}$$

For the second iteration, the iteration scheme uses the corrected log $\hat{v}'(x)^1$ to re-estimate the expected value of the true image $E[\hat{v}'(x) \mid \hat{v}'(x)^1]$, and the bias field estimate $\hat{f}(x)_r^n$ is calculated by inspecting (3.4). The iteration solution is designed to converge such that the value of $\hat{f}(x)_r^n \to 0$. Using (3.4) the total bias field estimate is obtained as

$$\hat{v}'(x)^1 = \hat{v}(x) - \hat{f}(x)_r^1$$

$$\hat{v}'(x)^2 = \underbrace{(\hat{v}(x) - \hat{f}(x)_r^1)}_{\hat{v}'(x)^1} - \hat{f}(x)_r^2$$

$$\hat{v}'(x)^3 = \underbrace{((\hat{v}(x) - \hat{f}(x)_r^1) - \hat{f}(x)_r^2)}_{\hat{v}'(x)^2} - \hat{f}(x)_r^3$$

$$\vdots$$

$$\hat{v}'(x)^n = \hat{v}(x) - \sum_{i=1}^{n} \hat{f}(x)_r^i \tag{3.5}$$

Thus, the total bias field estimate at the n^{th} iteration is derived as

$$\hat{f}(x)_e^n = \sum_{i=1}^{n} \hat{f}(x)_r^i \tag{3.6}$$

Figure 3.3 presents sample results of the bias corrected images from both data sets STARE and DRIVE.

3.3.2 Adaptive histogram equalisation and distance transform

We apply an adaptive histogram equalisation [SGLK12] to the bias corrected image to enhance the contrast between vessel pixels and the background images. The histogram equalisation is performed using the following equation:

$$X(_{enhance}) = \sum_{q' \in R(q)} \Big(\frac{1}{h^2} \underbrace{S\big(X_{q'} - X_q\big)}_{\mathrm{S}\ (\mathrm{d})}\Big)^r \lambda \tag{3.7}$$

where

$$S(d) = \begin{cases} 1 \ if \ d \ > \ 0 \\ 0 \ if \ d \ < \ 0 \end{cases}$$

The notation q represents the pixels in the image and q' is the neighbourhood

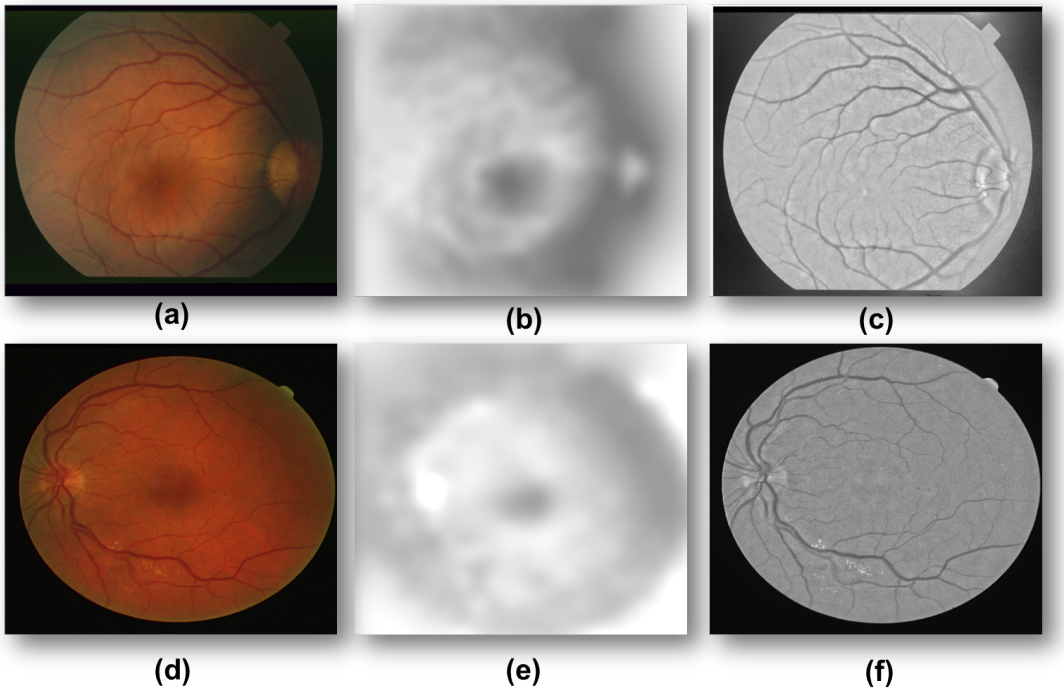

Figure 3.3: Example of Bias correction results. **(a)** STARE image. **(b)** STARE bias field. **(c)** STARE bias corrected image. **(d)** DRIVE image. **(e)** bias field. **(f) DRIVE bias corrected image.**

pixels of q, defined by a square window of width h. The value of r indicates the level of contrast between the vessels and the background, by increasing the value of r, the contrast between vessel pixels and the background increases. λ is the maximum pixel value of the input image ($\lambda = 255$) and R_q is a set of the neighborhood pixels.

Figure 3.4 shows the output images of the adaptive histogram equalisation with different values of r and h.

To reduce the noise in the adaptive histogram equalisation image, a binary morphological open process is used to prune the image by eliminating all the non-vessels pixels. This process is performed by elimination all the pixels in the misclassified pixels during the AHE operation. These pixels are discarded by setting a simple, pre-defined set of pixels number. Any connected pixels less than this number is discarded as noises in the image. The pruned image is used to create a distance map image using a distance

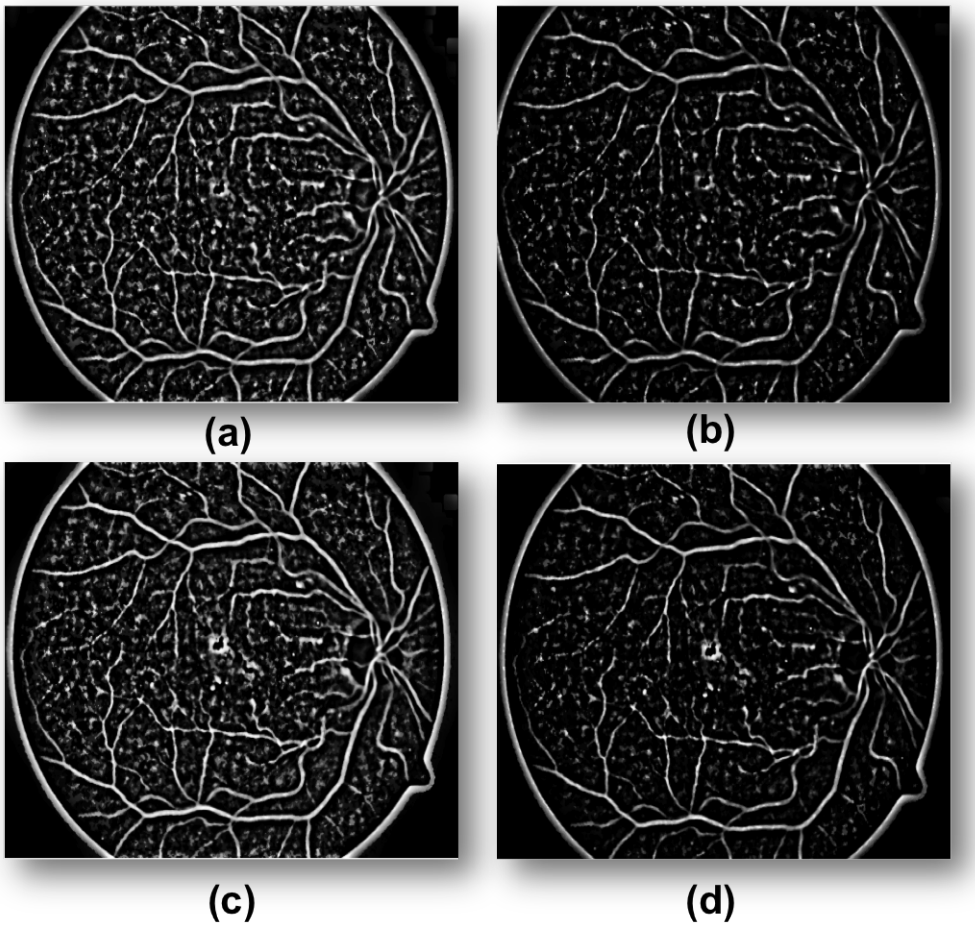

Figure 3.4: Adaptive histogram equalisation results. **(a)** $r = 3$, $h = 45$. **(b)** $r = 6$, 45. **(c)** $r = 3$, $h = 81$. **(d)** $r = 6$, $h = 81$.

transform model. The distance transform gives a measure of the separation of pixels in the image by calculating the distance between each pixel that is set to 0 and the nearest nonzero pixel for the pruned binary images. This operation provides a distance map image as seen in Figure 3.5 (d). Finally, a Mixture of Gaussians model is applied to the distance map image to extract the vessel tree. Figure 3.5 shows different fundus retinal image datasets with their corresponding distance map images.

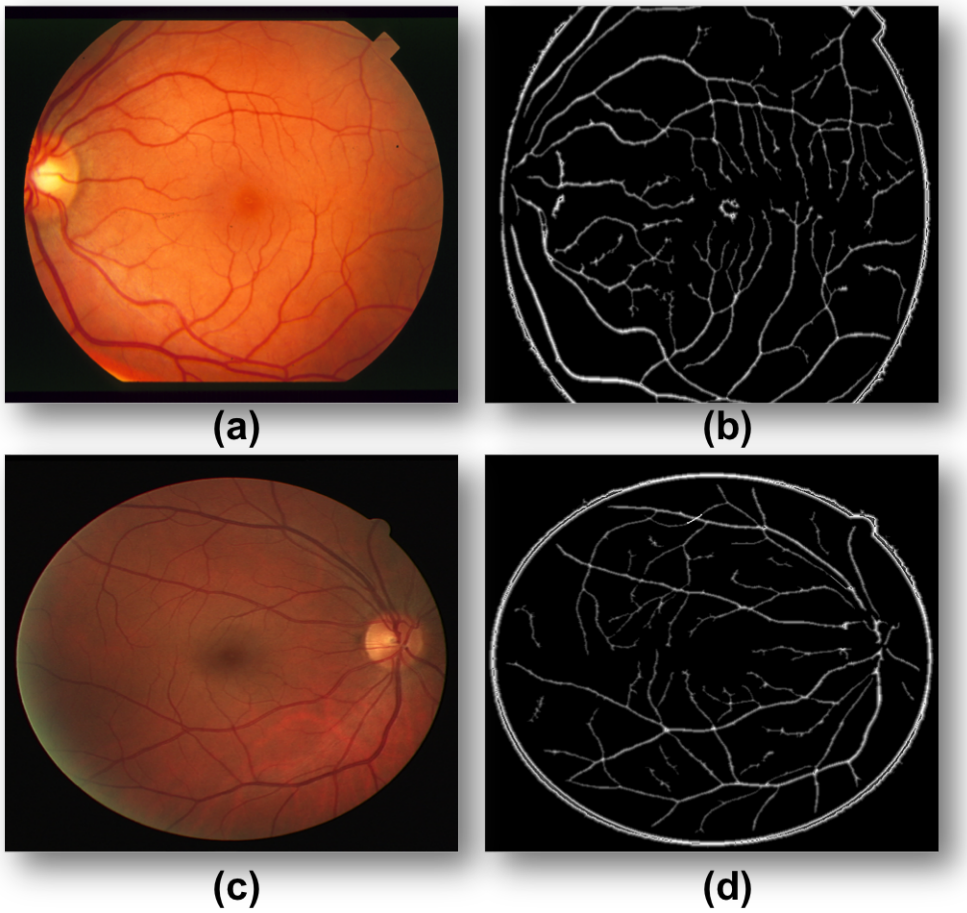

Figure 3.5: **(a)** STARE image. **(b)** STARE distance map. **(c)** DRIVE image. **(d)** DRIVE distance map.

3.3.3 Segmentation Algorithms

The extraction of the blood vessels is modelled with probabilistic unobserved variable model. An unobserved variable is introduced to model the process that determines the component from which the pixels observation originates. We introduce a binary vector $U_k = \{(U_{k0}, U_{k1})\}_{k=1}^{K}$ having a $1-of-K$ representation in which only one of the two elements in U_k can be equal to 1 and the other is equal to 0. $U_{k1} = 1$ if the i^{th} pixels in the retinal image $(X_i)_i^M$ (where M is the number of pixels) can be accurately assigned to K clusters as vessel's pixel otherwise $U_{k0} = 1$. A marginal distribution or a prior probability over U_k is defined such that $P(U_k = 1) = \pi_k$ where $k = 1, \ldots K$ thus:

$$P\left(U_k\right) = \prod_{k=1}^{K} (\pi_k)^{U_k} \tag{3.8}$$

where the probability values $\{\pi_k\}$ must satisfy $0 \leq \pi_k \leq 1$ and $\sum_{k=1}^{K} \pi_k = 1$. The aim in this process is to estimate the unknown parameters representing the mixing value between the Gaussians and the mean (μ_k) and covariance (Σ_k) of each component $\theta_k = (\mu_k, \Sigma_k)$. Thus, the conditional distribution or posterior probability of X_i given a particular value for U_k is defined as a mixture of two Gaussian distributions.

$$P\left(X_i \mid U_k = 1, \theta_k\right) = \mathcal{N}\left(X_i \mid \mu_k, \Sigma_k\right)$$

$$P\left(X_i \mid U_k = 1, \theta_k\right) = \prod_{k=1}^{K} \mathcal{N}\left(X_i \mid \mu_k, \Sigma_k\right)^{U_k} \tag{3.9}$$

The joint probability is derived as the product of equations (3.8) and (3.9) to give

$$P\left(X_i, U_k \mid \theta_k\right) = \prod_{k=1}^{K} \left(\pi_k \mathcal{N}\left(X_i \mid \mu_k, \Sigma_k\right)\right)^{U_k} \tag{3.10}$$

where the joint probability $P\left(X_i, U_k \mid \theta_k\right)$ defines a Gaussian mixture, and this model structure has been used in many problems of classification such as [QL05]. Assuming that $\{X_i\}_i^M$ are independent and identically distributed and $\{U_k\}_k^K$ is an unobserved variable, the likelihood is derived by marginalising $P\left(X_i, U_k \mid \theta_k\right)$ over the unobserved variable. In other words, the marginalised distribution of $\{X_i\}_i^M$ is derived by adding the joint distribution over all possible states of $\{U_k\}_k^K$. Our aim is to maximise the likelihood function that is given by

$$P\left(X\right) = \sum_{U_k} P\left(X_i, U_k \mid \theta_k\right) = \sum_{U_k} \prod_{k=1}^{K} \left(\pi_k \mathcal{N}\left(X_i \mid \mu_k, \Sigma_k\right)\right)^{U_k} \tag{3.11}$$

where $P\left(X\right)$ is also a Gaussian mixture as the joint probability $P\left(X_i, U_k \mid \theta_k\right)$. As in vector U_k only one element can be equal to 1, the multiplication and summation

over k in equation (3.11) can be the exhaustive summation of all possible values of $(\pi_k \mathcal{N}(X_i \mid \mu_k, \Sigma_k))$ over k. Thus

$$P(X) = \sum_{k=1}^{K} (\pi_k \mathcal{N}(X_i \mid \mu_k, \Sigma_k)) \tag{3.12}$$

Expectation maximisation

To calculate the maximum likelihood estimate of the equation (3.11), we use the expectation maximisation (EM) algorithm as it is the most powerful method for finding maximum likelihood solutions for models with latent variables [DLR77]. The EM performs the segmentation by classifying vessel's pixels in one class (foreground) and non-vessel's pixels in the other (background). The EM output is obtained by iteratively performing two steps: the expectation E- step computes the expected value of the likelihood function (pixel class membership function) with respect to the unobserved variables, under the parameters of a Gaussian Mixture Model and the maximisation M-step, maximises the likelihood function defined in the E-step until convergence [Bis07].

In the E-step, the posterior probability $P = (U_k \mid X_i, \theta_k)$ of the unobserved variable U_k is derived using Bayes theorem as:

$$P(U_k \mid X_i, \theta_k) = \frac{P(X_i, U_k \mid \theta_k)}{P(X_i)}$$

$$\Gamma(U_k) = P(U_k \mid X_i, \theta_k) = \frac{\prod_{k=1}^{K} (\pi_k \mathcal{N}(X_i \mid \mu_k, \Sigma_k))^{U_k}}{\sum_{j=1}^{K} (\pi_j \mathcal{N}(X_i \mid \mu_j, \Sigma_j))} \tag{3.13}$$

Therefore the expectation of the unobserved variable U_k is derived with respect to the distribution of the posterior probability or the responsibility $\Gamma(U_k)$ that component k takes for assigning the pixel X_i in the E-step. Then followed by the M-step, which calculates parameters maximising the expected log likelihood computed in the E-step. Suppose that the number of pixels in a retinal image is represented by a data set $\{x_i, \ldots x_M\}$ and we aim to model this set using a mixture of Gaussians. A $M \times D$

matrix X is used to represent the pixel data set in which the i^{th} row is defined by x_i^N. The corresponding latent variables is represented by a matrix Z of size $M \times K$ in which the i^{th} row is defined by u_i^N. Assuming that the pixel data points are drawn independently from the Gaussian distribution, we can define the log of the likelihood function using equation (3.12)

$$\ln\{P\left(X \mid \theta\right)\} = \sum_{i}^{M} \ln \left\{ \sum_{k=1}^{K} \left(\pi_k \mathcal{N}\left(x_i \mid \mu_k, \Sigma_k\right)\right) \right\} \tag{3.14}$$

The derivative of $\ln\{P\left(X \mid \theta\right)\}$ with respect to the means μ_k of the Gaussian components is set to 0 to give.

$$-\sum_{i=1}^{M} \frac{\left(\pi_k \mathcal{N}\left(x_i \mid \mu_k, \Sigma_k\right)\right)}{\sum_{j=1}^{K}\left(\pi_j \mathcal{N}\left(x_i \mid \mu_j, \Sigma_j\right)\right)} \left(\Sigma_k \left(x_i - \mu_k\right)\right) = 0$$

$$-\sum_{i=1}^{M} \Gamma\left(u_{ik}\right) \left(\Sigma_k \left(x_i - \mu_k\right)\right) = 0 \tag{3.15}$$

By multiplying (5.7) by $\left(\Sigma_k^{-1}\right)$, we define the means as

$$\mu_k = \frac{1}{\eta_k} \left\{ \sum_{i=1}^{M} \Gamma\left(u_{ik}\right) x_i \right\} \tag{3.16}$$

where $\eta_k = \sum_{i=1}^{M} \Gamma\left(u_{ik}\right)$ is the total number of pixels assigned to cluster k. We observed from equation (5.8) that the mean for the k^{th} Gaussian component μ_k is defined by using a weighted mean of all of the pixels in the data set, where the weighting factor for the image pixel point x_i is derived using the posterior probability $\Gamma\left(u_{ik}\right)$. Therefore a Gaussian component $\{k\}$ is responsible for generating the image pixel points x_i.

Similarly, we maximise $\ln\{P\left(X \mid \theta\right)\}$ with respect to the covariances Σ_k and we obtain

$$\Sigma_k = \frac{1}{\eta_k} \sum_{i=1}^{M} \Gamma\left(u_{ik}\right) \left(x_i - \mu_k\right) \left(x_i - \mu_k\right)^N \tag{3.17}$$

Like the mean μ_k, the denominator of (5.9) is defined by the total number of pixel points assigned to cluster k and each pixel point is weighted by the corresponding posterior probability.

Finally, setting the derivative of $\ln\{P(X \mid \theta)\}$ with respect to (π_k) the mixing coefficients and by using a Lagrange multiplier to satisfy the constraint $\sum_{k=1}^{K} \pi_k = 1$, we obtain

$$\ln\{P(X \mid \theta)\} + \lambda \left\{ \sum_{k=1}^{K} \pi_k - 1 \right\}$$

$$\sum_{i=1}^{M} \frac{(\pi_k \mathcal{N}(x_i \mid \mu_k, \Sigma_k))}{\sum_{j=1}^{K} (\pi_j \mathcal{N}(x_i \mid \mu_j, \Sigma_j))} + \lambda = 0 \tag{3.18}$$

By multiplying both sides of equation (3.18) and summing over k, we obtain the mixing coefficient as

$$\pi_k = \frac{\sum_{i=1}^{M} \Gamma(u_{ik})}{M} \tag{3.19}$$

From (3.19), we can see that the expression of the mixing coefficient for a component k is defined by the average responsibility that component k has for assigning image pixels.

In all, to perform the EM algorithm, we first choose initial values for Gaussians parameters (means, covariance and mixing coefficients), then the algorithm iterates between the E-step and the M-step [Bis07]. The EM algorithm process is summarised in Figure 3.6. In the E-step, the currents values of the parameters are used to calculate the values of the $\Gamma(u_{ik})$ the posterior probabilities (responsibilities) given by equation (5.7). These probabilities values are used in the M-step to re-calculate the values of the Gaussians parameters means, covariance and mixing coefficients derived in (5.8), (5.9), (3.19) respectively. However each update to the Gaussians parameters from the E-step and the M-step is guaranteed to increase the log likelihood. Figure 3.7(b) shows the experimental results of EM algorithm for the containing noises. To reduce these

noises, we applied the length filter operation in following section.

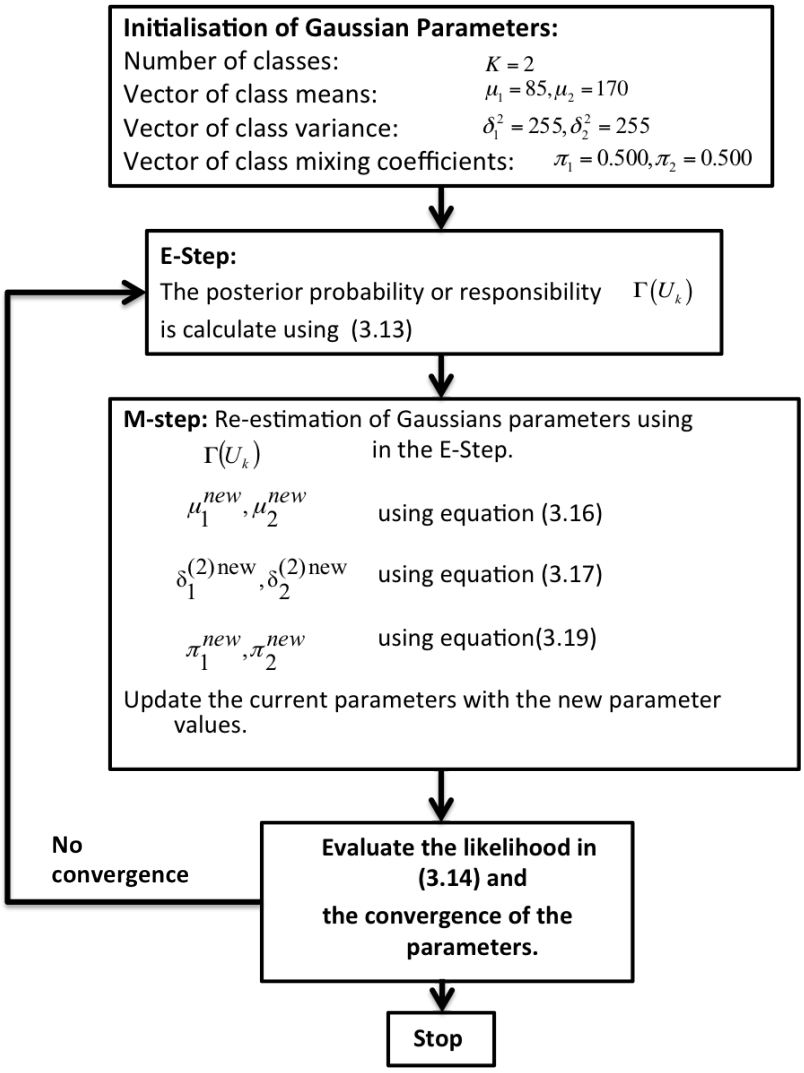

Figure 3.6: The EM algorithm summary.

Length Filter

The result of EM algorithm shown in Figure 3.7(a), exhibit some misclassified pixels indicated by the red arrows. This increases the false positive rate. To address this problem, the length-filtering model is designed to eliminate all the non-vessels pixels in the EM algorithm result image. We adapt the length filter used in [CF03], which

discards all the groups of pixels with pixel numbers less than a certain number of pixels. The approach uses connected pixels labelling model, in which each individual object in the image is defined as connected regions. The approach starts by identifying all the connected regions, then discards all the connected objects less than a certain number of pixels using an eight-connected neighbourhood of all surrounding pixels. Finally label propagation is used and all connected components larger than a certain number of pixels are labelled as blood vessels. This approach reduces significantly the false positive. The results of this operation is shown in Figure 3.7(b).

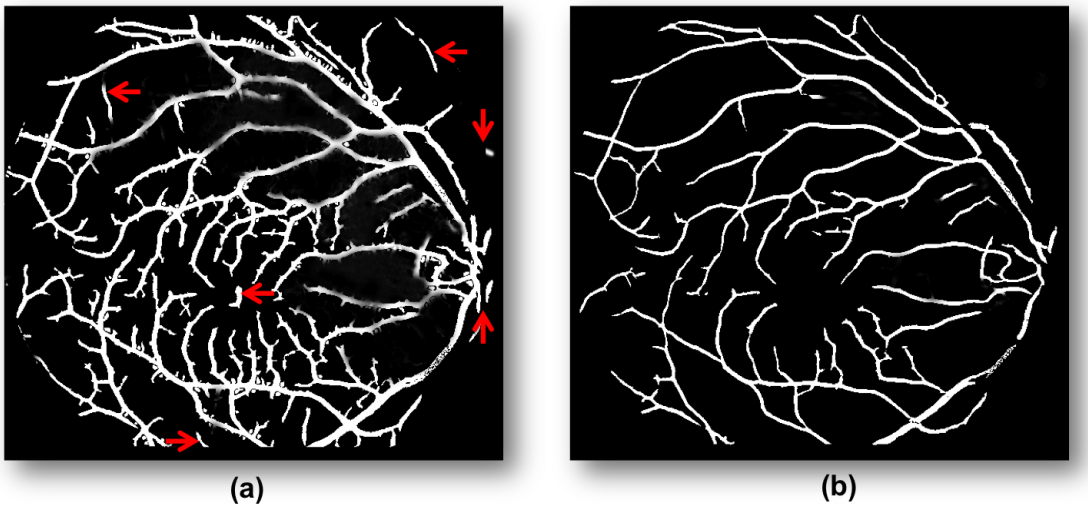

Figure 3.7: Example EM and Length Filter results. **(a)** EM result with misclassified pixels indicated by the red arrow. **(b)** Length filter result of the EM output.

3.4 Experimental results

The method presented in this paper was evaluated on two publicly available retinal image datasets: STARE [HKG02] and DRIVE [SAN+04a] containing 60 images in total with 25 of them showing a variety of lesions.

The STARE dataset contains 20 fundus colour retinal images, including 10 healthy and 10 unhealthy ocular fundus images with a variety of lesions. The images are

captured by a Topcon TRV-50 fundus camera at 35 ° field of view (FOV) and the size of the image is 700×605 pixels. The dataset provides two sets of hand labelled images segmented by two human experts as a ground truth for retinal vessel segmentation methods. We calculated the mask of the image for this dataset using a simple threshold technique for each colour channel. We adapt the first expert hand labelled image as the ground truth to evaluate our segmentation technique.

The DRIVE dataset provided 40 fundus colour ocular images, including 20 training and images, 20 test images including 15 images with a variety of lesions. These images are acquired using The Canon CR5 camera at 45 ° FOV, digitised at 24 bit with resolution of 565×584 pixels. The dataset also provides two sets of hand labelled images segmented by two human experts as ground truth. The first expert hand labelled image was adapted as ground truth in the evaluation on both the STARE and the DRIVE datasets.

To facilitate the performance comparison between our methods and other retinal blood vessels segmentation methods, the parameters measuring the performance (true positive rate, false positive rate and the accuracy rate) of [SAN+04a], [HKG02], [MC06b] were used to measure the performance of the segmentation. The true positive rate (TPR) is defined as the ratio of the total number of pixels correctly classified as vessel pixels to the total number of vessel pixels in the image ground truth. The false positive rate (FPR) is the ratio of the total number of non vessel pixels in the FOV classified as vessel pixels to the total number of non vessel pixels inside the FOV of the ground truth image. Finally the accuracy (ACC) is computed as the sum of true positives and true negatives over the total number of pixels in a given image. It is worth mentioning that a perfect segmentation would have a FPR of 0 and a TPR of 1. All the methods used the first expert hand labelled images as performance reference.

3.4.1 Segmentation Results on STARE Dataset

The experiment results of different retinal blood vessels segmentation methods on the STARE dataset are shown in Tables 3.1 and 3.2. The performance results of Staal et al. [SAN+04a], Mendona et al. [MC06b], Martinez-Perez et al. [MPHT+07b], Chaudhuri et al. [CCK+89a], Zhang et al. [ZZZK10] , and Hoover et al. [HKG02] were generated from their original manuscripts. The performance of the different methods was generated using all the 20 fundus images except the method presented by Staal [SAN+04a], that used 19 out of the 20 images including 10 healthy and 9 unhealthy images. Our Mixture of Gaussians has the highest average TPR = 0.7619 and with an average accuracy of 0.9456, it performs better than the methods presented by Mendoca et al. [MC06b], Hoover et al [HKG02], Chaudhuri et al. [CCK+89a] and Maritiner-Perez et al. [MPHT+07b] and its only marginally inferior to the method presented by Staal et al. [SAN+04a] and hang et al. [ZZZK10]. However as mentioned above the method presented by Staal et al. uses only 19 images for performance evaluation.

Method	TPR	FPR	Accuracy
2^{nd} human observer [MC06b]	0.8949	0.0610	0.9354
Mendonca [MC06b]	0.6996	0.0270	0.9440
Staal [SAN+04a]	0.6970	0.0190	0.9516
Chaudhuri [CCK+89a]	0.6134	0.0245	0.9384
Maritiner-Perez [MPHT+07b]	0.7506	0.0431	0.9410
Hoover[HKG02]	0.6751	0.0433	0.9267
Zhang [ZZZK10]	0.7177	0.027	0.9484
Gaussian Mixture Models [KSGL+13]	0.6645	0.0216	0.9450
Mixture of Gaussians	**0.7619**	**0.0328**	**0.9456**

Table 3.1: **The performance comparisons** - STARE dataset (Healthy and unhealthy retinal images)

We also compared the performance of our method on both healthy and unhealthy ocular images. The test on healthy retinal images in Table 3.2 shows that the Mixture of Gaussians achieves the highest average accuracy of (95.54%) compared to all other alternative methods. It also has the second highest average accuracy after [ZZZK10] in segmenting unhealthy retinal images.

Method	TPR	FPR	Accuracy
Unhealthy ocular images			
2^{nd} human observer [MC06b]	0.8252	0.0456	0.9425
Mendonca[MC06b]	0.6733	0.0331	0.9388
Hoover[HKG02]	0.6736	0.0528	0.9211
Chaudhuri [CCK+89a]	0.5881	0.0384	0.9276
Zhang [ZZZK10]	0.7166	0.0327	0.9439
Gaussian Mixture Models [KSGL+13]	0.6520	0.0255	0.9411
Mixture of Gaussians	**0.7068**	**0.0324**	**0.9417**
Healthy ocular images			
2^{nd} human observer [MC06b]	0.9646	0.0764	0.9283
Mendonca[MC06b]	0.7258	0.0209	0.9492
Hoover[HKG02]	0.6766	0.0338	0.9324
Chaudhuri [CCK+89a]	0.7335	0.0218	0.9486
Zhang [ZZZK10]	0.7526	0.0221	0.9510
Gaussian Mixture Models [KSGL+13]	–	–	–
Mixture of Gaussians	**0.8506**	**0.0300**	**0.9554**

Table 3.2: **The performance comparisons** - STARE dataset (Healthy vs Unhealthy retinal images)

3.4.2 Segmentation Results on DRIVE Dataset

Similarly to STARE dataset, The performance results of Staal [SAN+04a], Mendona [MC06b], Martinez-Perez [MPHT+07b], Chaudhuri [CCK+89a], Perfetti [PRCC07], Garq [GSC07], Al-Rawi [ARQA07] , Cinsdikici [CA09], Marin [MAGAB11] and Zhang [ZZZK10] were generated from their original manuscripts. But the performance results of Zana [ZK01] and Jiang [JM03] techniques were provided by Staal [SAN+04a] as their manuscripts were published before the DRIVE dataset was available. The performance of all the methods was based on the 20 test images and the results are shown in Table 3.3. An overview of the testing results show that our method outperforms all other methods in term of TFR and with the accuracy, its marginally inferior to the method presented by Staal et al. [SAN+04a], Marin et al. [MAGAB11], Mendona et al. [MC06b] and the performance of human experts. Nevertheless it is important to note that the methods presented Staal et al. and Marin et al. used supervised techniques that generally depend on the training datasets, hence good segmentation results are achieved by classifier

retraining before experimentations on new datasets.

Method	TPR	FPR	Accuracy
2^{nd} human observer [ZZZK10]	0.7761	0.0275	0.9473
Mendonca [MC06b]	0.7344	0.0236	0.9452
Staal [SAN+04a]	0.7194	0.0227	0.9442
Chaudhuri [CCK+89a]	0.6168	0.0259	0.9284
Maritiner-Perez [MPHT+07b]	0.7246	0.0345	0.9344
Jiang [JM03]	-	-	0.9112
Perfetti [PRCC07]	-	-	0.9261
Zana [ZK01]	-	-	0.9377
Garq [GSC07]	-	-	0.9361
Marin [MAGAB11]	-	-	0.9452
Al-Rawi [ARQA07]	-	-	0.9510
Cinsdikici [CA09]	-	-	0.9293
Zhang [ZZZK10]	0.7120	0.0276	0.9382
Mixture of Gaussians	**0.7466**	**0.0317**	**0.9410**

Table 3.3: **The performance comparisons** - DRIVE dataset

Figure 3.8 shows the experimental results of the proposed method, where 3.8(a-c) shows the input images, 3.8(d-f) the segmentation results and 3.8(g-i) the corresponding hand labelled blood vessel networks.

3.5 Summary

In this chapter, we describe a process of automated segmentation of the blood vessel networks in fundus retinal images using a mixture of Gaussians. This method can be used as a tool for non-invasive diagnosis in modern ophthalmology for mass patient screening, image registration and retinal disease evaluation and treatment. This method uses the bias correction as a pre-processing operation to remove noise and correct the intensity inhomogeneity across the image. An additional processing operation is used to enhance the appearance of the blood vessel network, including adaptive histogram equalisation (AHE) and distance transform, the latter operation allows the segmentation of narrow blood vessels.

The proposed method was tested on 60 fundus retinal images from two public

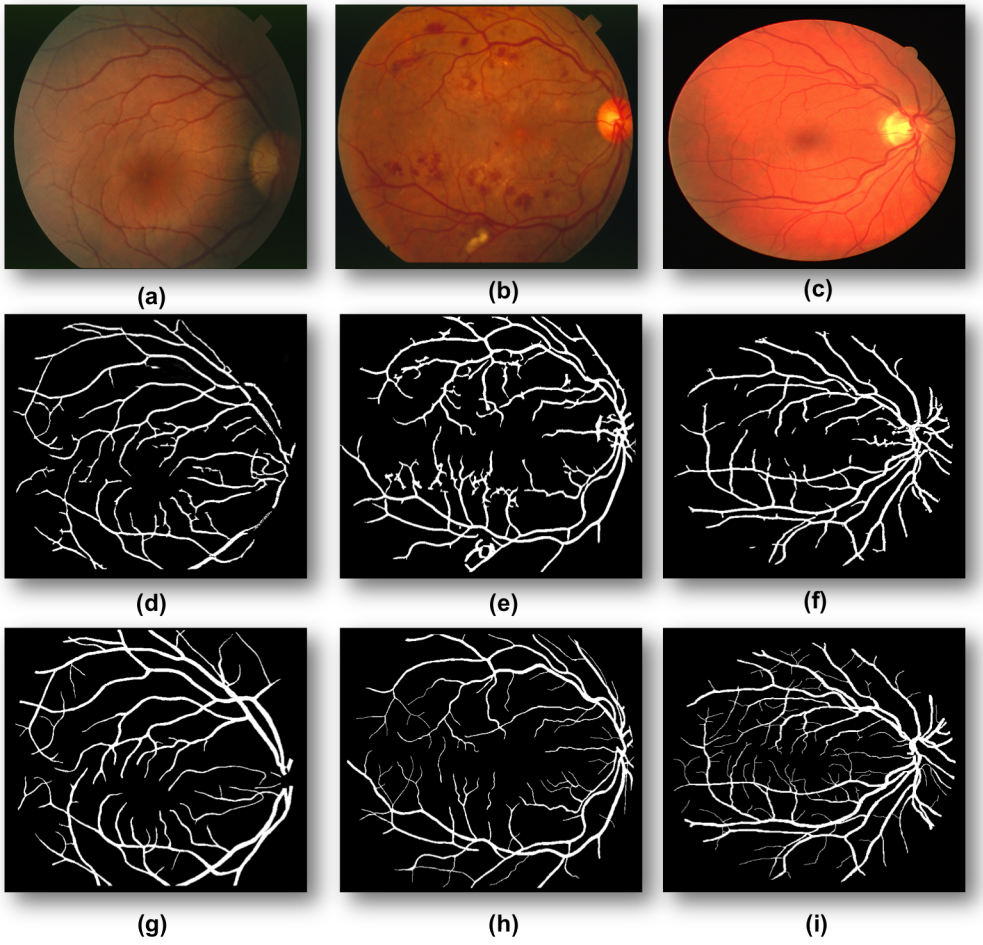

Figure 3.8: Sample results of our methods. **(a-b)** STARE input images and **(c)** DRIVE input image .**(d-f)** The corresponding segmentation results. **(g-i)** The corresponding hand labelled blood vessels.

datasets (STARE and DRIVE) including 25 images with a variety of lesions. The performance on these difficult datasets showed effective agreement with the manual annotations. The performance evaluations of the proposed method seen in Table 3.1, 3.2 and 3.3 show that our method outperforms most of the alternative methods we compared to in term of TPR, FPR and ACC.

This method has advantages over tracking-based methods because it applies bias correction and distance transform on retinal images to enhance vessel appearance and allows a complete segmentation of retinal blood vessel network. Also our method

achieves better results over other pixel processing based methods as it corrects the intensity inhomogeneity across retinal images to improve the segmentation of the narrow blood vessels. The Mixture of Gaussians method also minimises the segmentation of the optic disc boundary and lesions in the unhealthy retinal images. However, this is a low-level segmentation method because it combines three pre-processing operations, which analysis every pixels in the image. The bias correction operation can also remove the very thin blood vessels.

Chapter 4

Segmentation of Blood Vessels Using Graph Cut

This chapter presents our second contribution.

4.1 Introduction

The segmentation of retinal image structures has been of great interest because it could be used as a non-intrusive diagnosis tool in modern ophthalmology. The morphology of the retinal blood vessel is an important structural indicator for assessing the presence and severity of retinal diseases such as diabetic retinopathy, hypertension, glaucoma, haemorrhages, vein occlusion and neo-vascularisation. The ratio between the diameter of the retina arteries and veins can also indicate risks of systemic diseases including stroke, hypertension and myocardial infraction [AGS10]. However to assess the diameter and the tortuosity of retinal blood vessel, manual planimetry has commonly been used by ophthalmologist, which is generally time consuming and tedious, especially when the vessel structure are complicated or a large number of images are acquired to be labelled by hand. Therefore, a reliable automated method for retinal blood vessels segmentation is attractive in retinal image analysis.

An automated segmentation and inspection of retinal blood vessel features such as diameter, colour and tortuosity allows ophthalmologist and eye care specialists to perform mass vision screening exams for early detection of retinal diseases and treatment evaluation. This could prevent and reduce vision impairments, age related diseases and cut the costs of the eye screening. This examination can also prevent many cardiovascular diseases such as the risk of stroke and hypertension as shown in Figure 4.1.

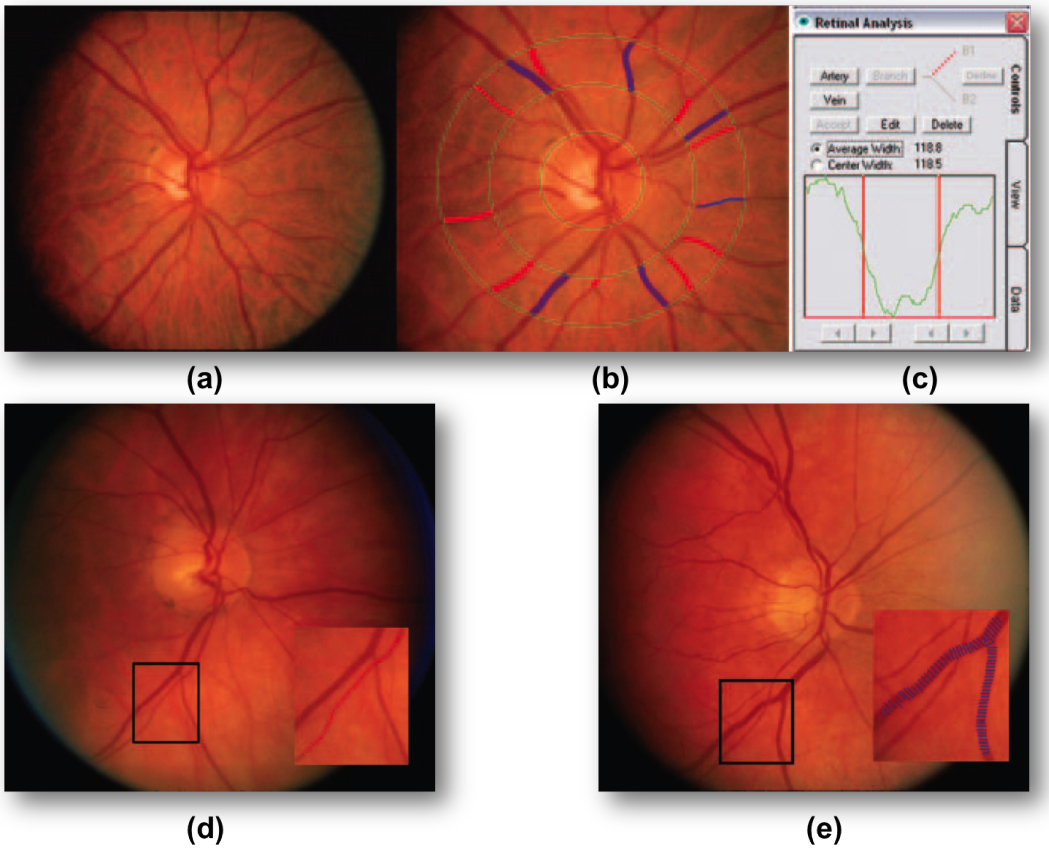

Figure 4.1: Retinal blood vessel evaluation. **(a)** Digital retinal image. **(b)** Measuring arteriolar and venular caliber. **(c)** Edge detection. **(d)** Retinal photograph of a patient showing narrow retinal arteriole, this patient developed severe hypertension within 10 years of the photography. **(e)** Retinal photograph of a patient showing wide retinal venule, this patient developed a fatal stroke within 10 years of the photograph. **(a-e)** [LWMW08].

In the literature, several segmentation techniques have been employed for the seg-

mentation of retinal blood vessel. However the acquisition of fundus retinal images under different conditions of illumination, resolution and field of view (FOV) and the overlapping tissue in the retina cause a significant degradation to the performance of automated blood vessel and segmentations. Thus, there is a need for a reliable technique for retinal vascular tree network extraction, which preserves various vessel shapes.

We reviewed a number of previous studies of retinal blood vessel segmentation in chapter 3. The segmentation methods were divided into two groups, pixel-processing-based and vessel tracking-based methods. Our graph cut method is implemented to address the issues in the Mixture of Gaussians method described in chapter 3, which is a low-level method as it uses three pre-processing operations and performs the vessel extraction by processing all the pixels in the fundus image. The graph cut method combines pixel-processing-based and vessel tracking-based methods by integrating the mechanism of flux into graph formation to achieve complete vessel network extraction including arrow vessels. The proposed method also applies a pre-processing technique including an adaptive histogram equalisation (AHE) and distance transform to enhance the appearance of the blood vessel in the retinal image.

4.2 Methods

Blood vessels can be seen as thin elongated structures in the retina, with variation in width and length. In order to segment the blood vessel from the fundus retinal image, we implemented a pre-processing technique, which consists of an effective AHE and robust distance transform. This operation improves the robustness and the accuracy of the graph cut algorithm. Fig. 4.2 shows the illustration of the vessel segmentation algorithm.

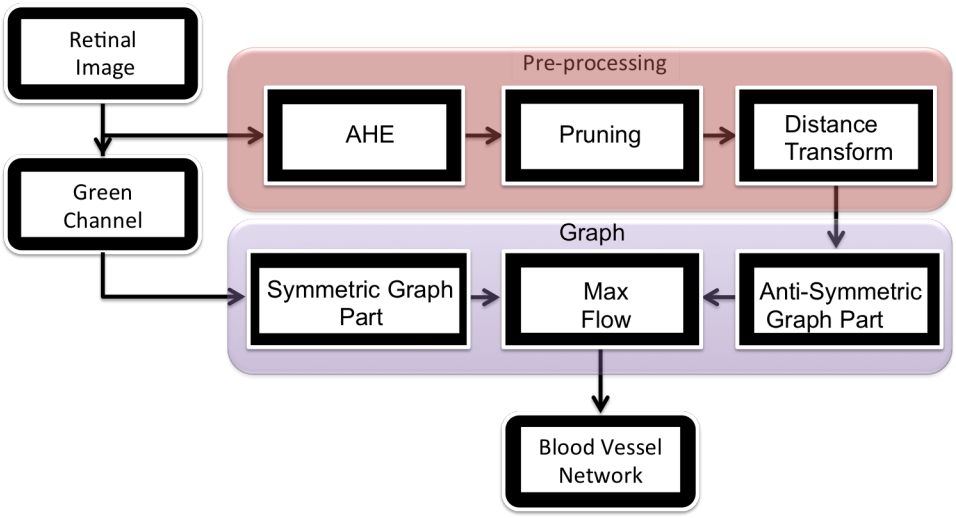

Figure 4.2: Vessel segmentation algorithm.

4.2.1 Pre-processing

We apply a contrast enhancement operation to the green channel of the input RGB (red, green, blue) retinal image, which displays a good contrast between the retinal blood vessel networks and the background similar to the work presented in [WZL06]. The intensity of the image is inverted, and the illumination is equalised. The resulting image is enhanced using an adaptive histogram equaliser, given by:

$$I_{Enhanced} = \left(\sum_{p' \in R(p)} \frac{s\left(I\left(p\right) - I\left(p'\right)\right)}{h^2} \right)^r \cdot M \tag{4.1}$$

where I is the green channel of the fundus retinal colour image, p denotes a pixel and $p^{'}$ is the neighbourhood pixel around p. $p^{'} \in R(p)$ is the square window neighbourhood with length h. $s(d) = 1$ if $d > 0$, and $s(d) = 0$ otherwise with $d = s\left(I\left(p\right) - I\left(p'\right)\right)$. $M = 255$ value of the maximum intensity in the image. r is a parameter to control the level of enhancement. Increasing the value of r and h would also increase the contrast between vessel pixels and the background as shown in Figure 4.3. The values of the window length was set to $h = 81$ and $r = 6$ by experimentation.

A binary morphological open process and the distance transform operation are

applied to prune and enhanced image. More information about this process is provided in Chapter 3 Section 3.3.2. This approach discards all the misclassified pixels and significantly reduces the false positive, since the enhanced image is used to construct the graph for the vessel segmentation process. Figure 4.3(e) shows the enhanced vessel or distance map image.

The distance map image is used to calculate the direction and magnitude of the vessel gradient. Figure 4.3(f) shows a sample vessel in the distance map image with black arrows indicating the direction of the gradients respectively. From the sample vessel image, we can see the centre line with the brightest pixels, which are progressively reduced in intensity in the direction of the edges (image gradients). The arrows in Figure. 4.3(f) referred as vector field, which is used to construct the graph in the next sections.

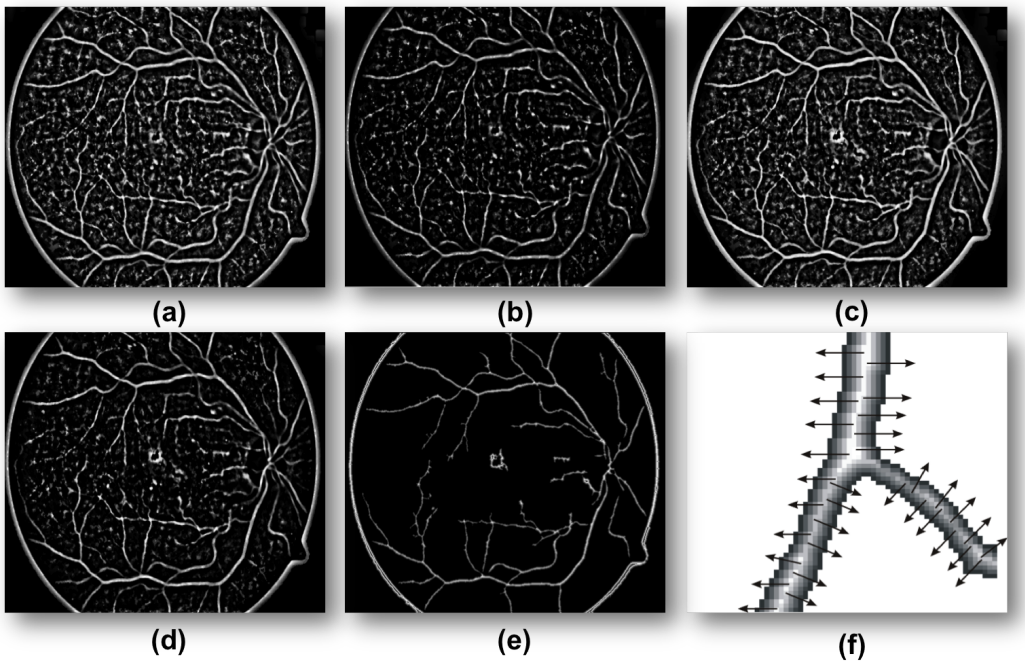

Figure 4.3: Pre-processing. **(a)** $h = 45, r = 3$. **(b)** $h = 45, r = 6$. **(c)** $h = 81, r = 3$. **(d)** $h = 81, r = 6$. **(e)** distance map. **(f)** sample of a vessel with arrows indicating the vessel gradients.

4.2.2 Graph construction

The graph cut is an energy based object segmentation approach. The technique is characterised by an optimisation operation designed to minimise the energy generated from a given image data. This energy defines the relationship between neighbourhood pixel elements in an image.

A graph $G(\nu, \epsilon)$ is defined as a set of nodes (pixels) ν and a set of undirected edges ϵ that connect these neighbouring nodes. The graph included two special nodes, a foreground terminal (source S) and a background terminal (sink T). ϵ includes two types of undirected edges: neighbourhood links (n-links) and terminal links (t-links). Each pixel $p \in P$ (a set of pixels) in the graph presents two t-links $\{p, S\}$ and $\{p, T\}$ connecting it to each terminal while a pair of neighbouring pixels $\{p, q\} \in N$ (number of pixel neighbour) is connect by a n-links [BJ01]. Thus:

$$\epsilon = N \bigcup_{p \in P} \{\{p, S\}, \{p, T\}, \nu = P \cup \{S, T\}\} \tag{4.2}$$

An edge $e \in \epsilon$ is assigned a weight (cost) $W_e > 0$. A cut is defined by a subset of edges $C \in \epsilon$ where $G(c) = \langle \nu, \epsilon \backslash C \rangle$ separating the graph into two foreground and background with C defined as $|C| = \sum_{e \in C} W_e$

The Max-Flow algorithm is used to cut the graph and find the optimal segmentation. Table 4.1 assigns weight to the edges ϵ in the graph [BJ01].

Edge	**Weight**	**For**
{p, q}	$B_{\{p,q\}}$	$\{p, q\} \in N$
{p, S} (Foreground)	$\lambda \cdot R_p(Fg)$	$p \in P, p \notin F \cup B$
	K	$p \in F$
	0	$p \in B$
{ p, T} (Background)	$\lambda \cdot R_p(Bg)$	$p \in P, p \notin F \cup B$
	0	$p \in F$
	K	$p \in B$

Table 4.1: **Weight assignment of the edges in the graph.**

where

$$K = 1 + max_{p \in P} \sum_{\{p,q\}} B_{p,q} \tag{4.3}$$

F and B represent the subsets of pixels selected as foreground and background respectively. Thus $F \subset P$ and $B \subset P$ such that $F \cap B = \emptyset$. $B_{p,q}$ defines the discontinuity between neighbouring pixels, and its value is large when the pixel intensities. $\lambda > 0$ is a constant coefficient, which we will define in the energy formulation of the graph.

The graph cut technique is used in our segmentation because it allows the incorporation of prior knowledge into the graph formulation in order to guide the model and find the optimal segmentation. Let's assume $A = (A_1, A_p, \dots A_P)$ a binary vector set of labels assigned to each pixel p in the image, where A_p indicate assignments to pixels p in P. Therefore, each assignment A_p is either in foreground (Fg) or background (Bg). Thus the segmentation is obtained by the binary vector A and the constraints imposed on the regional and boundary proprieties of vector A are derived by the energy formulation of the graph defined as

$$E(A) = \lambda \cdot R(A) + B(A) \tag{4.4}$$

where the positive coefficient λ indicates the relative importance of the regional term (likelihoods of foreground and background) R_A against the boundary term (relationship between neighbourhood pixels) B_A. The regional or the likelihood of the foreground and background is given by

$$R(A) = \sum_{p \in P} R_p(A_p) \tag{4.5}$$

and the boundary constraints is defined as

$$B(A) = \sum_{p,q \in N} B_{p,q} \cdot \phi(A_p, A_q) \tag{4.6}$$

where $\phi(A_p, A_q) = 1$ for $A_p \neq A_q$ and 0 Otherwise.

$$\mathrm{B}_{p,q} = \exp(-\frac{(I_p - Iq)^2}{2\sigma^2}) \cdot \frac{1}{dist(p,q)} \tag{4.7}$$

$R_p(A_p)$ specifies the assignment of pixel p to either the foreground (Fg) or the background (Bg). $B_{p,q}$ defines the discontinuity between neighbouring pixels, and it's value is large when the pixel intensities I_p and I_q are similar and close to zero when they different. The value of $B_{p,q}$ is also affected by the Euclidean distance $dist(p,q)$ between pixels p and q.

During the minimisation of the graph energy formulation in (4.4) to segment thin objects like blood vessels, the second term (boundary term) in (4.4) has a tendency to follow short edges known as "the shrinking bias" [VKR08]. This problem causes a significant degradation on the performance of the graph cut algorithm on thin elongated structures like the blood vessels. Figure 4.4 shows an example of the blood vessel segmentation using the traditional graph formulation [KB05]. From Figure 4.4, it can be seen that the blood vessel segmentation follows short edges, and tends to shrink in the search for the cheapest cost. It can also be noticed that λ in (4.4) controls the relation between boundary and regional terms. Increasing the value of λ, the likelihood of the pixels belonging to foreground and background (t-links) gains strength over the regional term (n-links), which slightly improved the segmentation result see Figure 4.4(d).

To address the above problem, the segmentation of blood vessels using the graph cut requires special graph formulation. One of the method used to address the shrinking bias problem is to impose an additional connectivity prior, where the user marks the constrain connectivity [VKR08]. In order to achieve full automated segmentation, we used the method presented in [KB05], which overcomes the "the shrinking bias" by adding the mechanism of vectors flux into the construction of the graph. The incorporation of vectors flux can improve edge alignment and allows the segmentation of

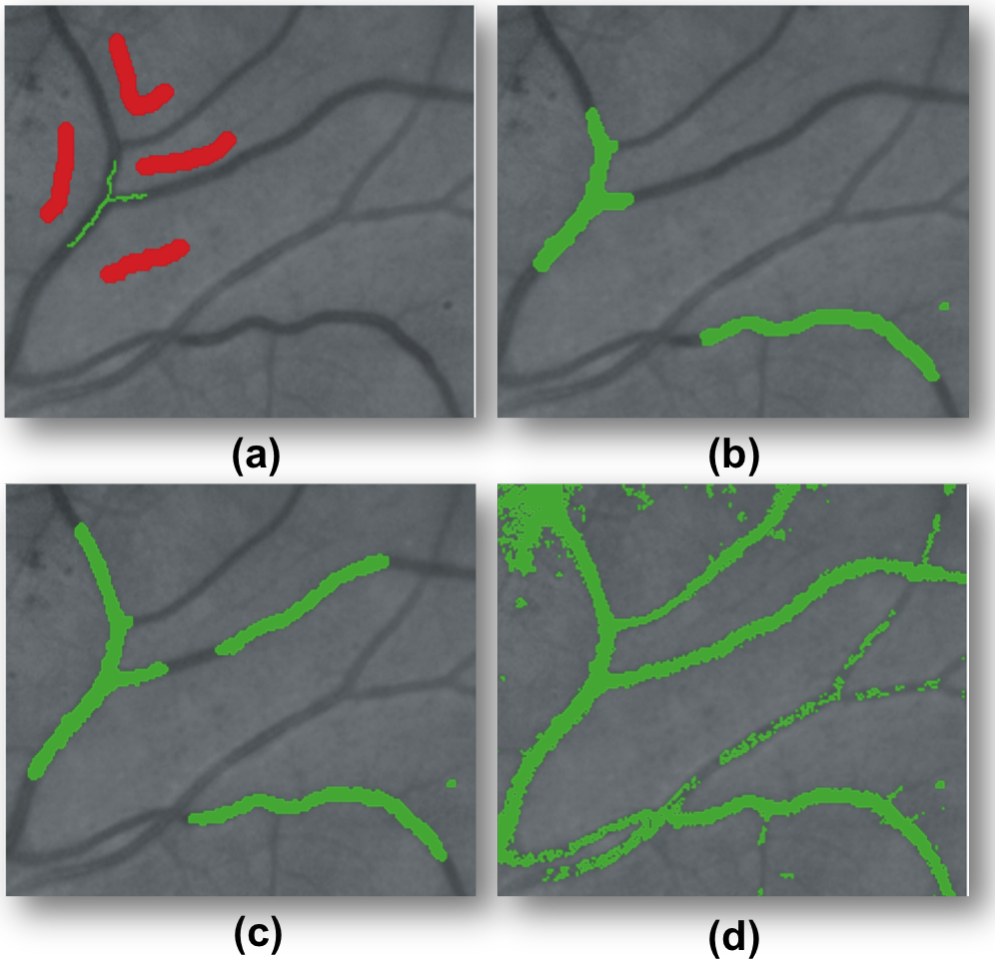

Figure 4.4: Retinal blood vessel segmentation using the traditional graph. **(a)** seeds initialisation of the input image: red background and green vessels. **(b)** $\lambda = 20$. **(c)** $\lambda = 50$. **(d)** $\lambda = 100$. Segmented blood vessel networks in green **(b-d).**

thin objects like blood vessels by keeping a balance between shrinking (length) and stretching (vectors flux) along the boundary. Figure 4.5 shows flux of vectors $\mathbf{v}$ passing through a given surface S. Our method takes the image gradients of rough blood vessels from the pre-processing step as vectors $\mathbf{v}$ see Figure 4.3(f), and the flux (magnitude, and direction) of these vectors is incorporated into the graph construction and optimised. Thus the shrinking effect of the minimization energy on the boundary term is equilibrated with the spreading effect of vectors $\mathbf{v}$ flux.

It is been shown in [KB05] that the class of Finsler metrics can described geo-

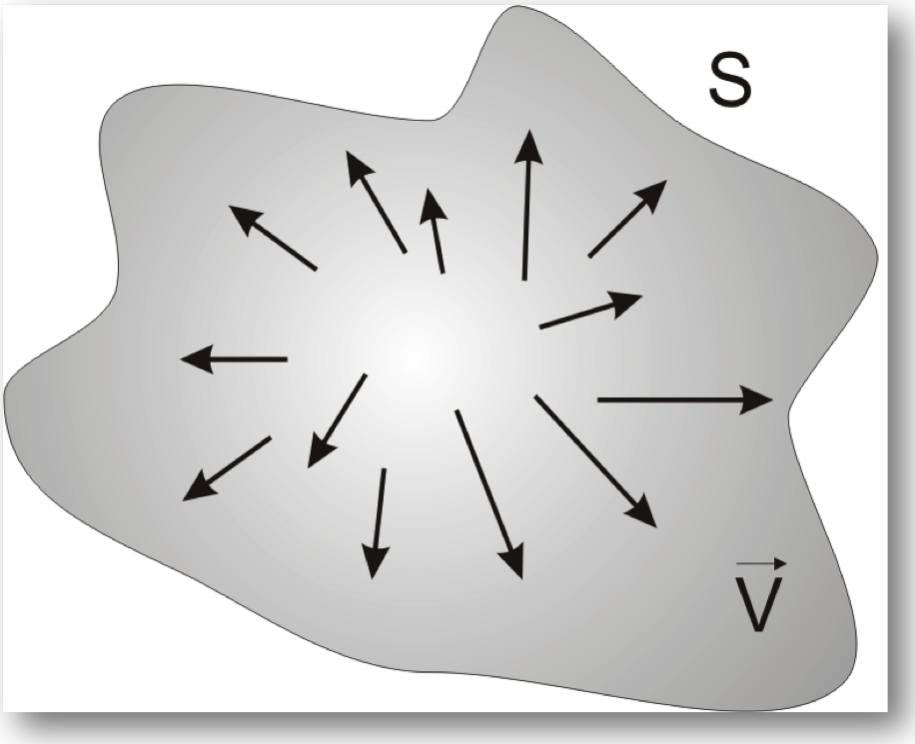

Figure 4.5: The flux of vectors **v** passing through a given surface S.

metric proprieties of the discrete cut metric on regular grids and Finsler length can be represented by the sum of two terms. Those terms represent the symmetric and anti-symmetric parts of the cut metric. The symmetric part of the cut defines the standard geometric length of contour and it is independent of its orientation. The anti-symmetric part of the cut metric represents the flux of a given vector field through the contour [KB05].

To address "the shrinking bias" problem seen in Figure 4.4, we have constructed a graph consisting of a symmetric part g^+ (shrinking) and an anti-symmetric part g^- (stretching) by incorporating the flux of vector **v** into the graph construction. The symmetric part g^+ of the graph corresponds to a cut geometric length and is related directly with the n-link connections and the anti-symmetric part g^- is equal to flux of vector field **v** over the cut geometric and it is used to derive the t-links. Thus the blood

vessels can be segment by keeping a good balance between shrinking and stretching (flux) throughout the image boundary.

The Symmetric Part of the Graph

The symmetric part of the graph is used to assign weights on the n-link connections (edges between neighbouring pixels). Let consider a neighbour system of a graph described by a set of edges e_k, where $1 \leq k \leq N$, for N number of neighbours. Let us define e_k as the shortest vector connecting two pixels in the direction of k, $W_k^+(p)$ the weight of the edge e_k at pixel p and $\widetilde{W}_k^+(p)$ a set of the edge weights at pixel p for all directions. The corresponding edge weights are defined by

$$\omega^+ = \frac{1}{2} D \times g^+ \tag{4.8}$$

where D is a N x N matrix with entries defined as

$$D_{ii} = -\frac{sin(\alpha_{i+1} - \alpha_{i-1})}{sin(\alpha_{i+1} - \alpha_i) sin(\alpha_i - \alpha_{i-1})} \tag{4.9}$$

$$\text{If } j + 1 = \pm 1$$

$$D_{ij} = \frac{1}{sin\,(\alpha_j - \alpha_i)}$$

$$D_{ij} = 0 \text{ Otherwise}$$

where α_k is the angle of the edge e_k with respect to the positive axis X see Figure 4.6.

In our implementation, we consider a grid map of 16 neighbours with edges $e_k, k = 1, 2, ..., 16$ as seen in Figure 4.6. For each pixel p in the green channel image, the edge weight $\widetilde{W}_k^+(p)$ is computed according to (4.8). g^+ is calculated using the pixel intensity difference between two given nodes by:

$$g^+ = K \cdot exp\left(\frac{-(I_p - I_q)^2}{\sigma^2}\right) \tag{4.10}$$

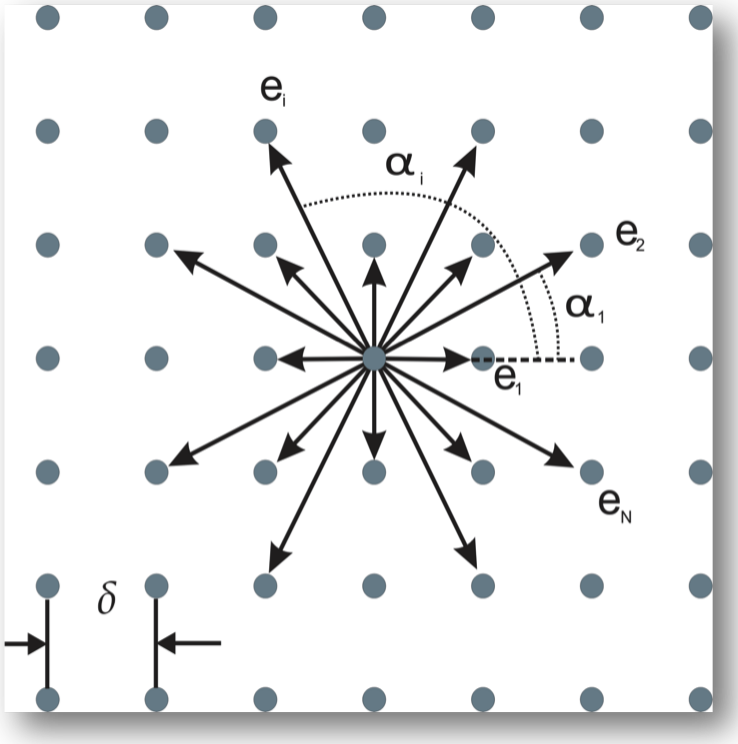

Figure 4.6: Neighborhood system for a grid in the graph.

g^+ has a high value for pixels of similar intensities, when $I_p - I_q < \sigma$. However if the pixels are very different $I_p - I_q > \sigma$ the value of g^+ is small, which represents a poor relation between the pixels, hence they belong to different terminals [BFL06].

The Anti-Symmetric Part of the Graph

We used the term Anti-Symmetry because, the flux (stretching) of vector field $\mathbf{v}$ over the cut geometric balanced the shrinking of blood vessels during the segmentation. This anti-symmetric part of the graph is defined by the flux of vector field $\mathbf{v}$ over the cut geometric. It is used to assign weights on the t-links (edges between a given pixel and the terminals) to balance the shrinking effect seen in Figure 4.4. Specific weights for t-links are obtained based on the decomposition of vector $\mathbf{v}$. Different decompositions of vector$\mathbf{v}$ may result in different t-links whose weights can be interpreted as an estimation of divergence. In our implementation, we decomposed the vector $\mathbf{v}$ along grid edges

with the n-links oriented along the main axes, X and Y direction. Thus vector $\mathbf{v}$ can be decomposed as $\mathbf{v} = v_x u_x + v_y u_y$ where u_x andu_y are unit vectors in X and Y direction respectively. This decomposition leads to the t-link weights defined as

$$t_p = \frac{\delta^2}{2}[\left(v_x^{right} - v_x^{left}\right) + \left(v_y^{up} - v_x^{down}\right)] \tag{4.11}$$

where v_x^{right} and v_x^{right} are the components of vector $\mathbf{v}$ in X direction taken at the right and left neighbour of pixel P respectively. v_y^{up} and v_y^{down} are the Y of vector $\mathbf{v}$ taken at the top and down of of pixel P. δ is the size of the cell in the grid map see Figure 4.6. We add edge $(s \rightarrow p)$ with weight $C * (-tp)$ if $tp < 0$, or edge $(p \rightarrow t)$ with weight $C * tp$ otherwise. The parameter C is related to the magnitude of the vector $\mathbf{v}$, thus pixels in the centre of the blood vessel have a higher connection to the source (foreground) than pixels in the edge of the blood vessels. Because the distance map is calculated on the pruned image and vector $\mathbf{v}$ is only defined for the pixels detected as blood vessels in the rough segmentation. For the rest of the pixels in the image, the initialisation of t-link weights is set as $(p \rightarrow s)$ with weight $t = 0$ and $(p \rightarrow t)$ with weight $t = K$, where K is the maximum weight sum for a pixel in the symmetric construction. Figure 4.7 shows the segmentation results of the blood vessels using different decomposition of the vector $\mathbf{v}$ generating different t-link weights.

4.3 Experiments

4.3.1 Data

For the vessel segmentation method, we tested our algorithm on two public datasets, DRIVE [SAN+04b], STARE [HKG00] with a total of 60 images including 25 images with some variety of lesions.

The DRIVE consists of 40 digital images including 15 images with a variety of lesions, which were captured from a Canon CR5 non-mydriatic 3CCD camera at 45° field of view (FOV). The images have a size of 768×584 pixels. The dataset includes

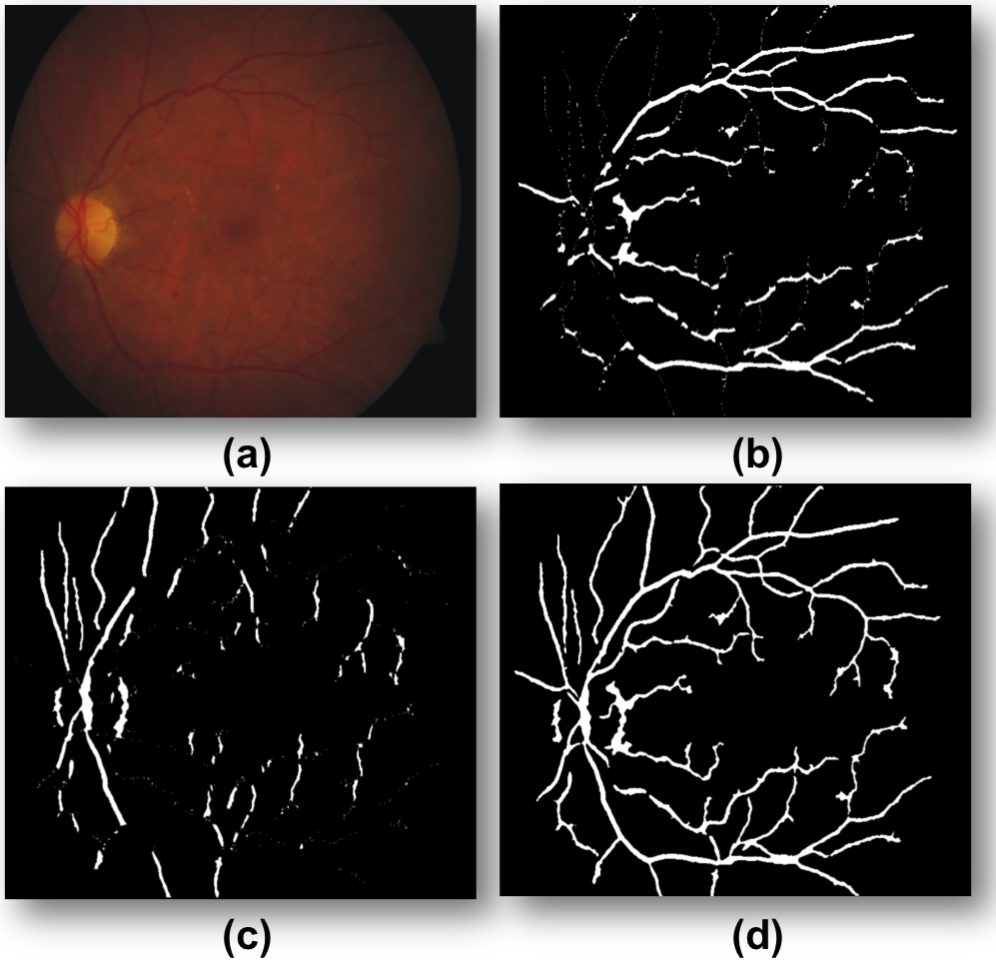

Figure 4.7: Vessel segmentation using the decomposition of vector **v**: **(a)** input retinal image. **(b)** Blood vessel segmentation using horizontal (X axis) decomposition of vector **v**. **(c)** Blood vessel segmentation using vertical (Y axis) decomposition of vector **v**. **(d)** Blood vessel segmentation result using the decomposition of vector **v** along X and Y axes.

masks to separate the FOV from the rest of the image. It included two sets hand labelled images (set A and set B) for the blood vessel. The set A offers the manually labelled images for all the images in the dataset, whereas the set B provides the manually labelled images for half of the dataset. To test our method we adopt the set A hand labeled images as the benchmark. We manually delimited the optic disc to test the performance of optic disc segmentation algorithm.

The STARE dataset consists of 20 images including 10 unhealthy images with a variety of lesions captured by a TopCon TRV-50 fundus camera at 35° FOV. The size of the images is 700×605 pixels. We calculated the mask image for this dataset using a simple threshold technique for each colour channel. The STARE dataset included images with retinal diseases selected by Hoover et al [HKG00]. It also provides two sets of hand labelled images performed by two human experts. The first expert labelled fewer vessel pixels than the second one. To test our method we adopt the first expert hand labelling as the ground truth.

The performance of the proposed method is compared to alterative retinal blood vessels segmentation approaches in the literature in term TPR, FPR and ACC defined in Section 3.4. Our method and all the alternative methods used the first expert hand labelled images as performance reference.

Most of the alternative methods use the whole image to measure the performance. In [SAN+04b] all the experiments, are done on the FOV without considering the performance in the dark area outside the FOV. The method in [MC06a] measures the performance on both the whole image and the FOV. The dark background outside the FOV in the retinal image is easy to segment. It is an advantage in measuring the true negatives pixels when the whole image is considered. We have calculated the percentage of pixels outside the FOV in the images for the two datasets, which represents approximately the 25% of the pixels in the whole image. However, it does not affect all the measurement metrics, except when the true negative value is involved (e.g. accuracy rate). On the other hand, most of the methods use the whole image to measure their performance, making the comparison fair.

4.3.2 Results of Blood Vessel Segmentation Algorithm on STARE dataset

Tables 4.2 and 4.3 show performance comparison results of our approach with recent alternative methods in terms of TPR, FPR and ACC on STARE dataset. The perfor-

mance results of the second expert hand labelled and the method of Martinez-Perez et al. [MPHT+07a] and Staal et al. [SAN+04b] are taken from [MPHT+07a]. The results of the methods proposed by Mendonca et al. [MC06a] and Hoover et al. [HKG00] are taken from [MC06a] and the approaches of Chaudhuri et al. [CCK+89b], Kaba et al. [KSGL+13] and Marin et al. [MAGAB11] and Zhang et al. [ZZZK10] were generated from their original manuscripts. The performance of the segmentation results for Zhang et al. [ZZZK10], Chaudhuri et al. [CCK+89b] and Soares et al. [SLC+06b] on both healthy and unhealthy images were taken from [ZZZK10]. The testing includes all the 20 fundus images except the method proposed by Staal [SAN+04b] which used 19 out of the 20 (10 healthy and 9 unhealthy) images.

In Tables 4.2 the second human expert hand labelled image is considered as the target performance level with average ($TPR = 0.7887$) given that the first human expert hand labelled image was the benchmark. Thus our method needs an improvement of 10.64% in average true positive whereas Mendona et al., Staal et al., Chaudhuri et al., Hoover et al., Kaba et al., Martinez-Perez et al. and Zhang et al. have a room of improvement of 19.55%, 19.81%, 28.17%, 22.00%, 23.06%, 14.45% and 17.74% respectively.

Method	TPR	FPR	Accuracy
2^{nd} **human expert** [MPHT+07a]	0.8951	0.0438	0.9522
Hoover[HKG00]	0.6751	0.0433	0.9267
Staal[SAN+04b]	0.6970	0.0190	0.9541
Mendonca[MC06a]	0.6996	0.0270	0.9440
Martinez[MPHT+07a]	0.7506	0.0431	0.9410
Chaudhuri[CCK+89b]	0.6134	0.0245	0.9384
Kaba [KSGL+13]	0.6645	0.0216	0.9450
Zhang [ZZZK10]	0.7177	0.0247	0.9484
Marin [MAGAB11]	-	-	0.9526
Our method	0.7887	0.0367	0.9441

Table 4.2: **Performance comparison of all images (healthy and disease).** - STARE dataset.

Considering the value of average TPR as performance measure, our proposed ap-

Heathy images			
Method	**TPR**	**FPR**	**Accuracy**
Mendonca[MC06a]	0.7258	0.0209	0.9492
Hoover[HKG00]	0.6766	0.0338	0.9324
Chaudhuri[CCK+89b]	0.7335	0.0218	0.9486
Zhang [ZZZK10]	0.7526	0.0221	0.9510
Soares [SLC+06b]	0.7554	0.0188	0.9542
Our method	0.8717	0.0364	0.9513
Unhealthy images			
Method	**TPR**	**FPR**	**Accuracy**
Mendonca[MC06a]	0.6733	0.0331	0.9388
Hoover[HKG00]	0.6736	0.0528	0.9211
Chaudhuri[CCK+89b]	0.5881	0.0384	0.9276
Zhang [ZZZK10]	0.7166	0.0327	0.9439
Soares [SLC+06b]	0.6869	0.0318	0.9416
Our method	0.7057	0.0371	0.9369

Table 4.3: **Performance comparison of healthy versus disease images.** - STARE dataset.

proach reaches better performance than all the other methods. However with the average accuracy rate, our method is only marginally inferior to the methods presented by Staal et al. [SAN+04b], Kaba et al. [KSGL+13], Marin et al. [MAGAB11] and Zhang et al. [ZZZK10] but as mentioned above, Staal et al. [SAN+04b] used 19 of the 20 images. Compared to the methods proposed by Hoover et al. [HKG00], Martinez-Perez et al. [MPHT+07a] and Chaudhuri et al. [CCK+89b], our approach outperforms the accuracy rate of these techniques and it has approximately the same value of ACC as Mendonca et al. [MC06a].

Table 4.3 compares the performance of the healthy subject images against the unhealthy subject images on STARE dataset. The results of the experiments show the unhealthy ocular images cause a significant degradation to the performance of automated blood vessels segmentation techniques. An overview of the results shows on both healthy and unhealthy images, our proposed method achieves better overall average TPR performance than all the methods. However the average ACC value is comparable to the performance of Soares et al. [SLC+06b] and Zhang et al. [ZZZK10].

It outperforms the ACC of Mendonca et al. [MC06a], Hoover et al. [HKG00] and Chaudhuri et al. [CCK+89b] on both healthy and unhealthy images.

Figure 4.8 shows sample results of the proposed method and the manually labelled images for STARE data set.

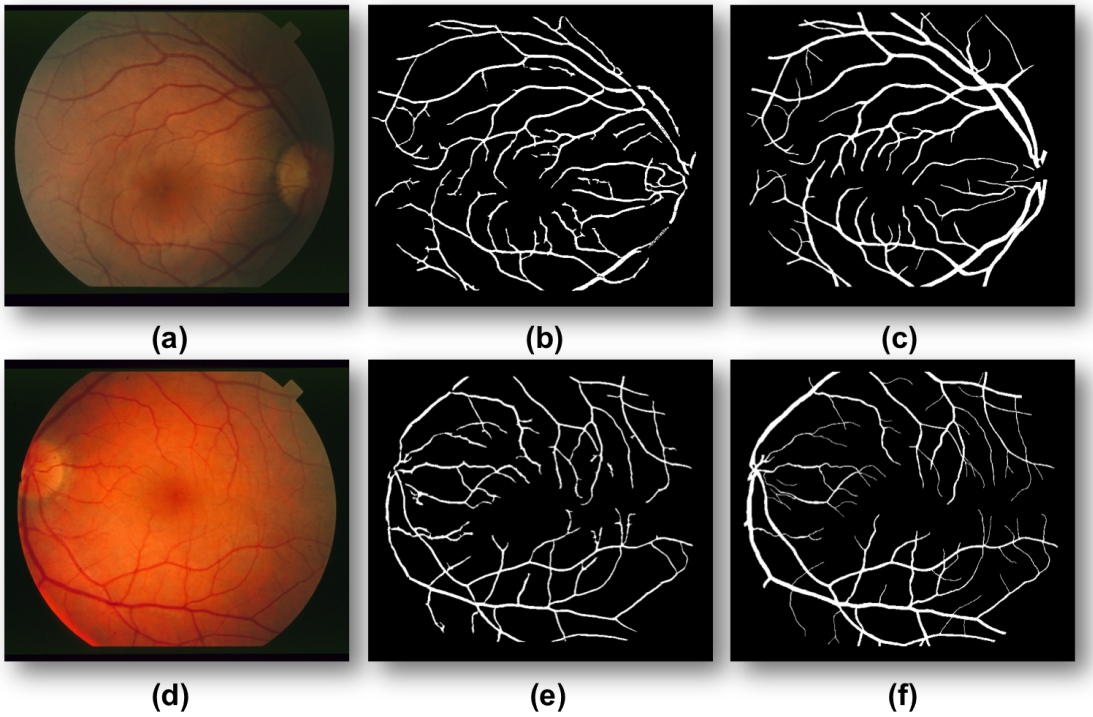

Figure 4.8: The STARE dataset: **(a)** and **(d)** retinal images. **(b)** and **(e)** Our segmentation results. **(c)** and **(e)** Manually labelled results.

4.3.3 Results of Blood Vessel Segmentation Algorithm on DRIVE dataset

The performance of the segmentation using our method on DRIVE dataset is compared with alternative methods: Zhang et al. [ZZZK10], Soares et al. [SLC+06b], Zana et al. [ZK01], Garg et al. [GSC07], Perfetti et al. [PRCC07], Al-Rawi et al. [ARQA07] taken from [ZZZK10]. The results of the second human expert B and the method proposed by Niemeijer et al. [NSvG+04], Mendonca et al. [MC06a] and Staal et al. [SAN+04b]

were acquired from [MC06a]. Cinsdikici et al. [CA09] and Jiang et al. [JM03] were generated from Marin et al. [MAGAB11] and finally Ricci et al. [RP07], Soares et al. [SLC+06b]and Martinez-Perez et al. [MPHT+07a] were used from their original manuscripts.

Method	TPR	FPR	Accuracy
Human expert B[MC06a]	0.7761	0.0275	0.9473
Staal[SAN+04b]	0.7194	0.0227	0.9442
Mendonca[MC06a]	0.7344	0.0236	0.9452
Niemeijer[NSvG+04]	0.6898	0.0304	0.9417
Jiang[JM03]	-	-	0.8911
Cinsdikici [CA09]	-	-	0.9293
Marin [MAGAB11]	-	-	0.9452
Ricci[RP07]	-	-	0.9633
Zana[ZK01]	-	-	0.9377
Garg[GSC07]	-	-	0.9361
Perfetti[PRCC07]	-	-	0.9261
Al-Rawi[ARQA07]	-	-	0.9510
Soares[SLC+06b]	-	-	0.9466
Zhang[ZZZK10]	0.7120	0.0276	0.9382
Martinez[MPHT+07a]	0.7246	0.0345	0.9344
Our method	0.7512	0.0316	0.9412

Table 4.4: **Performance comparison of all images (healthy and disease).** - DRIVE dataset.

The second human expert B hand labelled image [MC06a] is considered as the target performance level with average ($TPR = 0.7761$) and ($ACC = 0.9473$) given the first human expert A hand labelled image as reference (benchmark). Tables 4.4 shows the performance of our method against the above methods on DRIVE dataset. Our method needs an overall improvement of 2.49% and 0.61% in average true positive rate and average accuracy rate respectively.

Whereas with an average TPR rate of 0.7512, our method achieves better performance than all the other methods with respect to the average TPR value. The average accuracy achieved with our approach on DRIVE outperforms Jiang et al. [JM03], Cinsdikici et al. [CA09], Zana et al. [ZK01], Garg et al. [GSC07], Zhang et al. [ZZZK10] and Martinez et al. [MPHT+07a]. But it is marginally inferior to the methods proposed

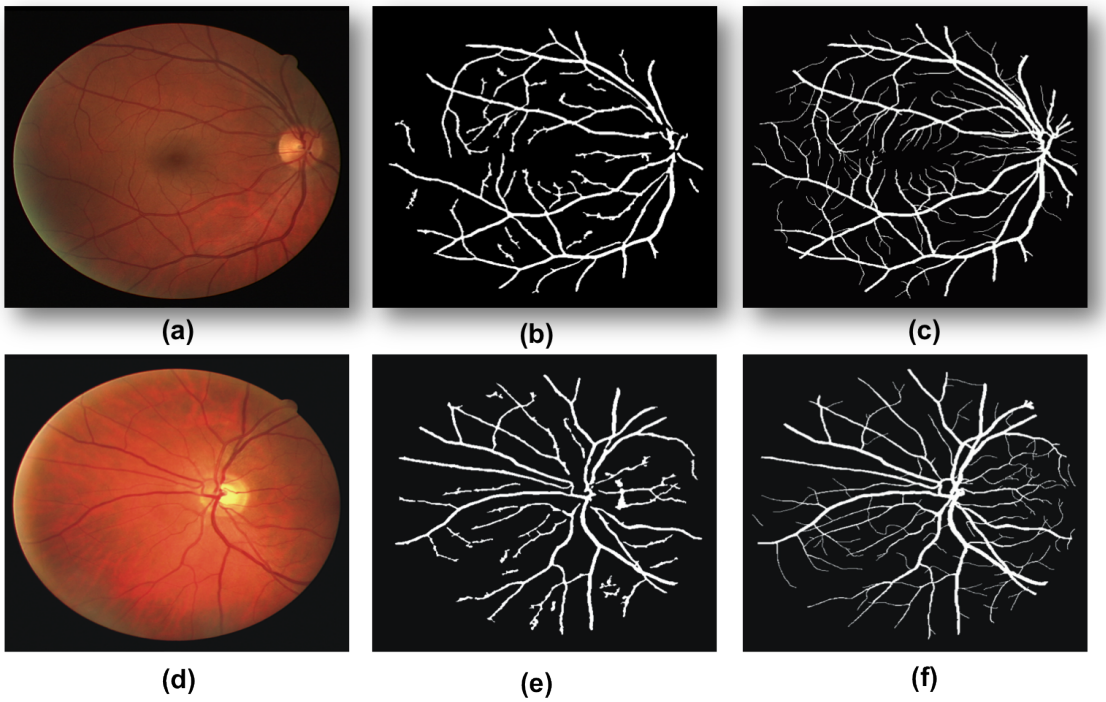

Figure 4.9: The DRIVE dataset: **(a)** and **(d)** retinal images. **(b)** and **(e)** our segmentation results. **(c)** and **(e)** Manually labelled results.

by Al-Rawi et al. [ARQA07], Ricci et al. [RP07] and Mendonca et al. [MC06a] and it is comparable to Soares et al. [SLC+06b], Marin et al. [MAGAB11], Niemeijer et al. [NSvG+04] and Staal et al. [SAN+04b].

It is important to note that the methods presented by Ricci et al. [RP07], Soares et al. [SLC+06b], Marin et al. [MAGAB11], Niemeijer et al. [NSvG+04] and Staal et al. [SAN+04b] used supervised techniques that generally depend on the training datasets, thus to achieve a good results, classifier re-training is required before performing any experimentation on new datasets.

Figure 4.9 shows sample results of our segmentation method and the manually labelled images for DRIVE data set. An overview of the testing results on DRIVE in Table 4.4 shows that our method offers a reliable and robust segmentation solution for blood vessels. It is clearly observed that our approach reaches better performance in

terms average true positive rate.

4.4 Summary

This chapter describes a process of automated segmentation of the blood vessel network in fundus retinal images. The method can be used as a tool for non-invasive diagnosis technique in modern ophthalmology for mass patient screening, image registration and retina diseases evaluation and treatment. In order to perform the segmentation of the blood vessel network in the fundus retinal photography, the algorithm starts by enhancing the appearance of the blood vessel in the image. This operation known as pre-processing includes an AHE and distance transform. The results of this operation improve the robustness and the accuracy of the graph cut segmentation. The energy formulation of the graph is constructed by integrating the mechanism of flux into the graph cut algorithm. This allows the segmentation of thin blood vessels in the retinal image. The proposed method is tested on 60 fundus retinal images from two public datasets (STARE and DRIVE) including 25 images with a variety of lesions. The performance of the method was also compared against 10 and 15 other methods on STARE and DRIVE data sets respectively. The performance of our method on these difficult datasets demonstrated effective agreement with the manual annotation. The evaluations also show that our method achieved exceptional performance against the alternative methods it was compared to. The proposed method also outperforms our pervious method proposed in Chapter 3, as it is capable of segmenting small and thinner blood vessels.

Tables 4.2, 4.3 and 4.4 show performance comparison in terms of average true positive rate, false positive rate and accuracy rate. According to these results, our vessel segmentation algorithm reaches a acceptable results and outperforms all other methods in terms of average true positive rate on both STARE and DRIVE images. In terms of average accuracy, our method outperforms Hoover et al. [HKG00], Martinez-Perez

et al. [MPHT+07a] and Chaudhuri et al. [CCK+89b] on Stare images. On DRIVE it performs better than Jiang et al. [JM03], Cinsdikici et al. [CA09], Zana et al. [ZK01], Garg et al. [GSC07], Zhang et al. [ZZZK10] and Martinez et al. [MPHT+07a]. Nevertheless our method is marginally inferior to the methods presented by Staal et al. [SAN+04b], Kaba et al. [KSGL+13], Marin et al. [MAGAB11] and Zhang et al. [ZZZK10] on STARE and Al-Rawi et al. [ARQA07], Ricci et al. [RP07] and Mendonca et al. [MC06a], Soares et al. [SLC+06b], Marin et al. [MAGAB11] and Staal et al. [SAN+04b] on DRIVE. Although Soares et al. [SLC+06b], Marin et al. [MAGAB11], Staal et al. [SAN+04b] and Ricci et al. [RP07] seems to achieve higher accuracy, as supervised techniques, they generally depend on the training datasets, thus to achieve excellent results, classifier re-training is required before performing any experimentation on new datasets. Further studies in [MAGAB11] proved that these methods perform well when both training and testing are applied on the same dataset but the performance deteriorated when the method is tested and trained on different datasets. Since these methods are sensitive to the training datasets, deploying them for practical use in retinal blood vessel segmentation would need further improvements as segmentation algorithms must work on retinal images taken under different conditions to be effective.

Our propose method incorporates prior knowledge of blood vessels to perform the segmentation and it can be applied on retinal images from multiple sources and under different conditions without a need for training. This can be seen in the results achieved by this method on both STARE and DRIVE datasets.

Chapter 5

Optic Disc Detection in Fundus Retinal Images

In this chapter we present our third contribution.

5.1 Introduction

The optic nerve head or optic disc is described in a colour fundus images as a bright yellowish round area in the retina where the blood vessels converge with a shape that is approximately elliptical. Its size varies from one patient to another and generally it has a width of 1.8 ± 0.2 mm and height 1.9 ± 0.2 mm [SBCW99]. This area of the retina is considered as one of the most important structure of the eye. The blood vessels in the retina converge into the optic nerve to provide blood to the upper layers of the retina, it also allows the flow of information from the eye to the brain for further analysis [HG03]. In general retinal diseases manifest gradually on early stages without affecting the entire retina. However optic nerve pathology, in contrast to most of the retinal diseases can cause more severe damages in early stages, because of the essential role it plays for vision [HG03], [Oys99].

The optic disc is known to be the visible region of a 2-D view optic nerve [HG03].

Fundus images analysis of the optic disc has been of great interest because it could be used as a non-intrusive diagnosis for early detection, treatment evaluation of pathologies such glaucomatous damage and diabetic retinopathy. One of the main indispensable screening methods of glaucomatous damage is the assessment of the damaged optic nerve head. Optic nerve head assessment is considered to be more promising than the traditional assessment methods such as the intraocular pressure measurement and the visual field test [CLX+13]. The glaucomatous damage is mainly detected by identifying the changes in shape, colour or depth in the optic disc [LC03]. Thus the optic disc morphology is an important indicator for the presence of glaucoma and it evaluation can help minimise the risk of visual loss due to glaucomatous damage. The segmentation and localisation of the optic disc is also dispensable both in glaucoma assessment and the analysis of other retinal structures such as the blood vessels and the macula in computer-aided diagnosis. For example, the location of the optic disc relative to the macula was used by Tan et al. [TLW+10] to classify left and right eye retinal images. In addition to the physiological information of the optic disc, an automated detection of the optic disc location and size is an important factor in quantifying vascular changes in diabetic retinopathy and analysing of the severity of myopia [WLT+10].

However eye care specialists perform the optic nerve head assessment using manually planimetry (annotations) consisting of manually labelling the optic nerve head. This form of manual assessment is time consuming, expensive and subjective. Therefore, reliable automated methods for optic nerve head examination, which preserves various shapes of the disc would be very valuable and attractive in computer-aided diagnosis.

Several approaches of automated optic disc segmentation have been presented in the literature. But one of the main problems for detecting the optic disc in fundus retinal images is the appearance of the retinal structures in the image. Figure 5.1(a) shows an healthy retina image where the optic disc region is located at the right side of the image as bright yellowish round area with well defined shape, colour and size. Fig-

ure 5.1(b) shows an abnormal retinal image, revealing distorted shape and size caused by swelling. The segmentation of such optic nerve would be very difficult and require the combination of several retinal features (shape, colour, size). Figure 5.1(c) shows an image of the retina affected by central vein and artery occlusion. The haemorrhages caused by this pathology has completely masked the optic nerve making the disc segmentation impossible. Figure 5.1(d) shows several lesions on the retina, which have similar brightness as the optic disc. In this case using the brightness as a sole feature for segmenting the disc can lead to enormous errors. These issues show the difficulty in optic nerve segmentation and the necessity of robust and reliable technique, which preserves various optic disc shapes in the presence of different retinal diseases.

5.2 Previous Works

The optic disc detection approaches can be divided into pixel classification based methods, deformable-based methods and template based methods [CLX+13].

5.2.1 Pixel classification based methods

Most of the pixel classification methods are machine-learning techniques, which include the feature extraction and classification. Many features of the optic disc such as intensity, texture, colour, location and gist can be extracted from the fundus retinal photographs for classification. Pixel feature classification operation uses these features to assign a class to a pixel in an image, which can be either optic disc pixel or background pixel. As a supervised method, the classification is based on the training operation, where the technique learns to correctly perform the pixels classification from known classifications. Amount the classification methods the following methods were successful in segmenting the optic disc in the fundus retinal photographs.

Cheng et al. [CLX+13] proposed superpixel classification based method capable of performing both the optic disc and optic cup segmentation. The algorithm applies

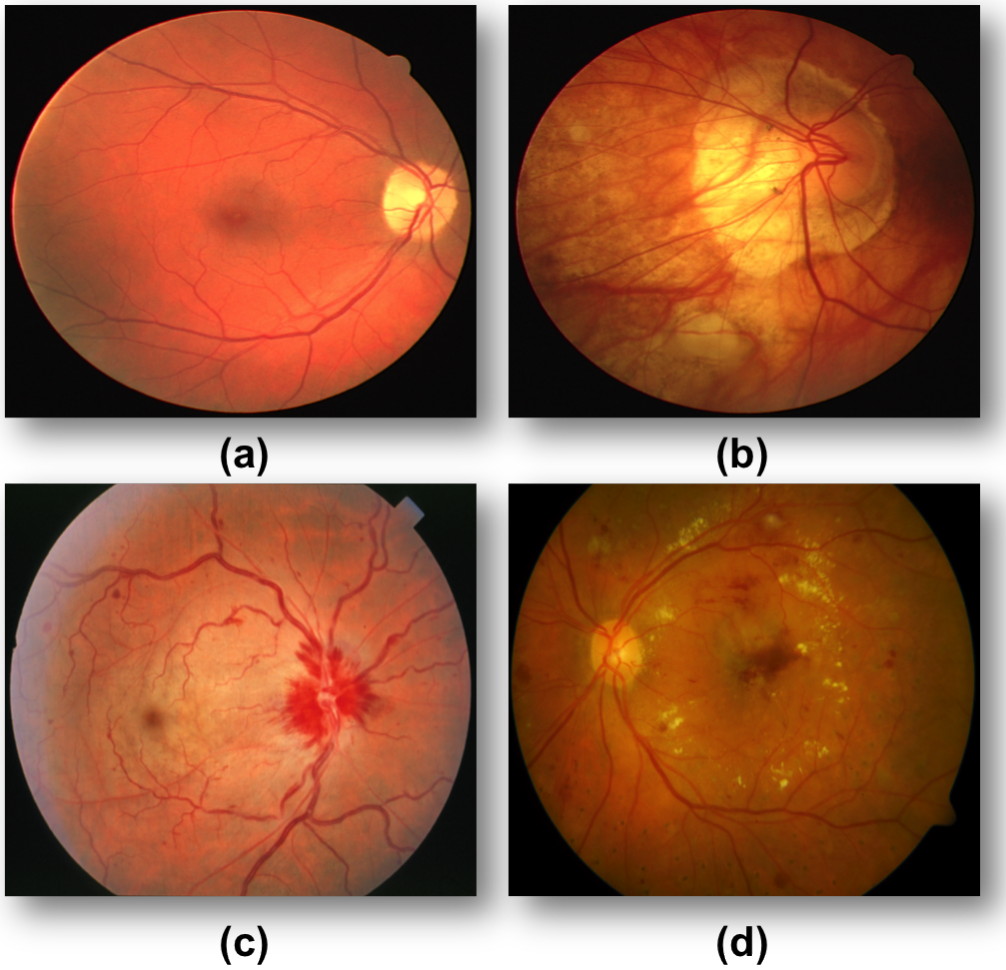

Figure 5.1: Retinal images. **(a)** Healthy retina with well defined optic nerve shape and size. **(b)** Optic nerve with distorted shape and size caused by swollen. **(c)** Optic nerve obscured by haemorrhages. **(d)** Optic nerve with lesions.

histogram equalisation to different channels (red, green and blue) of the RGB colour spaces to enhance the contrast of the images. The hue and saturation of HSV colour space are also used to forms five channel maps. These five channel maps are used to compute the histogram of each superpixel. Center surround statistics is used to classify each superpixel as disc pixel or background pixel. The location of the information was also used in the feature space to enhance the segmentation.

Wong et al. [WLT+10] presented an automated detection of the optic disc digital

retinal fundus images using machine learning technique. The method includes the region of interest detection, the feature extraction and the feature classification. By using the histogram of the retinal image and the intensity of the optic disc, a region of interest is defined to design more computationally efficient algorithms. The features are extracted based on the images colour space and the intensity. A support vector machine (SVM) is used to perform the classification of each feature pixel as disc or background pixels.

Abramoff et al. [AAG+07] proposed an automated segmentation method for cup to disc segmentation in stereo colour images. The algorithm performs the segmentation by first extracting the pixel features based on pixel intensity and simple edge operators. A Gaussian steerable filter bank is used on the image to create a large set of pixel features. This set is used to select an optimal combination of subset including twelve features. The classification is performed using the k-nearest neighbour (kNN).

5.2.2 Deformable-Based Method

The deformable-based method is an energy-based segmentation, which combine several features such as inherent connectivity and smoothness. These features allow noise filtering and solve boundary irregularities during segmentation [XPP00]. The deformable-based method can incorporate a priori knowledge about the location, shape and size of retinal image structures. The optic head nerve segmentation have deployed three deformable based methods including gradient-based active contour model, region-based active contour model and variational level-set based deformable model [JSK11].

In the gradient-based active contour model, the optic disc segmentation is performed first by initialising the disc contour manually or automatically. An energy term derived on the image gradient is used to perform the deformation in the contour. For example:

Mendels et al. [MHT99] presented a method based active contours for identifying the optic disc boundary in retinal images. A pre-processing based on morphological filtering and local minima detection is used to minimise the obstruction of the blood

vessels during the detection of the disc boundaries. The algorithm initialises the contour manually, which is then deformed by an external image derived field known as the Gradient Vector Flow.

Osareh et al. [OMTM02] proposed the optic disc location method in the retinal image using colour morphology and snakes. The first step of the algorithm was to remove the blood vessels in the optic disc region using colour morphology operation to offset their obstructions during the segmentation. Then, a snake was automatically initialised around the optic disc and allowed to evolve onto its boundary.

Both methods [MHT99] and [OMTM02] used pre-processing techniques to remove the blood vessels which causes significant degradation to the segmentation during the deformation in the contour under the effect of the energy term. But gradient-based active contour models segment the optic disc by restricting the segmentation results either to a circular or elliptical shaped object [JSK11]. Examples of this approach are presented in [LHS+04] and [NPS08].

The variational level-set deformable model was deployed to solve the local gradient minima problem in the gradient-based active contour model. In this model, the segmentation is performed by either incorporating the shape model into the energy formulation or as a post-processing step.

Wong et al. [WLL+08] proposed a variational level-set based automated cup-to-disc ratio measurement in the retinal images. The algorithm performs the segmentation of the optic disc and the cup by first estimating the initial contour using threshold analysis as a pre-processing step. After the segmentation of the disc an ellipse-fitting post-processing is used to correct the segmentation errors caused by the presence of the blood vessels in the disc region.

Li et al. [LC03] presented a method based on the extraction of the features in the retinal images including the optic disc and fovea and the pathology (exudates). A principal component analysis (PCA) is used to localise the optic disc. Then the boundary of the optic disc is detected by applying a modified active shape model.

One of the main problems of variational level-set deformable model is the limitation of the segmentation range of the optic disc due to the prior shape incorporation in the energy formulation. This can constraint the segmentation of irregular optic disc shapes [JSK11]. The method proposed in [XCS+07] overcomes this limitation using a model free snake technique. This technique a supervised classification to classify contour points into two set of groups either points belonging to vessel region or points belonging to the optic disc edge. In addition, the algorithm performs the deformation of each point using both local and global pixel information to address local gradient variations.

The region-based approaches have been deployed to overcome some of the issues in the gradient-based active contour model and the variational level-set deformable model. This approach is based on Mumford-Shah model [MS89], the optic disc region and the background are statically modelled and the energy functional is minimised to get the best segmentation results of the optic disc. The algorithm used in this approach is more robust against local gradient variation, it allows better segmentation of irregular disc shapes. Examples of this approach are listed in the following:

Joshi et al. [JSKK10] proposed a approach to detect the optic disc and the cup in the retinal image using the image regional information. The segmentation is performed using the shape deformation model by incorporating the relevant disc parameters using the optic disc and the cup boundaries. A deformable model guided by an energy term defined by regional statistics is used to detect the optic disc boundary.

Tang et al. [TLvFG06] proposed an effective approach for automated segmentation of the papilla in fundus retinal image. The algorithm incorporates the Chan-Vese (C-V) model using level sets and the elliptical shape constraint, which force the deformation in the contour to stay ellipse. This allows an accurate extraction of the papilla from the retinal image.

Deformable-based methods are very attractive in optic disc and cup detection as they can achieve a high performance when the boundaries and the shapes of the optic

disc are well defined in the retinal images. However, with local gradient variations (high gradient at vessel locations), the gradient-based active contour model may lead to a wrong segmentation of the disc boundary [MHT99], [OMTM02]. To address the local gradient variations some techniques constrain the segmentation results to a shape model (circular or elliptical) either by incorporating them into the energy formulation or using them in the post-processing steps of the segmentation. This can limited the segmentation of irregular optic disc shapes as seen in both variational level-set based deformable and region-based models [JSK11], [LC03], [JSKK10]. Furthermore, the deformable-based methods such as the region-based approaches [JSKK10] also suffer when the object to be segmented cannot be easily modelled in terms of global statistics [JSK11].

5.2.3 Shape-Based Template Matching Methods

The optic disc segmentation approaches that use the shape-based template matching methods perform the segmentation by modelling the optic disc as either an elliptical or a circular object. The matching operation is applied on a given retinal images edge map. Among these approaches, we have:

Aquino et al. [AGAM10] performed the detection of the optic disc boundary in digital fundus retinal photographs by morphological, edge detection operations and feature extraction model. The morphological operation is used to eliminate the vessels in the optic disc region followed by the edge detection operation and the circular Hough transform to define a circular optic disc boundary. A location approach based on a voting is also used to define the optic disc pixels.

Cheng et al. [CLW+11] proposed an automated optic disc segmentation in digital fundus retinal images. The algorithm starts the disc segmentation by eliminating the peripapillary atropy (PPA) through edge filtering so that all the non-disc structures are eliminated from the image to make the segmentation more accurate. The segmentation is performed by constraining the optic disc boundary to an elliptical shape using Hough

transform.

Lalonde et al.[LBG01] presented a template based optic disc detection method in low resolution colour fundus digital retinal images. The disc segmentation is detected by performing two operations. The first operation uses a Hausdorff based template matching on edge map. This operation is guided by a second operation, which uses a pyramidal decomposition for large-scale pixel tracking.

The shape-based template matching methods take advantage of the prior knowledge of the retina structures in the fundus retinal photographs by modelling them in template-based methodology. Consequently these approaches achieve high performance in a given retinal images data set. However the shape-based template matching methods may lead to erroneous segmentations on new retinal image data set. These approaches also suffer from the presence of the blood vessels into the optic disc region, which misguides the segmentation algorithm. In addition, the shape based modelling of the optic disc boundary puts restrictions for the detection of irregular optic disc shapes due the pathological changes.

In contrast to previous methods, we proposed two different methods, which find the convergence of the blood vessel network to define the location of the optic disc. Both methods use a prior segmented blood vessel network to perform the segmentation of the optic disc. The evaluations show that our methods achieve successful segmentation of the optic disc on 129 fundus images including 98 images with variety of lesions.

5.3 Methods

The optic disc segmentation starts by defining the location of the optic disc. This process used the convergence feature of vessels into the optic disc to estimate its location. The disc area is then segmented using two different automated methods (Markov Random field image reconstruction and Compensation Factor). Both methods use the convergence feature of the vessels to identify the position of the disc. The Markov

Random Field (MRF) method is applied to eliminate the vessel from the optic disc region. This process is known as image reconstruction and it is performed only on the vessel pixels to avoid the modification of other structures of the image. The reconstructed image is free of vessel and it is used to segment the optic disc via graph cut. In contrast to MRF method, the Compensation Factor approach segments the optic disc using prior local intensity knowledge of the vessels. Figure 5.2 shows the overview of both the MRF and the Compensation Factor method process.

5.3.1 Optic Disc Location

Inspired by the method proposed in [WSK+10], which effectively locates the optic disc using the vessels. We use the binary image of vessels segmented in Section 4.2 to find the location of the optic disc. The process iteratively traces towards the centroid of the optic disc. The vessel image is pruned using a morphological open process to eliminate thin vessels and keep the main arcade. The centroid of the arcade is calculated using the following formulation:

$$C_x = \sum_{i=1}^{K} \frac{x_i}{K} \qquad C_y = \sum_{i=1}^{K} \frac{y_i}{K} \tag{5.1}$$

where x_i and y_i are the coordinates of the pixel in the binary image and K is the number of pixels set to 1 (pixels marked as blood vessels) in the binary image.

Given the gray scale intensity of a retinal image, we select 1% of the brightest region. The algorithm detects the brightest region with the most number of pixels to determine the location of the optic disc with respect to the centroid point (right, left, up or down). The algorithm adjusts the centroid point iteratively until it reaches the vessel convergence point or centre of the main arcade (centre of the optic disc) by reducing the distance from one centroid point to next one in the direction of the brightest region, and correcting the central position inside the arcade accordingly. Figure 5.3 shows the process of estimating the location of the of optic disc in a retinal image. It is important

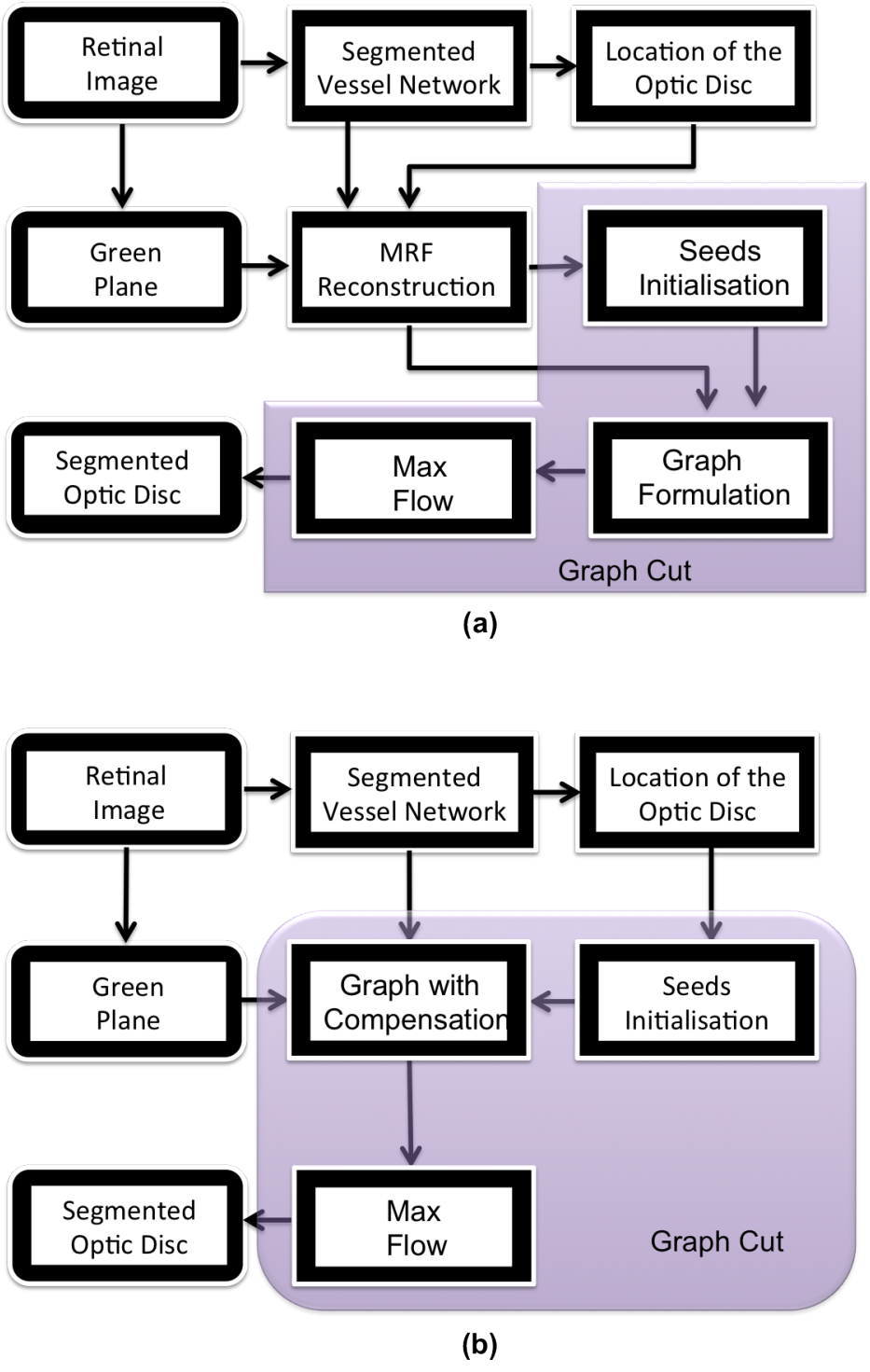

Figure 5.2: **(a)** Markov Random Field Image Reconstruction method diagram. **(b)** Compensation Factor method diagram.

to notice that, the vessel convergence point must be detected accurately, since this point is used to automatically mark foreground seeds. A point on the border of the optic disc may result in some false foreground seeds. After the detection of the vessel convergence point, the image is constrained a region of interest (ROI) including the whole area of the optic disc to minimize the processing time. This ROI is set to a square of 200 by 200 pixels concentric with the detected optic disc centre. Then an automatic initialisation of seeds (foreground and background) for the graph is performed. A neighbourhood of 20 pixels of radius around the centre of the optic disc area is marked as foreground pixels and a band of pixels around the perimeter of the image are selected as background seeds as shown in Figure 5.4.

5.3.2 Optic Disc Segmentation with Markov Random Field Image Reconstruction

The high contrast of blood vessels inside the optic disc presented the main difficulty for it segmentation as it misguides the segmentation through a short path, breaking the continuity of the optic disc boundary. To address this problem, the MRF based reconstruction method presented in [EL99] is adapted in our work. We have selected this approach because of its robustness. The objective of our algorithm is to find a best match for some missing pixels in the image, however one of the weaknesses of MRF based reconstruction is the requirement for intensive computation. To overcome this problem, we have limited the reconstruction to the ROI and using prior segmented retina vascular tree, the reconstruction was performed in the ROI. An overview diagram of the optic disc segmentation with Markov random field image reconstruction is shown in Figure 5.2(a).

Let us consider a pixel neighbourhood $w(p)$ defined as a square window of size W, where pixel p is the centre of the neighbourhood . I is the image to be reconstructed and some of the pixels in I are missing. Our objective is to find the best approximate values for the missing pixels in I. So let $d(w1, w2)$ represent a perceptual distance between

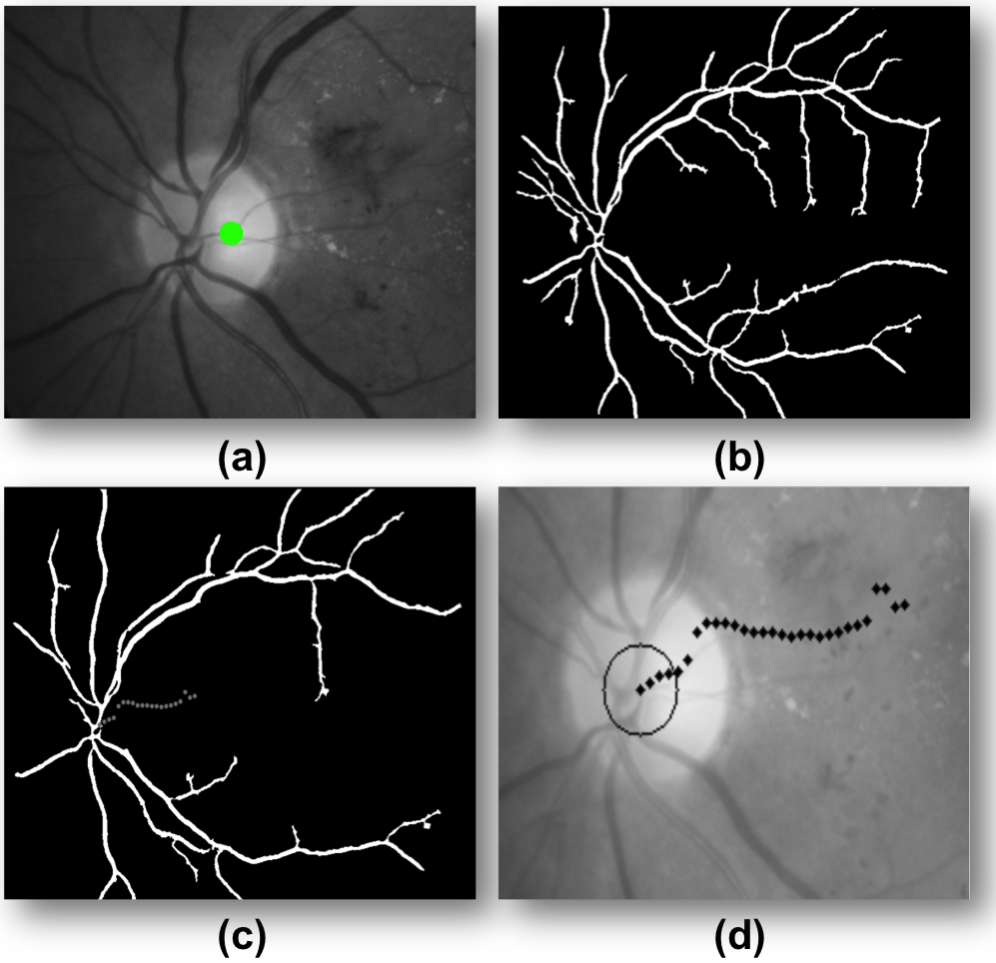

Figure 5.3: Optic disc detection. **(a)** Retinal image green channel with 1% of the brightest region selected in green colour. **(b)** Binary segmented blood vessel. **(c)** Binary segmented blood vessel after pruning. **(d)** Sequence of points from the centroid to vessels convergence point (optic disc location).

two patches that defines their similarity. The exact matching patch corresponds to $d(w', w(p)) = 0$. If we define a set of these patches as $\Omega(p) = \{\omega' \subset I : d(\omega', \omega(p)) = 0\}$ the probability density function of p can be estimated with a histogram of all centre pixel values in $\Omega(p)$. However we are considering a finite neighbourhood for p and the search is limited to the image area, there might not be any exact matches for a patch. For this reason, we find a collection of patches, which match falls between the best match and a threshold. The closest match is calculated as $\omega_{\text{best}} = \text{argmin}_{\omega} d(\omega(p), \omega) \subset$

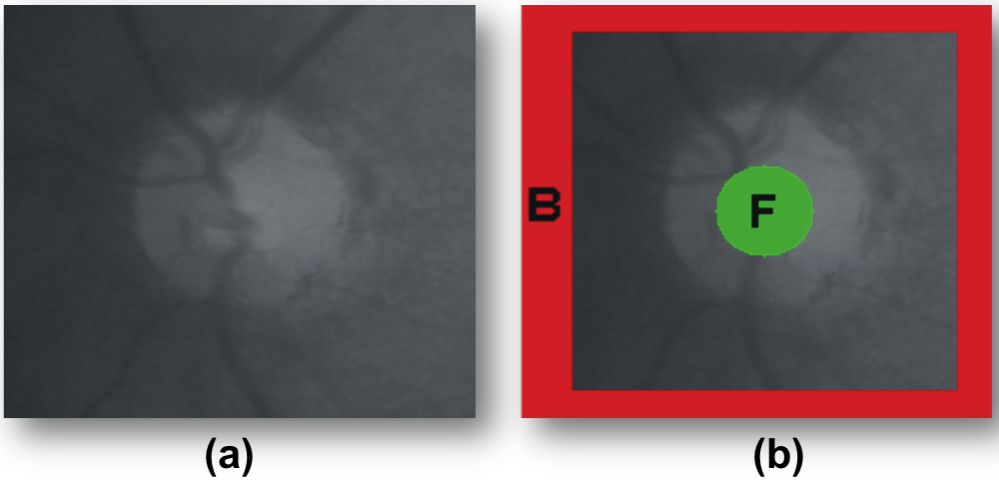

Figure 5.4: Optic disc detection. **(a)** ROI image **(b)** initialisation of the foreground **F** and the background **B** of the ROI image.

I. All the patches ω with $d(\omega(p), \omega) < (1+\epsilon)d(\omega(p), \omega_{\text{best}})$ are included in the collection ω'. $d(w', w(p))$ is defined as the sum of the absolute differences of the intensities between patches, so identical patches will result in $d(w', w(p)) = 0$. Using the collection of patches, we create an histogram and select the one with the highest mode. Figure 5.5 shows sample results of the reconstruction. The foreground Fg_s and the background Bg_s seeds are initialised in the reconstructed image, which are then used in graph cut formulation to segment the optic disc. Similar to Figure 5.4, the initialisation of the foreground Fg_s and background Bg_s seeds is performed using the reconstructed image.

The graph cut algorithm introduced in Section 4.2.2 is used to separate the foreground and the background by minimising the energy function over the graph and producing the optimal segmentation of the optic disc in the image. The energy function of the graph in (4.4) consists of regional and boundary terms. The regional term (likelihoods of foreground and background) is calculated using (4.5), while the boundary term (relationship between neighbouring pixels) is derived using (4.6). A grid of 16 neighbours N is selected to create links between pixels in the image Im. The Max-Flow algorithm is used to cut the graph and find the optimal segmentation.

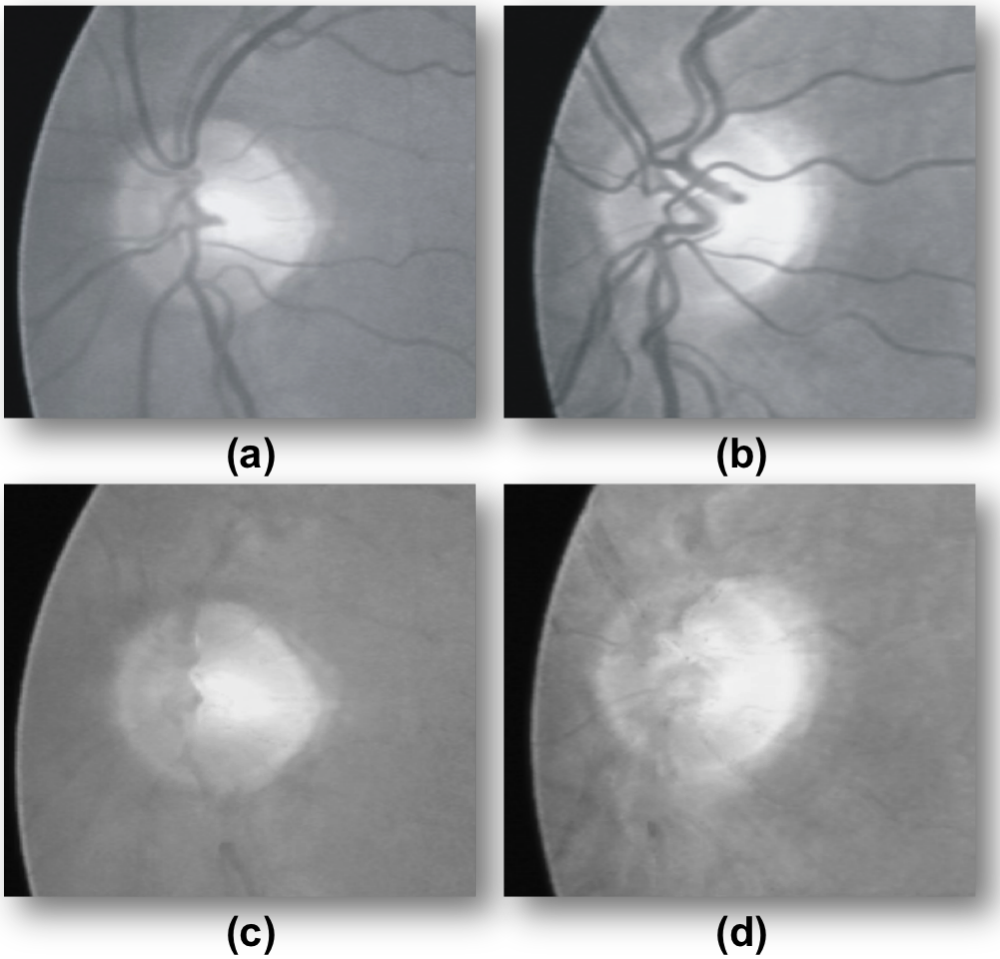

Figure 5.5: MRF reconstruction applied to retinal images. (Top) **(a)** and **(b)** original gray scale images. (Bottom) **(c)** and **(d)** reconstructed images using the MRF based method.

5.3.3 Optic Disc Segmentation With Compensation Factor

In contrast to MRF image reconstruction, we incorporate the blood vessels into the graph cut formulation by introducing a compensation factor (Vad). This factor is derived using prior information of blood vessel. The algorithm diagram of the optic disc segmentation with Compensation factor is shown in Figure 5.2(b).

The energy function of the graph cut algorithm generally comprises a boundary and regional terms. The boundary term defined in (4.6) is used to assign weights on the

edges between the neighbouring pixels (n-links) by measuring the similarity between neighbouring pixels with respect to the pixel proprieties (intensity, texture, colour). Therefore pixels with similar intensities have a strong connection. The regional term in (4.5) is derived to define the likelihood of the pixel belonging to the background or to the foreground by assigning weights on the edges (t-link) between image pixels and the two terminals background and foreground seeds. In order to incorporate the blood vessels into the graph cut formulation, we derived the t-link as follows:

$$\mathrm{S_{link}} = -\ln P_r\left(I_p \backslash \mathrm{Fg_{seeds}}\right) \tag{5.2}$$

$$\mathrm{T_{link}} = -\ln P_r\left(I_p \backslash \mathrm{Bg_{seeds}}\right) \tag{5.3}$$

$$\text{For } p \neq \text{vessel}$$

$$\mathrm{S_{link}} = -\ln P_r\left(I_p \backslash \mathrm{Fg_{seeds}}\right) + \mathrm{Vad} \tag{5.4}$$

$$\mathrm{T_{link}} = -\ln P_r\left(I_p \backslash \mathrm{Bg_{seeds}}\right) \tag{5.5}$$

$$\text{For } p = \text{vessel}$$

where p is the pixel in the image, Fg_{seeds} is the intensity distribution of the foreground seeds, Bg_{seeds} represents the intensity distribution of the background seeds and Vad is the compensation factor given as:

$$\mathrm{Vad} = \max_{p \in \mathrm{vessel}}\{-\ln P_r\left(I_p \backslash \mathrm{Fg_{seeds}}\right)\} \tag{5.6}$$

The intensity distribution of the blood vessel pixels in the region around the optic disc makes them more likely to belong to background pixels than the foreground (or the optic disc pixels). Therefore the vessels inside the disc have weak connections with neighbouring pixels making them likely to be segmented by the graph cut as back-

ground. We introduce in (5.4) a compensation vector to all s-links of the foreground for pixels belong to the vascular tree to address this behaviour. Consequently, vessels inside the optic disc are classified with respect to their neighbourhood connections instead of their likelihood with the terminals foreground and background seeds. Figure 5.6 shows sample of images segmented by Compensation Factor. The segmentation of the disc is affected by the value of Vad, the method achieves poor segmentation results for low value of Vad. However when the value of the Vad increases, the performance improves until the value of Vad is high enough to segment the rest of the vessels as foreground.

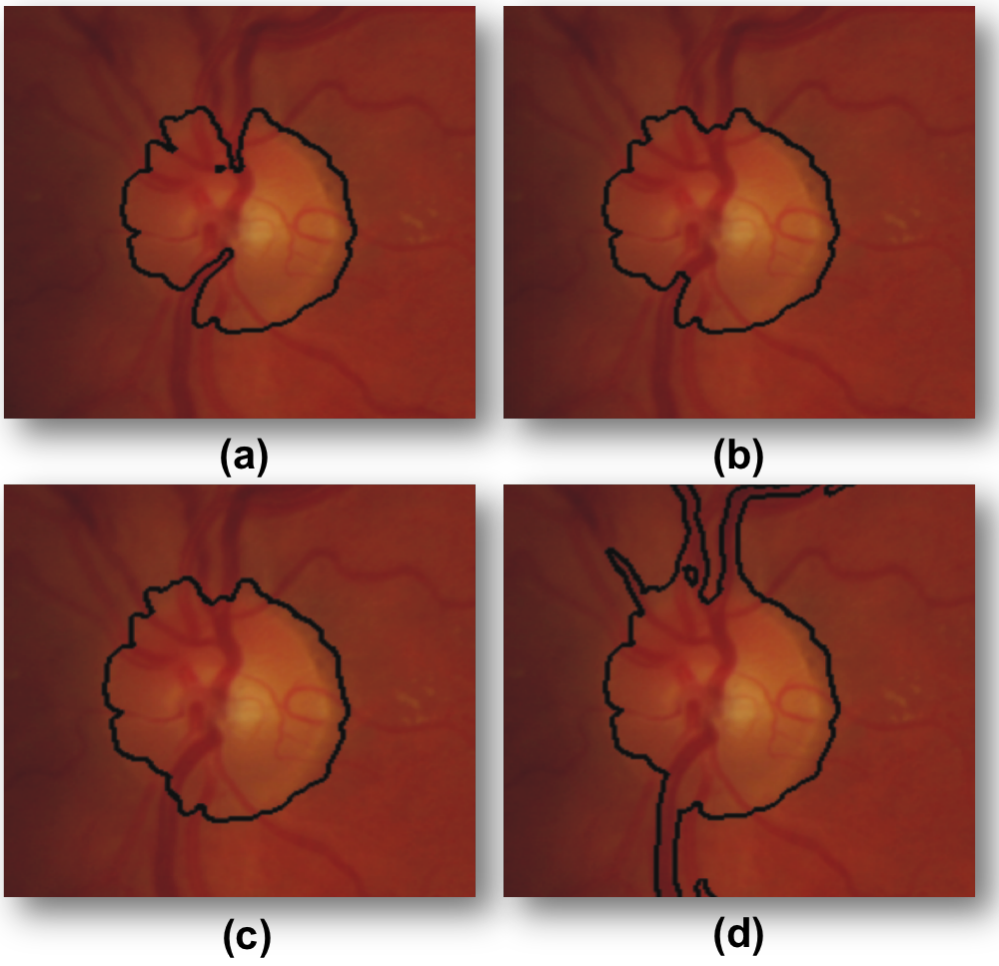

Figure 5.6: Optic disc segmentation with Compensation Factor method: **(a)** $Vad = 20$. **(b)** $Vad = 100$. **(c)** $Vad = 150$. **(d)** $Vad = 250$.

5.4 Experiments

The proposed optic disc segmentation method was tested on two public datasets, DRIVE [SAN+04b] and DIARETDB1 [KKK+07], consisting of 129 images in total inclunding 99 images with a variety of lesions. The performance of the method is tested against a number of alternative methods.

The DRIVE consists of 40 digital images including 15 images containing a variety of lesions. The images were captured from a Canon CR5 non-mydriatic 3CCD camera at 45° field of view (FOV). The images have a size of 768 × 584 pixels. The dataset includes masks to separate the FOV from the rest of the image. It included two sets of hand labelled images (set A and set B) for the blood vessel. The set A offers the manually labelled images for all the images in the dataset, whereas the set B provides the manually labelled images for half of the dataset. To test our method we adopt the set A hand labelling as the benchmark. We manually delimited the optic disc to test the performance of optic disc segmentation algorithm.

The DIARETDB1 dataset consist of 89 colour images with 84 of them contain at last one indication of lesions. The images were captured with digital fundus camera at 50 degree filed of view and have a size of 1500 × 1152 pixels. Hand labelled lesion regions are provided in this dataset by four human experts. However the DIARETDB1 dataset only includes the hand labelled ground truth of lesions but not the blood vessels and the optic disc. For this reason, we were unable to compare the performance of the blood vessel segmentation on the DIARETDB1 dataset. Nevertheless we were able to create the hand labelled ground truth of optic disc to test the performance of the optic disc segmentation.

The performance results of our approach are compared to the alternative methods: The adaptive morphological approach by Welfer et al. [WSK+10], the traditional graph cut technique by Boykov et al. [BFL06] and the topology cut technique proposed by Zeng et al. [ZSCP08]. Unfortunately it was not possible to test our method against a

large number of alternative methods, since most of the methods do use a unique benchmark to measure the results of the optic disc segmentation, therefore this makes the comparison of the results difficult. Further comparison is made between our two optic disc segmentation methods (the Compensation factor and the Markov Random field image reconstruction). All the methods are tested on the same datasets (DIARETDB1 and DRIVE) of 109 fundus retinal images in total, including those with discernable optic disc.

The optic disc segmentation performance is evaluated by the overlapping ratio Oratio and the mean absolute distance MAD. The overlapping ratio is defined to measure the common area between the optic disc region in the ground truth and the optic disc region segmented by our method. It is defined by the following formulation:

$$\text{Oratio} = \frac{\text{G}\bigcap\text{S}}{\text{G}\bigcup\text{S}} \tag{5.7}$$

where G represents the true optic disc boundary (manually labelled region) and S is the optic disc boundary segmented by our method. MAD is defined as:

$$\text{MAD}\left(\text{G}_c, \text{S}_c\right) = \frac{1}{2}\left\{\frac{1}{n}\sum_{i=1}^{n} d(g_{ci}, \text{S}) + \frac{1}{m}\sum_{i=1}^{m} d(s_{ci}, \text{G})\right\} \tag{5.8}$$

where G_c and S_c are the contours of the segmented regions of the ground truth and our algorithm respectively. $d(a_i, B)$ is the minimum distance from the position of the pixel a_i on the contour A to the contour B. A good segmentation implies a high overlapping ratio and a low MAD value.

The sensitivity of our method on DIARETDB1 and DRIVE, it is defined as:

$$\text{Sensitivity} = \frac{\text{Tp}}{\text{Tp} + \text{Fn}} \tag{5.9}$$

where Tp and Fn are the number of true positives and the number of false negatives respectively. The sensitivity indicates the detection of the foreground pixels by the

segmentation method.

Figure 5.7 (a) and (b) show the optic disc segmentation results of topology cut technique [ZSCP08], traditional graph cut technique [BFL06] and both our methods the optic disc segmentation with compensation factor and the optic disc segmentation with Markov Random field image reconstruction on DIARETDB1 and DRIVE respectively. Considering the ground truth images, It is clear that both our methods perform better than alternative methods topology cut technique [ZSCP08] and traditional graph cut technique [BFL06]. The topology cut technique achieved acceptable results in the brighter images, characterised by vessels that are more likely to belong to the foreground (similar intensity as the optic disc). However, the traditional graph cut technique tends to segment only the brightest region of the disc, this is due to the intrusion of the blood vessels in the optic disc region, which misguide the segmentation algorithm to follow a short path.

Table 5.1 shows the performance of our proposed methods with alternative methods on DIARETDB1 images. The compensation factor and the MRF image reconstruction segmentation algorithms achieve the overlapping ratio of 0.7594 and 0.7850 and outperform the approaches in [WSK+10], [ZSCP08] and [BFL06]. However considering the performance in terms of a mean absolute distance, the MRF image reconstruction algorithm reaches the lowest value 6.55 and performs better than all the other methods. Both our methods achieve the highest average sensitivity with 87.50% for MRF image reconstruction and 86.75% for compensation factor on the DIARETDB1 images.

Table 5.2 shows the performance results of our methods with other alternative methods in terms of Oratio, MAD and *Sensitivity* on DRIVE images. An overview of the segmentation results shows our proposed methods achieved the highest overlapping ratio with the minimum MAD value compare to the traditional graph cut method [BFL06], the topology cut method [ZSCP08], except the Adaptive morphologic [WSK+10], which is marginally inferior to the compensation factor algorithm in terms of MAD. However, an increase in the overlapping ratio does not necessarily mean

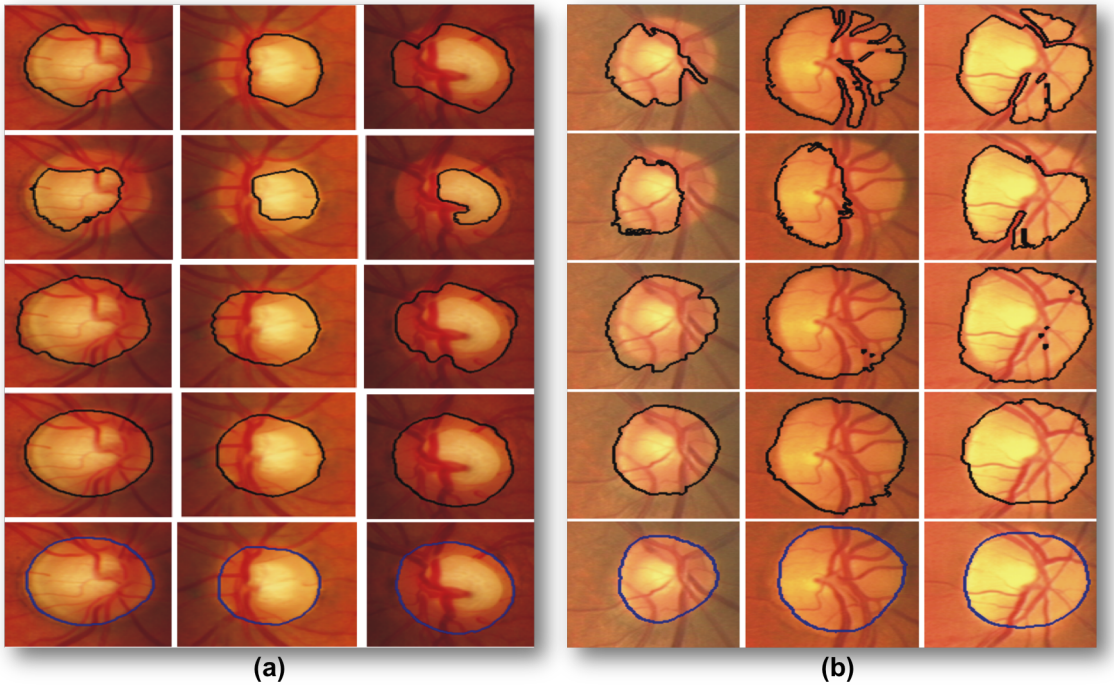

Figure 5.7: **(a)** Optic disc segmentation results of DIARETDB1 images: First row Topology cut, second row Graph cut, third row Compensation factor algorithm, fourth row Markov Random field image reconstruction algorithm, fifth row Hand labelled. **(b)** Optic disc segmentation results of DRIVE images: First row Topology cut, second row Graph cut, third row Compensation factor algorithm, fourth row Markov Random field image reconstruction algorithm, fifth row Hand labelled.

a decrease on MAD value. Thus the value of MAD alone is not enough to measure the performance of segmentation results, but it provides a good reference of the contour matching with the ground truth contour reference.

Method	**Average ORatio**	**Average MAD**	**Average Sensitivity**
Topology cut [ZSCP08]	0.3843	17.49	0.5530
Adaptive morphologic [WSK+10]	0.4365	8.31	—
Graph cut [BFL06]	0.5403	10.74	0.7635
Compensation Factor	0.7594	6.18	0.8675
MRF Image Reconstruction	0.7850	6.55	0.8750

Table 5.1: **Performance comparison** - DIARETDB1 dataset

For further performance comparison, we use the cumulative histogram to compare

Method	Average Oratio	Average MAD	Average Sensitivity
Topology Cut [ZSCP08]	0.5591	10.24	0.6512
Adaptive morphologic [WSK+10]	0.4147	5.74	—
Graph cut [BFL06]	0.5532	9.97	0.7398
Compensation Factor	0.709	6.48	0.8464
MRF Image Reconstruction	0.8240	3.39	0.9819

Table 5.2: **Performance comparison** - DRIVE dataset

the overlapping ratio of our proposed method against Topology Cut [ZSCP08] and Graph cut [BFL06]. This is done by performing each segmentation method against the human expert hand labelled image, and the cumulative histogram represents the frequency of the Oratio value. A perfect segmentation is achieved when the value of Oratio = 1 and the area under the curve is equal to zero. Figure 5.8 shows the plotted of the cumulative histograms comparison of overlapping ratio for Topology Cut [ZSCP08] and Graph cut [BFL06], Compensation Factor and MRF image reconstruction on DIARETDB1 and DRIVE datasets respectively. The overview of the graphs show that the Compensation Factor and MRF image reconstruction methods achieve the minimum area under the graph, hence our method outperforms all other methods. In general the MRF image reconstruction method reaches better results on DRIVE images, while the Compensation Factor method produces better segmentation results on DIARETDB1 dataset.

Based on the assumption in Niemeijer et al. [NAVG07] which consider a minimum overlapping ratio Oratio $> 50\%$ as a successful segmentation, the compensation factor algorithm with 86.52% success performs better on DRIVE than DIARETDB1 and the segmentation of MRF image reconstruction with 90.00% achieves better results than the compensation factor algorithm on DRIVE .

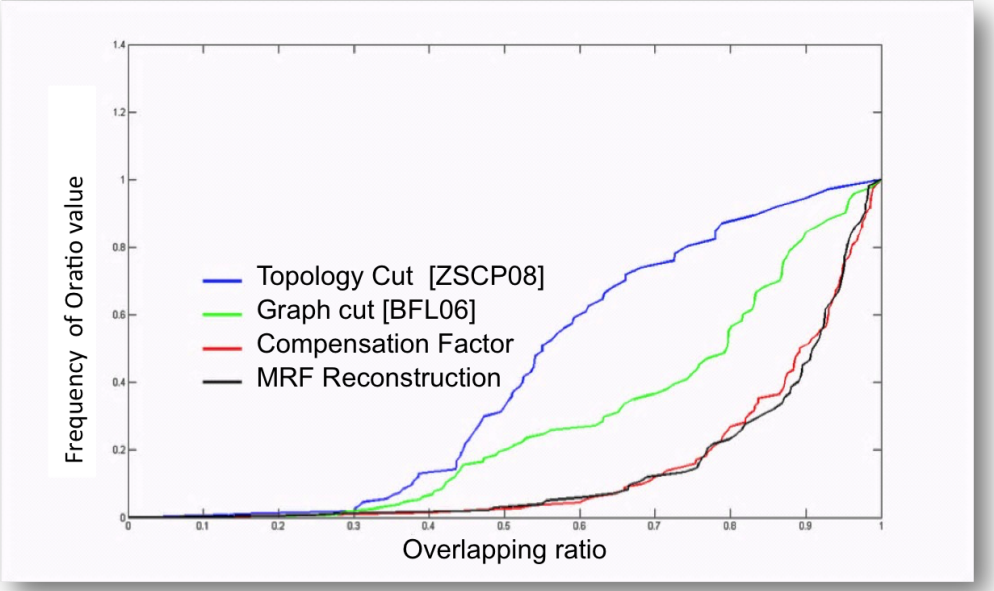

Figure 5.8: Cumulative histogram comparison for overlapping ratio of **(a)** DIARETDB1 and **(b)** DRIVE images.

5.5 Summary

We have presented novel approaches to automated segmentation of optic disc in fundus retinal images. The proposed methods use the convergence feature of the blood vessel network into the optic disc region and the feature of disc brightness to locate the position of the optic disc in the image. The segmented blood vessel network is also used to perform the MRF image reconstruction and the compensation factor into the graph cut method.

We have evaluated the performance the proposed methods on 129 fundus retinal images including 99 images showing a variety of lesions. The methods were also compared against three other methods in the literature on the same datasets.

On this difficult datasets, the results of the segmentation show that the proposed methods successfully segmented the optic disc. With an average sensitivity of 86.75% and 84.64% for the Compensation factor method and 87.50% and 98.19% for MRF image reconstruction on DIARETDB1 and DRIVE respectively, our methods achieved the best overall performance.

The results also show that, the MRF image reconstruction algorithm outperforms the Compensation factor algorithm by 2.56% and 11.5% on DIARETDB1 and DRIVE images respectively. However it is important to note that, both the MRF image reconstruction and compensation factor algorithms depend on the vessel segmentation algorithm, for example if the vessel segmentation algorithm achieved a low performance on severely damaged retinal images, the reconstruction would not defined a meaningful optic disc region, leading to segmentation errors. However the performance comparison in Table 5.1 and 5.2 show that the MRF image reconstruction method outperforms in segmenting the optic disc region on DIARETDB1 dataset in term of averages Oratio, MAD and Sensitivity. While the compensation factor method achieved better segmentation results on DRIVE dataset in term of the same metrics.

Furthermore, the proposed methods address one of the main issues in medical im-

age analysis, the overlapping tissue segmentation. Since the blood vessels converse into the optic disc area and misguide the graph cut algorithm through a short path, breaking the optic disc boundary. To achieve a good segmentation results, the MRF image reconstruction algorithm eliminates vessels in the optic disc area without any modification of the image structures before segmenting the optic disc. On the other hand the compensation factor incorporates vessels using local intensity characteristic to perform the optic disc segmentation. We believe that our optic disc methods can be also useful in other applications of the overlapping tissue segmentation.

Chapter 6

Retina Layer Segmentation Using Kernel Graph Cuts

This is our fourth contribution.

6.1 Introduction

Optical coherence tomography (OCT) imaging has been largely used in ophthalmology as a tool for assessing and monitoring morphological features such as the thickness of the retinal layers [HSL+91]. The time-domain OCT is one of the first OCT imaging techniques in retinal diseases diagnosis [SHA+95], [GSH+03]. However this technique has its limitations. The time domain OCT can only provide the RNFL thickness measurements in a line scan.

To address these limitations, the Spectral-Domain Optic Coherence Tomography SD-OCT [FHKEZ95, WLK+02] was developed with faster scan capability that provides the most comprehensive structure of the retina. With these new capabilities, this imaging equipment possesses a powerful tool that allows a 3-D image of the retina to be formed in routine clinical scans. The SD-OCT generates an image by an in-depth axial scan known as an A-scan. A series of successive A-scans form a cross sectional 2-D

image known as a B-scan. Using a series of successive B-scans, a 3-D image volume of the retina is yielded. This new technique is used in modern ophthalmology to assist the diagnosis of retinal diseases such as glaucoma, diabetic retinopathy, neo-vascularisation, vein occlusion and many more vision impairment diseases.

The evaluation of the RNFL thickness in glaucomatous damage requires segmentation of different retinal layers. This process can be time consuming and tedious when it is done by hand. Therefore there is a need for a robust and reliable automated segmentation algorithm in computer-aided diagnosis, which preserves various retinal layer shapes.

Circular scan SD-OCT imaging has become one of the best tools for diagnosis of retinal diseases. This technique provides a more comprehensive detail of the retinal morphology and layers around the optic disc nerve head (ONH). However accurate automated segmentation methods are needed to provide the thickness evaluation of these layers, since manually labelling these retinal layers can be tedious and time consuming.

This chapter presents an automated method that serves this purpose by performing the segmentation of retinal layers boundaries in a circular scan SD-OCT image acquired around the ONH. The layers are detected by adapting a graph cut segmentation technique that includes a kernel-induced space and a continuous multiplier based max-flow algorithm. Results from scan images acquired with Spectralis HRA+OCT (Heidelberg Engineering, Germany) prove that the proposed method is robust and efficient in detecting the retinal layer boundaries in images. With a mean absolute deviation (MAD) of 0.3589 ± 0.2624 and an average Dice coefficient of 0.9488 ± 0.0404 pixels for the retinal nerve fiber layer thickness (RNFLT), the proposed method demonstrated effective agreement with manual annotations.

6.2 Previous Studies

Recently many methods for retinal layers segmentation in the OCT image have been extensively studied. Early methods were purely based on pixel intensity variation (high and low tissue reflectivity) processing operations along A-scan profile [KBR01], [ISW+05], [CFSP05], [ASG+08]. These methods detected the retinal layer boundary by setting a target threshold value for the layer tissue pixel intensity. They are computationally efficient, but often suffer because of the variation of intensity within layers. This inconsistency of intensity is commonly generated by the blood vessels artefacts (shadows) during the OCT imaging. Some other segmentation techniques use image gradients, prior layer shape information and many other constraints to perform the segmentation of the layers. Some of these segmentation technique are active contours, graph cut and machine learning approaches. The active contours segmentation technique uses an energy formulation consisting of gradient, edge density and boundary smoothness. In [MCC+05], Mujat et al performed the segmentation of the RNFL thickness in SD-OCT image using anisotropic noise suppression operation and deformable splines. This technique is not affected by any intensity variation but it is sensitive to the artefacts of the blood vessels in the OCT image. Yazdanpanah et al [YHSS11], used Chan-Veses energy-minimising active contours to segment the intra-retinal layers by incorporating a circular shape in order to model the boundaries of retinal layers. This method is also less affected by the intensity variations, however the constraints on the boundaries can lead to errors when segmenting irregular layer shapes. In [NVT+13], Novosel et al utilised Bayesian inference in level sets to segment three retinal layers in SD-OCT retinal image. All the layers are simultaneously detected using prior knowledge of the layers. This segmentation approach is also sensitive to the blood vessel artefacts. Zhu et al [ZCS+10] provided a FloatingCanvas technique for retinal layer segmentation in 3-D SD-OCT. The algorithm makes use of analytical surface deformable and prior information about the layers location in the OCT image.

This method is sensitive to low gradient on the region of the vitreous-RNFL boundary of some OCT images. Garvin et al [GAK+08] segmented five retinal layers in 3-D SD-OCT by finding a minimum-cost in a geometric graph formulated from edge information and priori surface information. This technique was improved in [GAW+09], which simultaneously segmented retinal layers by learning the cost function and constraints from a training set and by using a 3-D graph search technique. The graph search method was extended in [CLN+10] by Chiu et al, to segment eight retinal layer boundaries on individual B-scan in the SD-OCT using dynamic programming.

The majority of these methods [MCC+05], [YHSS11], [NVT+13], [ZCS+10], [GAW+09], [CLN+10] used prior knowledge about the layers to apply constraints such as shapes and positions on the segmentation algorithms. These constraints can lead to segmentation errors when the algorithms are used on irregular retinal layers or new OCT data sets. Also the graph-based segmentation methods have problems in finding appropriate cost functions on the graph formulation to distinguish individual layers. Another issues with the graph-based segmentation is the efficiency of the optimisation operations to accurately detect the layers boundaries. Furthermore, segmentation algorithms used in many commercially available OCT imaging tools encounter enormous problems segmenting the RNFL layers in OCT images with poor scanning quality or noise as seen in Figure 6.1 [Sco10].

The aim of this work is to develop a new automated segmentation method to address the limitations of the existing for the RNF detection. It also provides a good balance between efficiency and robustness. Our method addresses some these segmentation problems using the bias correction algorithm [TAC+10b] to eliminate the image artefacts and a graph cut based segmentation technique which incorporates the mechanism of the kernel induced function [SMA11] and a continuous Max-flow to allow better detection of retinal layers. The proposed method also addresses the layers detection problem in the presence noises reports in [Sco10].

Because of the above advantages, our method performs better than the previous

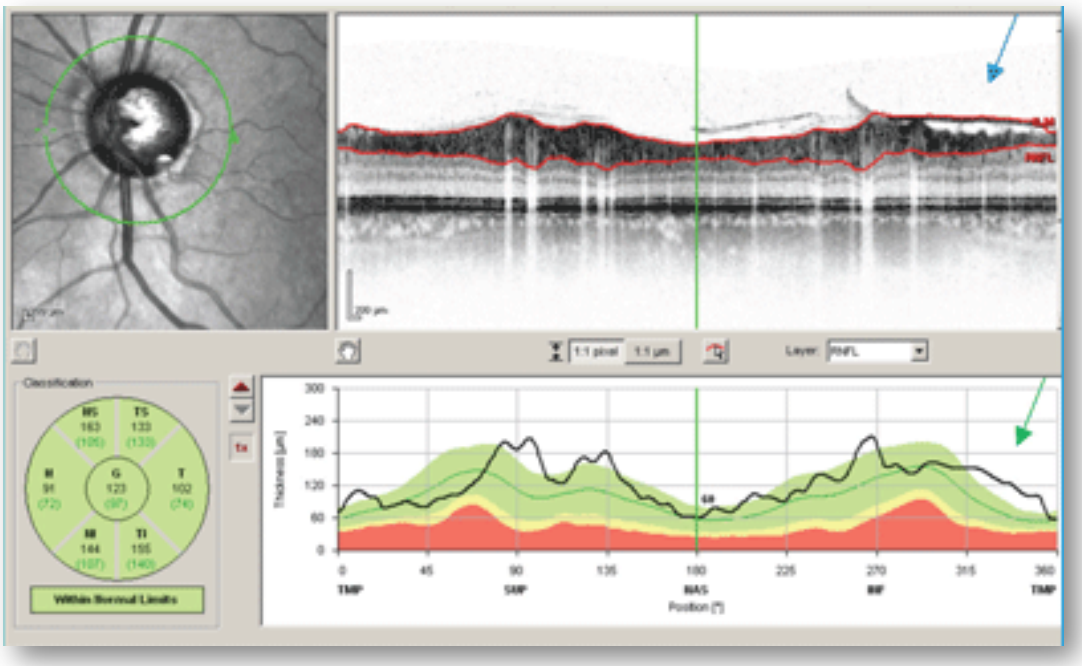

Figure 6.1: Error in measuring the RNFL thickness. Top left: circular scan. Top right: error in segmentation line at the inferior temporal quadrant indicated by the blue arrow caused by poor scan quality. Bottom right: the inferior temporal RNFL thickness is measured as abnormal shown by the green arrow. Bottom left: The classification chart showing the overall results of the RNFL thickness measurement within normal boundaries. [Sco10].

methods. In particular for difficult cases. We tested our method on 120 SD-OCT circular scans around the ONH. All the images were acquired with SD-OCT Spectralis HRA + OCT (Heidelberg Engineering, Germany). We believe our method would perform well on OCT images with diseases such as exudates, haemorrhage, swelling, edema, cyst, detachment, epimembrane, because the nature of the problems is similar, although we do not have access to these types of data currently. Figure 6.2 shows the different images of the retina in the circular scan.

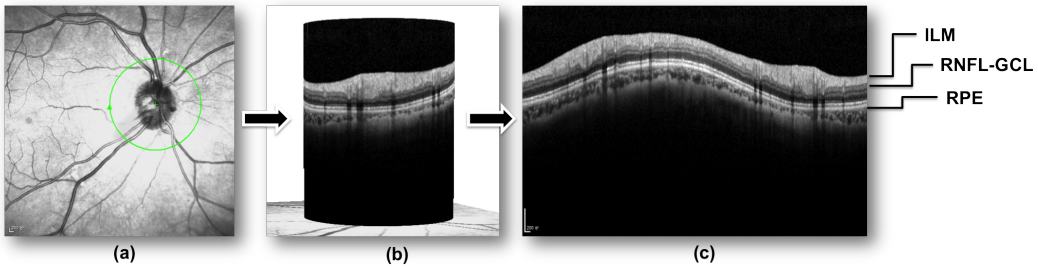

Figure 6.2: SD-OCT circular imaging process. **(a)** Circular scan on the OCT fundus image. **(b)** Reitnal tissues (Layers) image from the scan. **(c)** A 2-D OCT cross-sectional image of the layers tissues.

6.3 Methods

In this study, the segmentation of retinal layers boundaries including RNFL or inner limiting membrane (ILM), RNFL-ganglion cell layer (RNFL-GCL) and the retinal pigment epithelium (RPE) was performed. The segmentation method starts by removing some common medical imaging artefacts from the retinal SD-OTC circular images such as intensity inhomogeneity and noise. This operation is performed using the bias correction technique [TAC+10b] and it is expected to improve the robustness of the retinal tissue layers segmentation. The boundaries of the ILM, RNFL-GCL and RPE are detected by adapting a multiregional graph cut segmentation technique [SMA11], that includes a kernel induced segmentation functional and a continuous multiplier based max-flow algorithm [YBT10]. Figure 6.3 shows the illustration of the segmentation method.

The bias correction operation [TAC+10b] discussed in chapter 3 is used to correct the intensity inhomogeneity and remove noise from the image. This pre-processing operation enhances the boundaries of the layers, which reduce false positives during the segmentation process. Figure 6.4 shows the results of the bias correction operation, where 6.4(c) is the corrected image with well-defined layers boundaries.

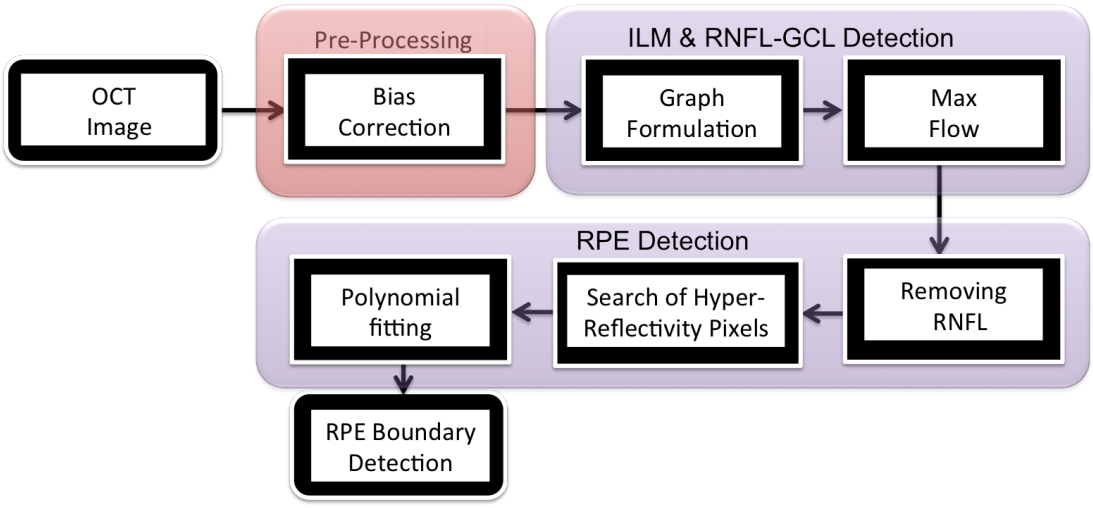

Figure 6.3: Algorithm of the segmentation method.

6.3.1 Graph construction for the Detection of ILM and RNFL-GCL Boundaries

The detection of the first two boundaries (ILM and RNFL-GCL) is performed by adapting the method proposed in [SMA11] and [YBT10], which used a multiregional graph cut segmentation via a kernel and a continuous Max-Flow respectively. A segmentation graph is constructed with a data term that uses a kernel induced function. The operation of the kernel consists of mapping the original nonlinear image data into a higher dimensional kernel space to allow better separability (linear) in the SD-OCT data space. The resulting graph formulation is optimised by a continuous Max-Flow [YBT10] designed to find the minimal energy in the graph segmentation, and provided a global optimisation.

To perform the segmentation of the ILM and RNFL-GCL boundaries, we represent each circular B-scan image as a graph $G(\nu, \epsilon)$ consisting of a set of vertex or nodes (pixels) ν and a set of directed edges ϵ connecting neighbouring pixels. In the circular B-scan image nested grid, the graph contained two special terminal nodes, a foreground terminal (source s) in our case the ILM and RNFL-GCL pixels and a background

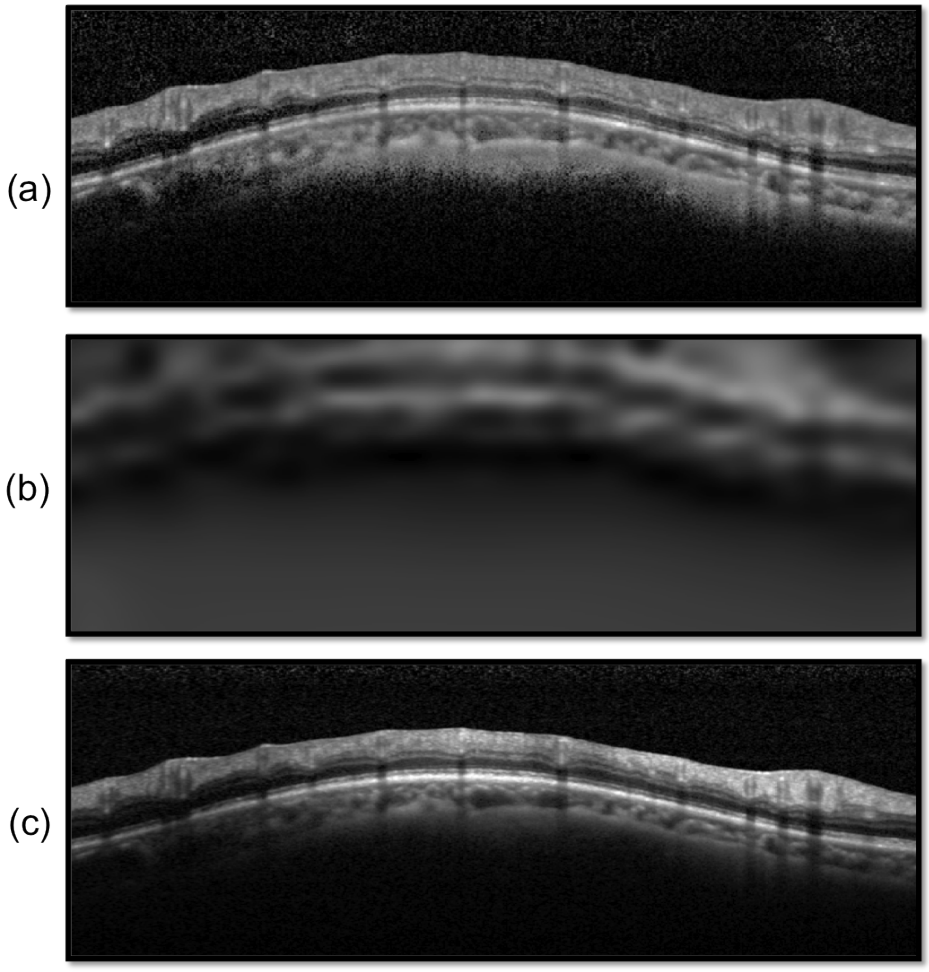

Figure 6.4: Pre-processing. **(a)** SD-OCT circular scan image. **(b)** Bias image. **(c)** Bias corrected image.

terminal (sink t). The edge set ϵ includes the (n-links) linking two neighbourhood nodes in the image grid and the terminal links or data edge (s-links and t-links) connecting the source s and sink t to each node in the image grid respectively. Each pixel $p \in \Omega$ (a set of pixels) in the grid is connected to the terminals by s-links with $\{p, s\}$ and t-links with $\{p, t\}$ while a pair of neighbouring pixels $\{p, q\} \in N$ (number of pixel neighbour) is connected by n-links [BJ01]. The set of connected edges provides a pathway through which one can travel across the graph. The path preferences are created by assigning non-negative weight (cost) $W_e > 0$ to each edge $e \in \epsilon$. To obtain good segmentation results of the boundaries, the preferred path should have the minimum total weights

of edges for travelling from a start node to an end node of the graph. The resulting path from this operation represents the cut, which separates the image into two disjoint partitions, including ILM + RNFL-GCL layer and the background.

If we denote s-t the cut that separates the image into two disjoint partitions, this cut can be defined by a subset of edges $C \in \epsilon$ where $G(c) = \langle \nu, \epsilon \backslash C \rangle$. C is defined as $|C| = \sum_{e \in C} W_e$. The segmentation into two disjoint regions can be expressed as:

$$\epsilon = N \bigcup_{p \in \Omega} \{\{p, s\}, \{p, t\}, \nu = \Omega \cup \{s, t\}\} \tag{6.1}$$

$$\epsilon = F_g \bigcup B_g, \quad F_s \cap B_t = \emptyset \tag{6.2}$$

F_g are pixels labelled as foreground (ILM, RNFL-GCL boundaries) while B_g are the pixels mapped as background.

The energy for each cut which is defined as the minimum total weights of edges can be defined [YBT10] as:

$$\min \; C \in \epsilon \sum_{e \in C} W_e \tag{6.3}$$

This cut is computed by a computationally efficient continuous multiplier based max-flow algorithm [YBT10].

To define the segmentation functional of the graph, let us assume a binary labelling set $A = (A_1, A_p, \ldots A_P)$, which is assigned to each pixel $p \in \Omega$ in the circular image grid and let A_p indicate assignment to pixels $p \in \Omega$. Each assignment A_p in the circular image grid is either in the foreground Fg (ILM, RNFL-GCL) boundaries or background (Bg). Thus the segmentation functional can be defined as:

$$E(A) = \lambda \cdot R(A) + B(A). \tag{6.4}$$

where $R(A)$ is the data term (regional term) that measures the similarity between

neighbouring pixels in a circular image Ω. $B(A)$ is the prior (boundary term), for smoothing regions boundaries and λ a positive coefficient indicating the relative importance of the regional term against the boundary term. The regional (the likelihood of the foreground and background) can then be written as:

$$R(A) = \sum_{p \in \Omega} R_p(A_p) = \sum_{A_p \in A} \sum_{p \in S_{A_p}} -\log\left(I_p / S_{A_p}\right). \tag{6.5}$$

where S_{A_p} is the image region whose label is A_p and $\left(I_p / S_{A_p}\right)$ is the conditional probability of a pixel in data grid given a model distributions within each image region. If κ_{A_p} is the piecewise constant model parameter of image region or image region parameter S_{A_p}, the data term (6.5) can be expressed as:

$$R(A) = \sum_{p \in \Omega} R_p(A_p) = \sum_{A_p \in A} \sum_{p \in S_{A_p}} \left(\kappa_{A_p} - I_p\right)^2. \tag{6.6}$$

The boundary term is expressed as follows:

$$B(A) = \sum_{p,q \in N} B_{p,q} \cdot \phi(A_p, A_q) \tag{6.7}$$

For $A_p \neq A_q$

$$\phi(A_p, A_q) = 1$$

$$\phi(A_p, A_q) = 0 \text{ Otherwise}$$

$$B_{p,q} = exp(-\frac{(I_p - Iq)^2}{2\sigma^2}) \cdot \frac{1}{dist(p,q)} \tag{6.8}$$

where $R_p(A_p)$ assigns pixel p to either ILM, RNFL-GCL boundaries (Fg) or the background (Bg). $B_{p,q}$ indicates the discontinuity between neighbouring pixels. The value of $B_{p,q}$ is large when I_p and I_q are similar and it is close to zero when I_p and I_q are different.

The data term of the graph formulation is defined by first transforming the image data implicitly using a kernel function where the piecewise constant model of the graph cut formulation is applicable. This operation allows a better partition of a non-linearly separable data [SMA11]. If we consider $\psi(.)$ as a non-linear mapping from a data space Θ to a higher dimensional feature space Δ. The graph cut formulation in (6.4) becomes:

$$E\left(\{\kappa_{A_p}\}, A_p\right) = \sum_{A_p \in A} \sum_{p \in S_{A_p}} \left(\psi\left(\kappa_{A_p}\right) - \psi\left(I_p\right)\right)^2 + \lambda \sum_{p,q \in N} B_{p,q} \cdot \phi\left(A_p, A_q\right). \tag{6.9}$$

Thus a kernel induced space image segmentation with the graph cut would simply result in finding the labelling which minimises the graph formulation (6.9).

Using Mercer's theorem [MMR+01], the kernel function can be expressed as a dot product in a high dimensional space[SMA11], therefore there is no need to explicitly know the mapping $\psi(.)$. Consequently a kernel function can be expressed as:

$$F(Y, Z) = \psi(Y)^T \cdot \psi(Z), \quad \forall (Y, Z) \in \Theta^2. \tag{6.10}$$

where $(\cdot)$ represents the dot product in the feature space.

Substitution of the kernel functions from (6.10) provides

$$\begin{aligned} D_k\left(I_p, \kappa\right) = \|\psi(I_p) - \psi(\kappa)\|^2 &= \left(\psi(I_p) - \psi(\kappa)\right)^T \cdot \left(\psi(I_p) - \psi(\kappa)\right) \\ &= \psi(I_p)^T \psi(I_p) - \psi(\kappa)^T \psi(I_p) - \psi(I_p)^T \psi(\kappa) + \psi(\kappa)^T \psi(\kappa) \\ &= F\left(\psi(I_p), \psi(I_p)\right) + F\left(\psi(\kappa), \psi(\kappa)\right) - 2K\left(\psi(I_p), \psi(\kappa)\right) \end{aligned} \tag{6.11}$$

(6.11) gives a non-Euclidean distance measure in the original data space that corresponds to the square norm in feature space [SMA11], where $\kappa \in \kappa_{A_p}$. Simplifying (6.11) and substituting in (6.9) gives the kernel induced segmentation function [SMA11] as:

$$E\left(\{\kappa_{A_p}\}, A_p\right) = \sum_{A_p \in A} \sum_{p \in S_{A_p}} D_F\left(I_p, \kappa_{A_p}\right) + \lambda \sum_{p,q \in N} B_{p,q} \cdot \phi\left(A_p, A_q\right). \tag{6.12}$$

The kernel induced segmentation functional expressed in (6.12) depends on the labelling function A and the image region parameter κ_{A_p}.

In our implementation, we use the Radial basis function kernel (RBF) experimentally, because it gives the best experimental results in the detection of ILM and RNFL-GCL boundaries compare to other kernel functions such as sigmoid kernel and polynomial kernel. The value of sigma was defined experimentally. The kernel function is defined by:

$$F(Y, Z) = \exp\left(-\frac{\|Y - Z\|^2}{\sigma^2}\right). \tag{6.13}$$

The functional in (6.12) is optimised using a continuous multiplier based max-flow algorithm. The multiplier based max-flow algorithm is used because it splits the optimisation problem into simple sub problems over independent flow variables and is globally optimised.

6.3.2 Graph Optimisation for the Detection of ILM, RNFL-GCL Boundaries

The segmentation functional (6.12) is optimised using a continuous multiplier based max-flow algorithm [YBT10]. The max-flow algorithm consists of finding the partitions of the circular image such that the energy functional in (6.12) is minimal.

This optimisation operation separates the circular image into retinal RNFL boundaries (ILM+RNFL-GCL) and the photoreceptor layer that includes the RPE layer. Figure 6.5 shows the segmentation results of the proposed method of ILM and RNFL-GCL boundaries.

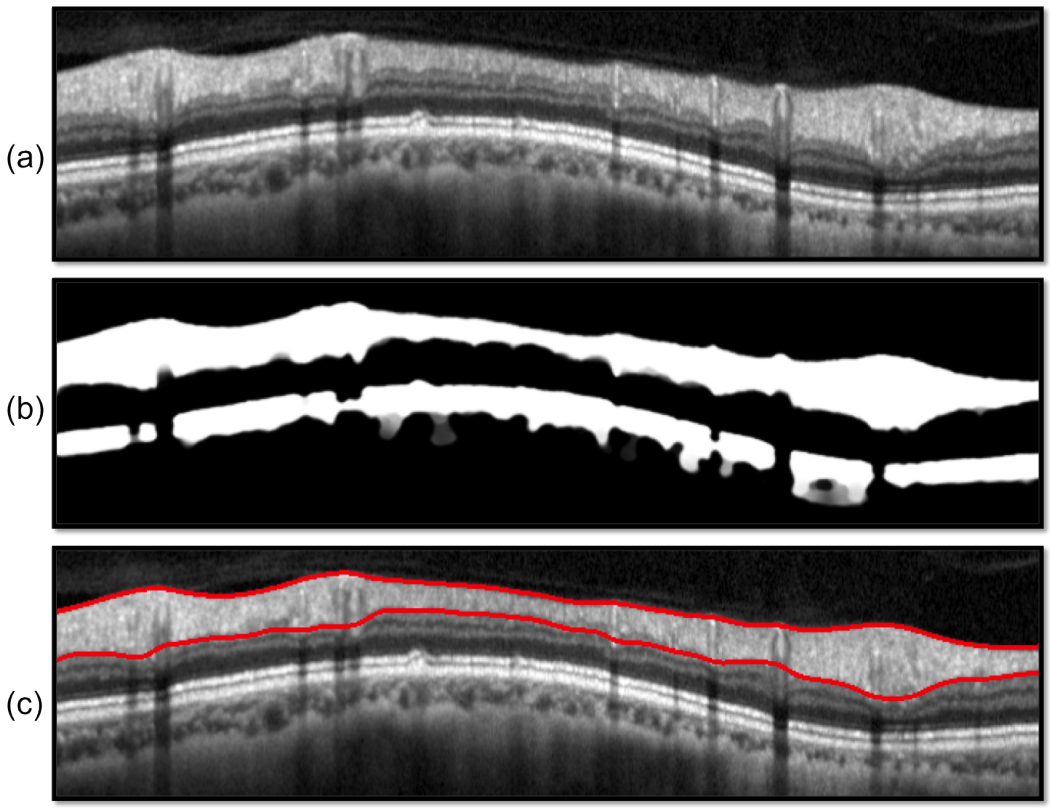

Figure 6.5: ILM and RNFL-GCL boundaries detection. **(a)** Circular scan image. **(b)** Segmented binary image. **(c)** ILM and RNFL-GCL boundaries in red.

6.3.3 Detection of the RPE layer Boundaries

The RPE layer detection is performed using prior knowledge about the SD-OCT image and its features. Based on clinical and tomographical correlation studies [CSMJ+06], it had been suggested that the RPE-choriocapillaris layer exhibits the most hyper-reflectivity layer in the retinal SD-OCT imaging. While the RNFL represents some of the hyper-reflectivity pixels at the top of the retinal SD-OCT image see Figure 6.6(a).

To segment the RPE layer, we first perform the search for all the hyper-reflectivity pixels (highest intensity values) in circular scam image. These pixels correspond to the most reflective layer (RPE). However to prevent the algorithm from selecting hyper-reflectivity pixels in the RNFL that also exhibit some bright pixels, it is helpful to constrain the search to a region of interest (RPE layer). The boundaries of the RNFL

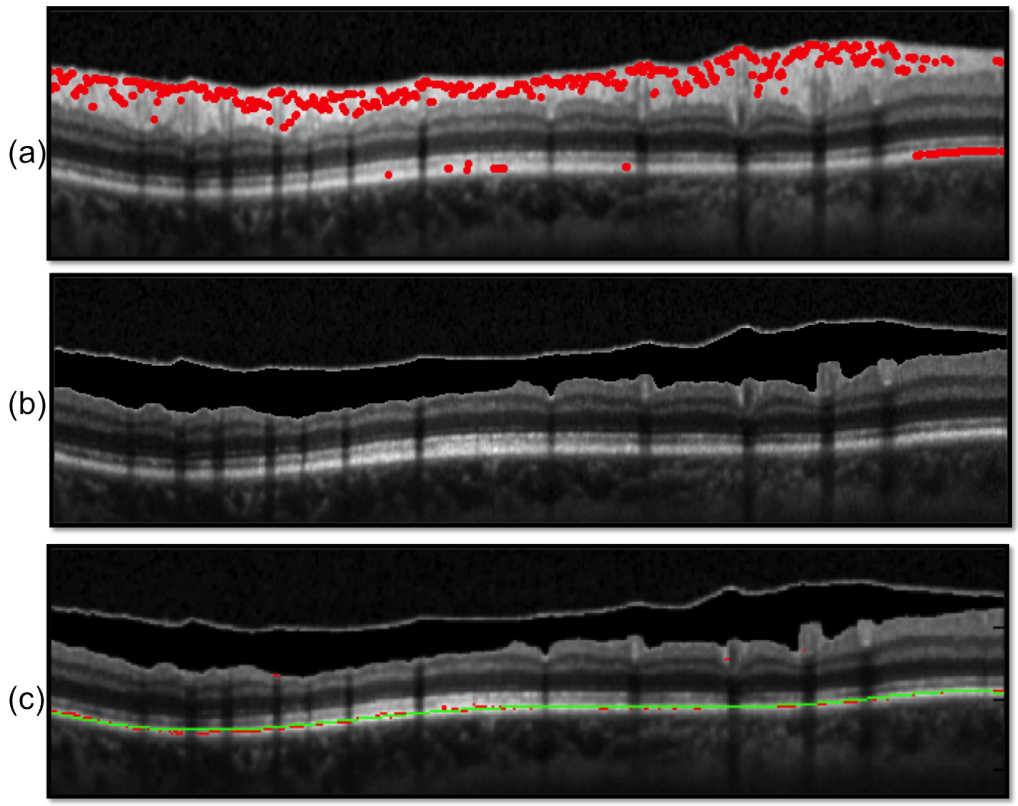

Figure 6.6: RPE boundary detection. **(a)** Hyper-reflectivity pixels in red on RNFL layer. **(b)** Selection of region of interest. **(c)** RPE boundary in green.

is already accurately detected in Section (6.3.1), thus we may set all pixels belonging to the RNFL to zero before searching for the hyper-reflectivity pixels. By setting the RNFL pixels to zero, the search area of the bright pixels is limited to the space shown in Figure 6.6(b).

After the selection of all the hyper-reflectivity points in the region of interest, a polynomial curve fitting process is used to construct a curve that has the best fit to the series of hyper-reflectivity pixels. The degree of the polynomial curve in our case was set to 6. Results of the segmentation of the RPE using the polynomial curve fitting are shown in Figure 6.6(c).

6.4 Experiments

The data used in this study was obtained from continuing research and prevention on retinal diseases such as glaucomatous damage, diabetic retinopathy, age-related, optic neuropathy, macular degeneration or other significant retinal diseases in Tongren Eye Hospital. 120 SD-OCT circular scans around ONH were obtained from patients with an age range of 20-85 years. The scans of both eyes of each patient was acquired with a high-resolution SD-OCT Spectralis HRA+OCT (Heidelberg Engineering, Germany). The SD-OCT imaging of the optic nerve was performed using a scan protocol that applies a circle of diameter 3.4 mm centred on the ONH. Figures 6.2 shows the scan process of the retinal optic nerve. In Figure 6.2(a) a green circular scanning path of diameter 3.4 mm centred on the ONH of OCT fundus image is used to capture a scan of the retinal layers tissues see 6.2(b). Figure 6.2(c) transformation of the circular scan into a 2-D OCT cross-sectional image (B-scan) of the layers tissues with different layers boundaries definitions.

6.4.1 Segmentation Accuracy

In this study three retinal boundaries were evaluated including ILM, peripapillary RNFL-GCL and the RPE as well as the thickness of the RNFL. The measurement of these boundaries plays an important role in the application of the OCT imaging in diagnosis and prevention of retinal diseases such as glaucomatous damage.

To evaluate accurately the segmentation of the ILM, RNFL-GCL and the RPE boundaries by the proposed method, the results of the segmentation were compared to the manual annotations of the ILM, RNFL-GCL and the RPE in the circular scans. The mean absolute deviation (MAD), the root-mean-square (RMSE) and the dice coefficient were used to evaluate the method on the ILM, RNFL-GCL and the RPE against the corresponding manually labelled images. The MAD, RMSE and the Dice coefficient are computed as follow:

$$
\begin{aligned}
\mathrm{M}AD(\mathrm{GT},\mathrm{SEG}) &= 0.5 * \left(\frac{1}{n}\sum_{i=1}^{n} d(pt_i,\mathrm{SEG}) + \frac{1}{m}\sum_{i=1}^{m} d(ps_i,\mathrm{GT}) \right) \\
\mathrm{RMSE} &= \sqrt{\frac{1}{n}\sum_{i=1}^{n}(\mathrm{SEG}_i - \mathrm{GT}_i)^2} \\
\mathrm{Dice} &= \frac{2|\mathrm{GT}_i \cap \mathrm{SEG}_i|}{|\mathrm{GT}_i| + |\mathrm{SEG}_i|}
\end{aligned}
\tag{6.14}
$$

where SEG_i is the pixel labelled as retinal Layer by the proposed segmentation method and GT_i is the true retinal layers pixel in the manual annotation image. pt_i and ps_i represent the coordinates of the images, $d(pt_i, \mathrm{SEG})$ is the distance of pt_i to the closest pixel on SEG with the same segmentation label, $d(ps_i, \mathrm{GT})$ is the distance of ps_i to the closest pixel on GT with the same segmentation label, n and m are the number of points onSEG) and GT respectively.

In addition, further evaluation was conducted on the area between the anterior (ILM) and posterior (RNFL-GCL) boundaries of the RNFL (RNFL thickness) using the following evaluation measurement.

$$
\begin{aligned}
\mathrm{TPR} &= \frac{\mathrm{TP}}{\mathrm{GT}_{\text{RNFL pixels}}} \\
\mathrm{FPR} &= \frac{\mathrm{FP}}{\mathrm{GT}_{\text{Non RNFL pixels}}}
\end{aligned}
\tag{6.15}
$$

where TP is the true positive, FP is the false positive and $\mathrm{GT}_{\text{RNFL pixels}}$ and $\mathrm{GT}_{\text{Non RNFL pixels}}$ represent the manually labelled RNFL layer pixels and non RNFL pixels in the image. Also TPR, FPR are the true positive rate (sensitivity) and the false positive rate.

Table 6.1 shows the evaluation of the proposed method on 120 OCT scans including 100 healthy and 20 diseased retina. The RPE boundary detection of all the 120 images with mean RMSE $= 0.0124 \pm 0.0124$ and MAD $= 0.2131 \pm 0.3108$ has the lowest boundary error against the other layers boundaries (ILM and RNFL-GCL). The

All Images	Mean RMSE	Mean MAD
ILM	0.0453(0.0276)	0.3931(0.2905)
RNFL-GCL	0.0582(0.0329)	1.2785(1.0523)
RPE	0.0124(0.0124)	0.2131(0.3108)

Table 6.1: **Performance evaluation with RMSE (Standard deviation) and MAD (Standard deviation) for each boundary. The values have units of pixels** - 120 OCT Scans.

Heathy images	Mean RMSE	Mean MAD
ILM	0.0474(0.0286)	0.4166(0.3023)
RNFL-GCL	0.0610(0.0312)	1.3835(1.0683)
RPE	0.0103(0.0084)	0.1504(0.2565)
Unhealthy images	**Mean RMSE**	**Mean MAD**
ILM	0.0346(0.0198)	0.2753(0.1867)
RNFL-GCL	0.0440(0.0382)	0.7536(0.8002)
RPE	0.0072(0.0129)	0.1379(0.2814)

Table 6.2: **Performance comparison of healthy versus disease images** -OCT Scans.

algorithm achieves such a high performance on the RPE boundary detection because it segments the boundary using polynomial fitting as well as removing all the other hyper-reflectivity pixels in the image. While in the literature, the RPE boundary is considered as the most difficult boundary to detect since it has the most hyper-reflectivity pixels and it is not always visible through all OCT images as it has tendency to appear and disappear [LCS+13]. This phenomenon is due to the blood vessels artefacts (shadows) in the OCT retina image.

The ILM boundary detection also has a very low boundary error with mean values of RMSE $= 0.0453 \pm 0.0276$ and MAD $= 0.3931 \pm 0.2905$. This low error is expected because the ILM boundary is the location where the retinal tissue layer in the OCT image has a large gradient, as it is the area where the background and retina tissue intersected. However the RNFL-GCL boundary also has a low mean RMSE $= 0.0582 \pm$ 0.0329 and a reasonably high MAD $= 1.2785 \pm 1.0523$. This large error is caused by the presence of the blood vessels shadows on the RNFL- GCL boundary, while manual segmentation ignores the vessels artefacts. Including these areas of the vessels in the

automated segmentation can also leaded to some error in assessing the retinal layer thickness. Figure 6.7(b) shows the segmentation results of the RNFL-GCL boundary with some blood vessels artefacts indicated with blue arrays.

Table 6.2 shows the evaluation of the proposed method on healthy and diseased retina including 100 healthy and 20 diseased images. Similar to Table 6.1, in Table 6.2 the RPE boundary achieved the best overall segmentation value in both healthy and diseased images followed by ILM boundary. The proposed method performed well on both healthy and diseased images.

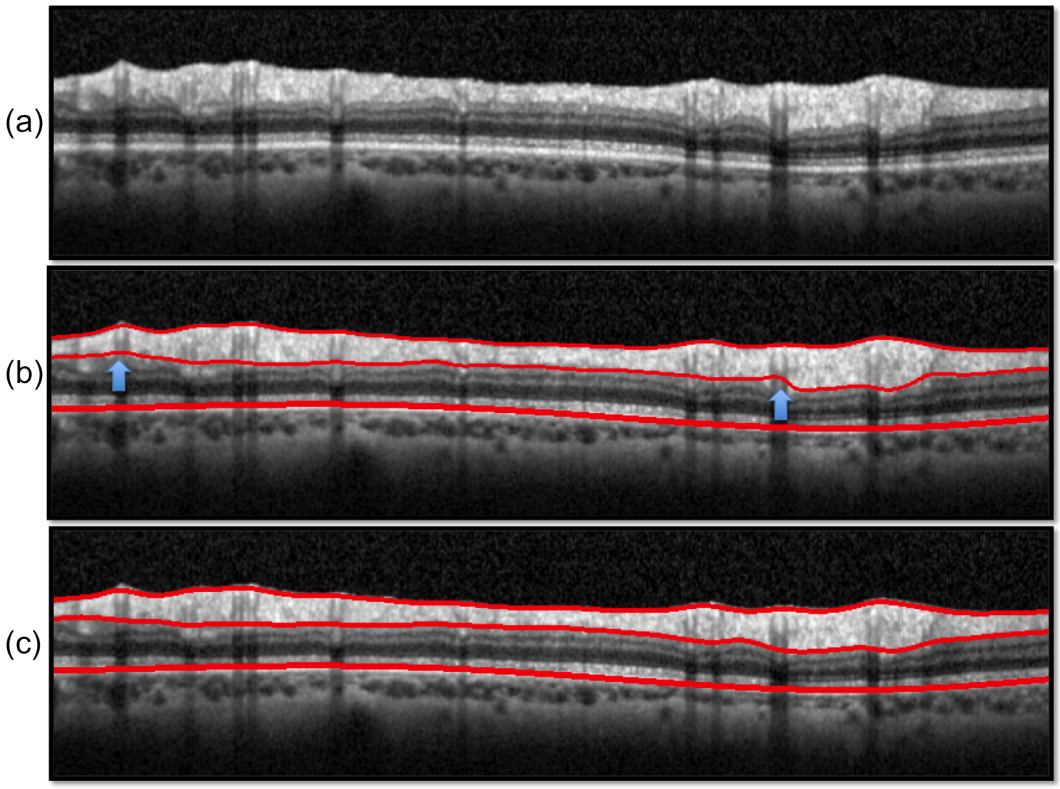

Figure 6.7: Results. **(a)** Circular scan. **(b)** Segmentation result of the proposed method. **(c)** Human manual grading image.

Table 6.3 shows the values of the TPR, FPT and Dice coefficient of the performance evaluation between the estimated RNFL thickness and the true RNFL thickness. With the value of TPR = 97.46%, our method achieves very good segmentation results and it is comparable to the results of the manual segmentation. However the value

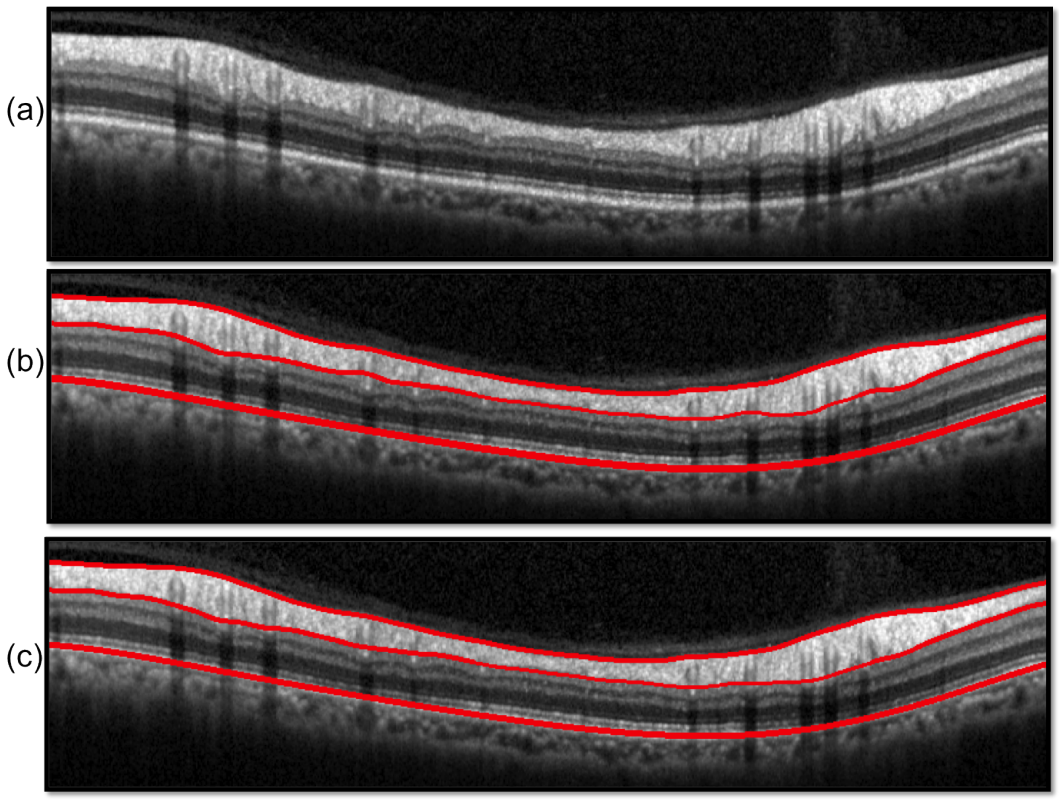

Figure 6.8: Results. **(a)** Circular scan image. **(b)** Segmentation result of the proposed method. **(a)** Human manual grading image.

of the FPR = 8.67% is slightly higher, this is largely due again to the blood vessels artefacts around the RNFL-GCL boundary, where the vessels appear as a false positive. To solve this problem [NVT+13] included the blood vessels areas in the OCT image from the accuracy evaluation to improve the segmentation errors. Considering the value of the Dice coefficient Dice = 0.9468 ± 0.0705, RMSE = 0.0835 ± 0.0495 as performance measures, the proposed method performs well for the segmentation of the RNFL thickness. Similar to the results in Table 6.1 and Table 6.2, Table 6.3 also shows higher performance of the proposed method on pathological retina with TPR = 98.59% and FPR = 5.57%. These results are due to the large gradient on the region of the ILM boundary and the thin RNF in diseased retina. Figure 6.8 shows the comparison of the proposed segmentation results on the ILM, RNFL-GCL and RPE boundaries and the Human manual grading images.

Images	RNFLT	std	conf
Mean TPR	0.9746	0.0665	±0.0119
Mean FPR	0.0867	0.1037	±0.0186
Mean Dice	0.9468	0.0705	±0.0126
Mean RMSE	0.0835	0.0495	±0.0089
Heathy images			
Mean TPR	0.9792	0.0230	±0.0045
Mean FPR	0.0919	0.0947	±0.0186
Mean Dice	0.9473	0.0404	±0.0079
Mean RMSE	0.0881	0.0418	±0.0082
Unhealthy images			
Mean TPR	0.9859	0.0215	±0.0042
Mean FPR	0.0557	0.0970	±0.0190
Mean Dice	0.9676	0.0401	±0.0079
Mean RMSE	0.0586	0.0521	±0.01021

Table 6.3: **Performance evaluation of TPR, FPR, Dice coefficient and RMSE, Standard deviation (Std) and the** 95% **Confidence interval between the estimated RNFL thickness and the true RNFL thickness** -OCT Scans.

6.4.2 RNFL Thickness Profiles

In addition to the evaluation of the RNFL thickness, we provided the RNFL thickness profile graph. The thickness profile graph provides the following information:

- The RNFL thickness profile measured along the circular scan of the retina;
- The RNFL thickness profile of the normative database, allowing the comparison of our segmentation thickness values to the normal range.

This thickness profile graph is obtained from a normative database compiled by Spectralis HRA+OCT (Heidelberg Engineering GmbH, Germany). Figure 6.9 shows the thickness profile graph, where the x-axis indicates the length of the circular scan (position in degree) and the y-axis displays the RNFL thickness in pixels. The colour coding of the thickness profile graph indicates whether a given retina thickness is within normal limits (green), outside the normal limits (red) or on the border of normal limits (yellow).

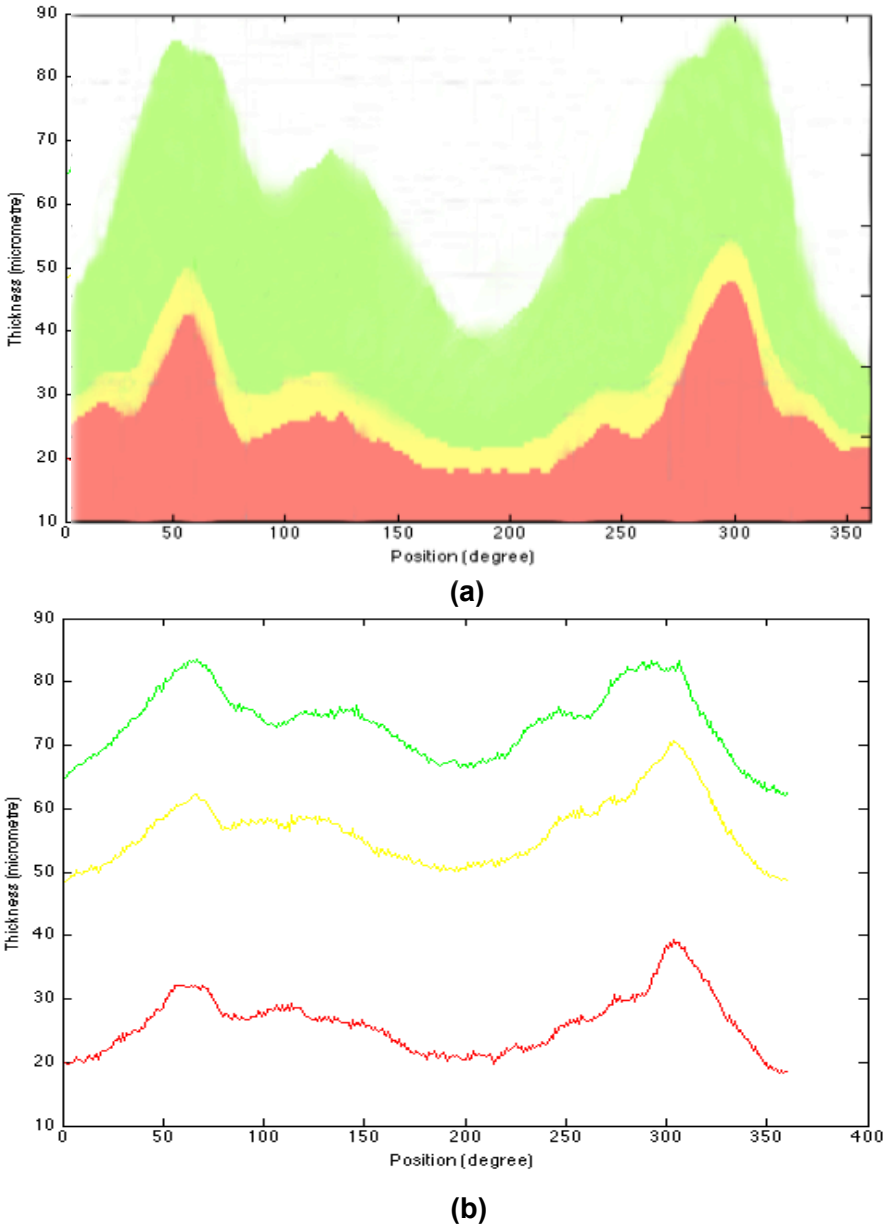

Figure 6.9: **(a)** Normative database of retinal RNFL thickness. **(a)** Proposed method RNFL thickness profile: Green Healthy, Yellow Risk, Red Glaucoma.

The healthy eyes (normal limits or green) is indicated by the thickness values that fall within the range of $5^{th} - 95^{th}$ percentile of the RNFL normal profile distribution. Any RNFL thickness values within this range are considered healthy eyes.

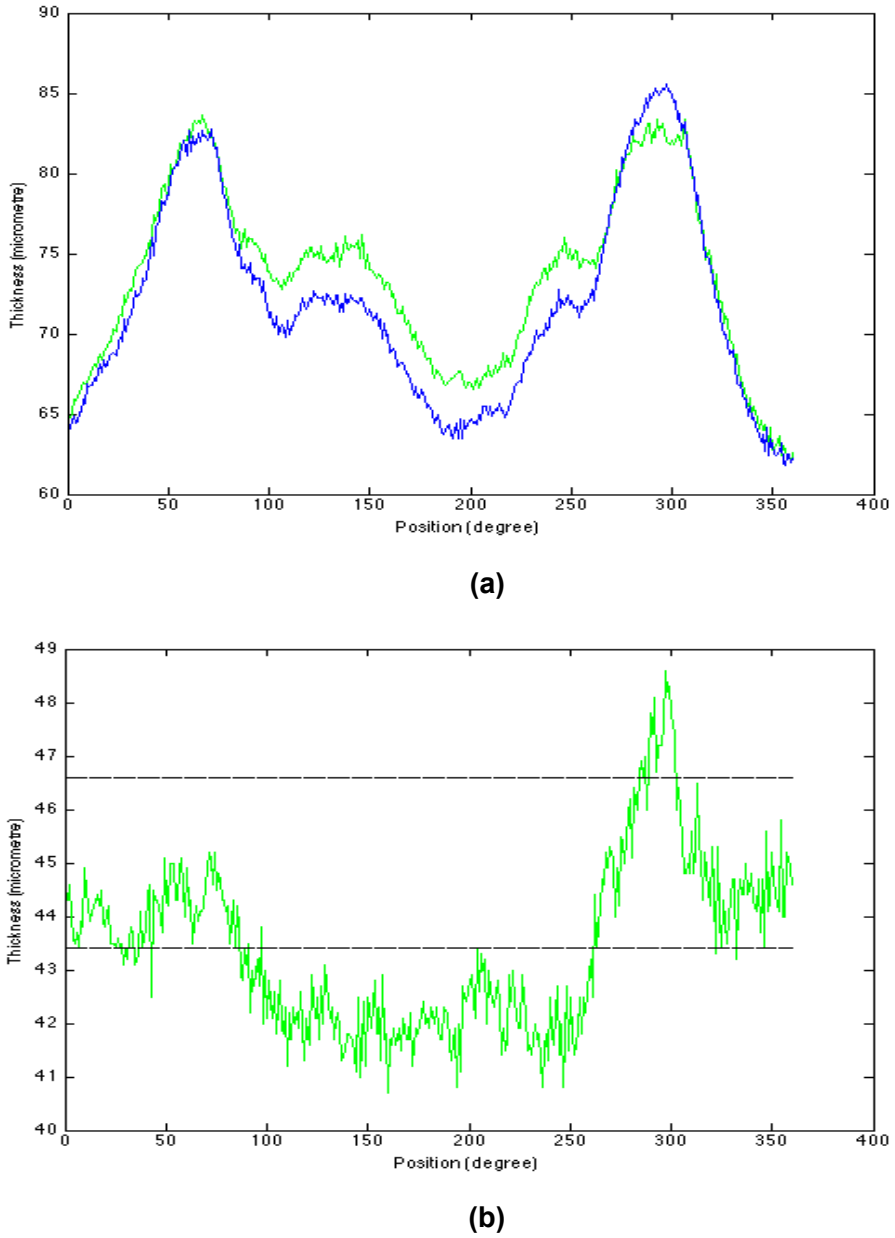

Figure 6.10: Results. **(a)** RNFL thickness profile of healthy retinal images: Green proposed segmentation method, Bleu Manual segmentation. **(b)** Error in RNFL thickness profile of healthy retinal images: Green the error, Black lines the standard deviation.

The diseased eyes (red or outside normal limits) is defined when the thinness values are below 1^{st} percentile of the RNFL thickness of normal distribution. Any RNFL thickness values within this range are considered disease eyes.

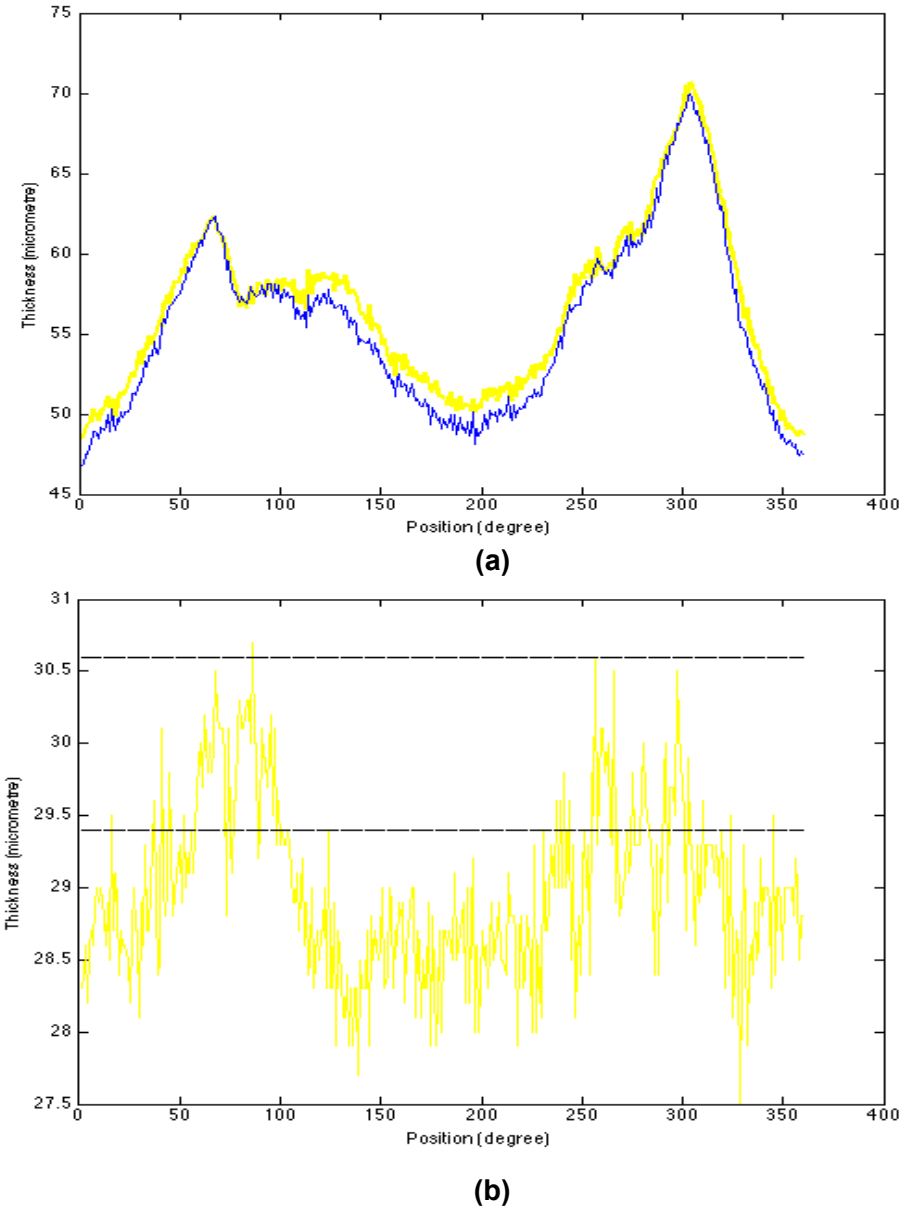

Figure 6.11: **(a)** RNFL thickness profile of retinal images with risk of glaucoma: Yellow proposed segmentation method. Blue Manual segmentation. **(b)** Error in RNFL thickness profile of retinal images with risk of glaucoma: Yellow the error and Black lines the standard deviation.

The thickness values within the yellow region are values that are below the 5^{th} but above the 1^{th} percentiles of normal thickness distribution. So any RNFL thickness values at this range are at risk of developing the diseases (borderline). Figure 6.9 shows

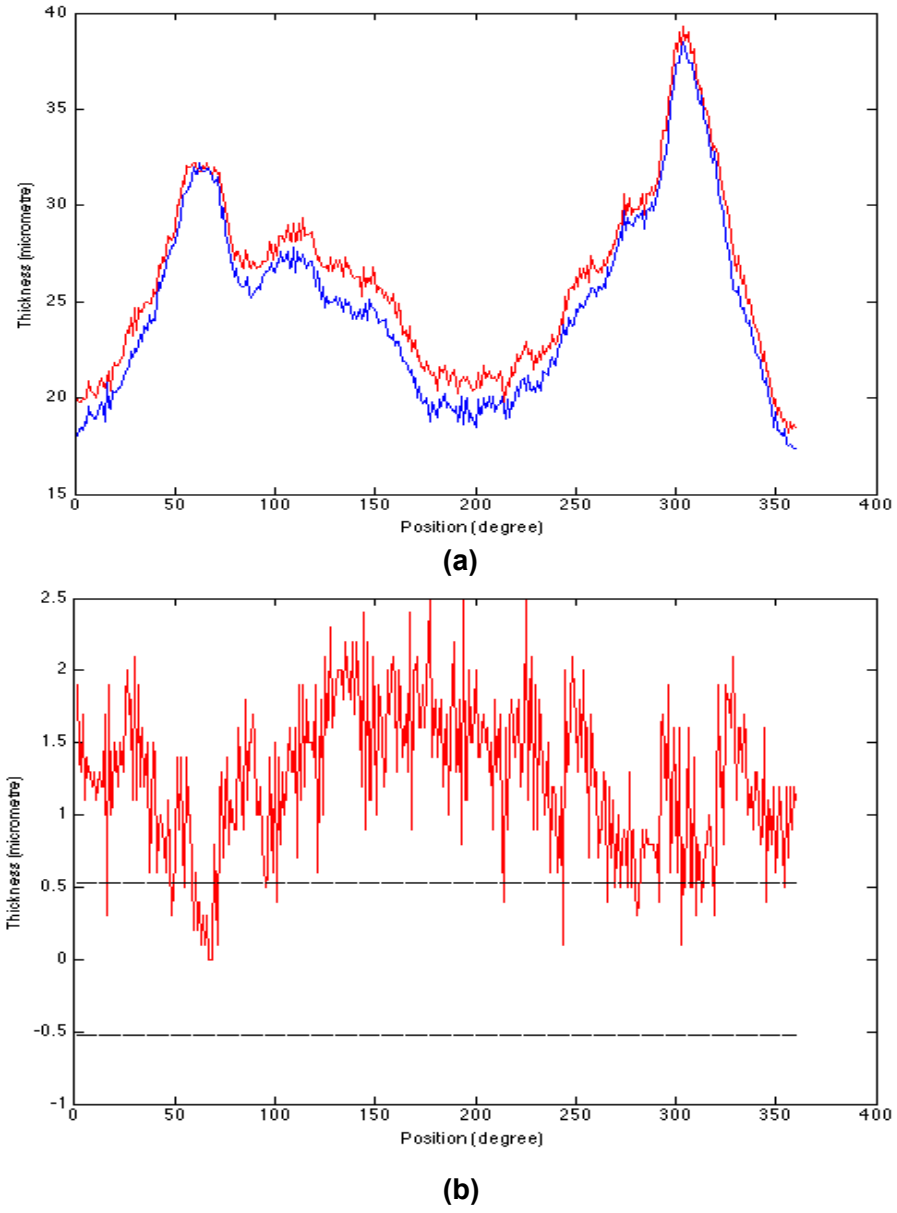

Figure 6.12: **(a)** RNFL thickness profile of retinal images with glaucoma: Red proposed segmentation method. Blue Manual segmentation. **(b)** Error in RNFL thickness profile of Glaucoma retinal images: Red the error, Black lines the standard deviation.

the RNFL thickness profile for healthy retina in green, retina at risk in yellow and in red the glaucoma retina.

In Figure 6.10(a), we provide the average thickness profile graph of the proposed method on 100 healthy images in Green compared to manually segmented healthy images in blue and Figure 6.10(b) shows the profile error of healthy retinal images. The results of this graph show effective agreement with manual annotations and the normative database as the thickness values of the graph are within the normal limits (green). Figure 6.11(a) also shows the average thickness profile graph of the proposed method on 10 retinal images with risk of developing glaucoma in yellow and the corresponding manually segmented images in blue. Figure 6.11(b) shows the corresponding error of the profile representation. Similarly, the results in Figure 6.11(a) also demonstrated successful agreement with normative database since the thickness values of the graph are within the borderline (yellow).

Figure 6.4.2(a) shows the average thickness profile graph of the proposed method on 10 glaucoma retinal images in red and the corresponding manually segmented images in blue and the corresponding error profile is also shown in red in Figure (b). The results also show successful agreement with the normative database since the thickness values of the graph are within the borderline (red).

6.5 Summary

This study presents an automated approach for retinal layers segmentation by integrating the mechanism of the kernel mapping into the graph cut technique and the polynomial-fitting algorithm. The overall process includes a pre-processing step that enhances the contrast of the retinal layers in the SD-OCT circular scan image around the ONH using a bias correction operation and a segmentation step that includes kernel graph cuts and continuous max-flow algorithms. The method proved to be flexible, accurate, robust and fast, leading to successful segmentation results of the three main retinal layers boundaries used to assess and monitor retinal diseases such as glaucomatous damage. However there are many aspects of this study that can be improved.

This includes the removal of blood vessel artefacts in the OCT image without affecting the RNFL thickness measurements and the extension of the proposed method to 3-D OCT image segmentation. The advantage of the 3-D retinal layers segmentation is to use the contextual information in the 3-D structure to improve the segmentation of different layers and also allows the detection of more intra-retinal layers.

Part III

Conclusion

Chapter 7

Conclusion and Future Work

Over the course of the past few years, research in computer-aided diagnosis has been accelerating in aspects affecting all areas of the medical field. The incentive for this is obvious, the analysis of medical images can be time consuming, tedious and subjective when it is done by hand.

The introduction of computer-aided diagnosis in retinal image analysis brought about a new platform for early detection of retinal diseases as well as cardiovascular disorders. The structures of the retina such blood vessels, optic disc and RNFL are considered to be a key indicator of diseases such as diabetic retinopathy, glaucomatous damage, age-related macular degeneration, hypertension, the risk of stroke and myocardial infraction just to listed a few. Therefore an accurate and effective segmentation of these structures can improve the productivity of ophthalmologists and eye experts by reducing the time required for diseases assessment as well as reducing the cost of the eye screening.

The previous retinal image segmentation methods have led to a familiarity with the retina structures that was beneficial in the implementation of automated segmentation techniques capable of extracting a variety of retinal features. However, the imaging artefacts such as noise, intensity homogeneity and the overlapping tissue of retina structures can cause significant degradations to the performance of these automated

image analysis tools.

The aim of this thesis is to provide robust and reliable automated retinal image analysis technique to facilitate early detection of various retinal and other diseases. Thus we proposed five innovative segmentation methods, including two for retinal vessel network segmentation, two for optic disc segmentation and one for retina nerve fibre layers detection. The strong experimental results, obtained on several public and other datasets as well as the comparison with existing methods in the literature, have shown that our proposed methods are robust and efficient in the segmentation of retinal images.

7.1 Blood Vessel Segmentation

In this thesis, we provide two novel methods for retinal blood vessel network segmentation. The first method in chapter 3 uses the pixel processing approach for complete extraction of the retina vascular tree fundus retinal images.

This segmentation technique is performed in two-pass operations. A pre-processing stage, which combines the bias correction operation, an adaptive histogram equalisation and a distance transform. This pre-processing technique removes noise and adjusts the contrast of the blood vessels in the image. A distance map of the blood vessel network is created using a distance transform operation. This operation enhances blood vessel network and finally a probabilistic modelling including EM is applied to segment the vascular tree.

This method was evaluated on two fundus image datasets from different sources (STARE and DRIVE) and the results were also compared to alternative methods in the literature. The overview of the experimental results shows that our segmentation method achieves the best overall performance. This result is mainly achieved by the combination of the three pre-processing operations (bias correction, adaptive histogram equalisation and distance transform), which removed all the imaging artefacts but kept

most of the arrow blood vessels. The probabilistic modelling method segments thin blood vessels and also minimises the segmentation of the optic disc boundary and the lesions in the unhealthy retinal images.

The probabilistic modelling method achieves better results over other pixel processing based methods because it corrects the imaging artefacts in the fundus retinal images by combining efficient and robust image processing operations in the pre-processing stage. The blood vessel extraction is also performed by a probabilistic method capable of segmenting thin blood vessels. The proposed methods have advantages over traditional tracking-based methods because they are capable of segmenting a complete blood vessel network and they are not affected by the discontinuities in the vessel branches, which cause significant degradations in the performance of tracking-based methods. However, like a traditional pixel processing method, the proposed method is a low-level segmentation technique as it processes all the pixels in the fundus retinal photograph to perform the classification of both vessel and background pixels.

A graph cut segmentation operation was implemented to improve the probabilistic modelling method by speeding up the blood vessel segmentation process. This method combines both pixel processing and vessel tracking based methods. Like the probabilistic modelling method, we implemented a pre-processing technique, which consists of effective AHE and robust distance transform to enhance the contrast between the blood vessel network and the background. This operation improves the robustness and the accuracy of the graph cut algorithm. The energy formulation of the graph is constructed by integrating the mechanism of flux into the graph cut algorithm. This allows the segmentation of thin blood vessels in the retinal image. The performance evaluation of this method was carried out on STARE and DRIVE datasets. This performance was compared against 25 other alternative methods in the literature. In term of TPR, the proposed method achieves the best overall results on both STARE and DRIVE fundus images.

The graph cut method has advantages over our probabilistic modelling method

and other pixel processing and vessel tracking based methods as it balances the segmentation of the retinal blood vessel by applying pixel processing techniques in the pre-processing stage and vessel tracking approach in the segmentation step. The segmentation process also incorporates the mechanism of vectors flux into the graph formulation, which allows the segmentation of more arrow blood vessels. This method can also achieve high segmentation results on retinal images from a variety of sources without a need of training or adjustments. It could be used to assist ophthalmologists and eye diseases experts in retinal and cardiovascular diseases evaluation, treatment and management by reducing the costs and time required in eye screening examinations.

7.2 Optic Disc Segmentation

Chapter 5 provides two different methods of optic disc segmentation including the Markov random field (MRF) image reconstruction method and the compensation factor method. Both segmentation methods use structural features of the optic disc such a convergence feature of the blood vessel network into the optic disc region and the disc brightness to locate the position of the optic disc in the fundus image. The MRF image reconstruction method performs optic disc segmentation by first removing the blood vessel network from the disc area, which misguides the graph segmentation through a short path, breaking the continuity of the optic disc boundary. Then the graph cut algorithm is used to define the boundary of the optic disc in the reconstructed image. The compensation factor method unlike the MRF image reconstruction method performs the optic disc nerve segmentation using prior information about local intensity of the blood vessel network. This process incorporates the blood vessels into the graph cut formulation by introducing a compensation factor. This factor is derived using prior information about the blood vessel and it minimises the contrast of the blood vessel network in the optic disc area during the detection of the disc boundary.

The proposed methods are tested on 129 fundus retinal images from two public

datasets (DIARETDB1 and DRIVE) including 98 images with variety of lesions. The methods were also compared against three other methods in the literature on the same datasets. On these difficult datasets, our methods demonstrated effective agreement with the manual segmentation and outperform all the others alternative methods to which it was compared.

The key achievement in the optic disc segmentation is that our proposed methods address one of the main issues in medical image analysis known as the overlapping tissue segmentation. The presence of the blood vessel network in the optic disc tissue causes a significant degradation to the optic disc segmentation breaking the disc boundary, this problem is shared with all the optic disc segmentation methods in the literature. Most of the methods address this particular issue by removing the blood vessel in the optic disc area using morphological operations, which can modify the pixel information in the image, hence misguide the segmentation. But we use an efficient and robust vessel removing operation (MRF image reconstruction), which replaces the vessel pixels with neighbouring pixels that have same or similar intensity values. The compensation factor also uses the vessel information to control the breaking of the disc boundary during segmentation. However it is important to note that, both the MRF image reconstruction and compensation factor algorithms depend on the vessel segmentation algorithm, for example if the vessel segmentation algorithm achieved a low performance on severely damaged retinal images, the reconstruction and compensation factor would not defined a meaningful optic disc region, leading to segmentation errors.

We believe that our optic disc methods can be also useful in other applications of the overlapping tissue segmentation. In addition, our optic disc segmentation methods can detect and segment the optic disc in the retinal photograph with no restrictions on the shapes, sizes and locations of the optic disc as well as the sources of the images. They can be used to help assess and manage the gradual cupping of the optic disc in glaucomatous damage considered to be the third most common cause of blindness in the developed world.

7.3 Retinal Layers Segmentation

Since the cause of glaucoma is not fully known and the fact that glaucomatous damage affects the structures of the retina. It is important to assess the change occurring on those structures in the OCT scan to control this disease in addition to the optic disc evaluation in the fundus photograph. The evaluation of the RNFL thickness in glaucomatous damage requires segmentation of different retinal layers. This process can be time consuming and tedious when it is done by hands. In chapter 6, we provide the segmentation of RNFL, which can be used in modern ophthalmology to assist the diagnosis of glaucoma.

The proposed method uses the bias correction operation to remove all the imaging artefacts (noises, intensity inhomogeneity). The layers are detected by adapting a graph cut segmentation technique that includes a kernel-induced space and a continuous multiplier based max-flow algorithm. This approach solves problems related to variation of intensity within layers in the OCT image, which causes errors in the layers boundaries segmentation. These problems affects current RNFL segmentation techniques such pixel intensity variation, active contours, graph cut and machine learning approaches. These issues can also be found in commercially available OCT imaging tools.

The segmentation graph is formulated with a data term that uses a kernel induced function, which maps the original nonlinear image data into a higher dimensional kernel space to allow better separation in the OCT image space. This process addresses the problems of finding appropriate cost functions on the graph formulation to distinguish individual layers, which is often found in the graph-based segmentation methods. The evaluation of the proposed method on 120 OCT scan around the optic nerve head demonstrated effective agreement with manual annotations. We believe that this method can be use in glaucoma evaluation to provide reliable RNFL thickness, which provides key information on glaucomatous damage.

7.4 Future Work

Recently we have been working with clinical doctors at Tongren Hospital in Beijing and Moorfield Eye Hospital in London, the aim of this collaboration is to support them with retinal image analysis algorithms capable of quantifying different retinal tissue layers. Therefore our future work will be mainly based in implementing of computer algorithms capable of analysing accurately and more efficiently the OCT scans. This project can be summarised as follows:

- The detection and the removal of blood vessels artefacts in the OCT image, which cause a significant degradation to the retinal layer segmentation in the OCT scan.
- The segmentation of retinal layers in 3-D OCT, which can provide more contextual information about the retinal layers and improve the segmentation of difference layers as well as allowing the detection of more inter-retinal layers.
- The 3-D blood vessel segmentation in the OCT scans to better understand diabetic retinopathy, age-related macular degeneration and vascular diseases.
- Provide glaucoma assessment tools using both RNFL measurements and the functional visual field point.
- More accurate segmentation of the optic disc using both the 3-D OCT scan and fundus photograph.
- Quantification of retinal blood vessel diameter, tortuosity as well as the optic disc and the cup for better analysis of retinal diseases and cardiovascular disorders.

Part IV

Bibliography

Bibliography

[A+11] Ala Alwan et al. *Global status report on noncommunicable diseases 2010.* World Health Organization, 2011. 51

[AAG+07] Michael D Abràmoff, Wallace LM Alward, Emily C Greenlee, Lesya Shuba, Chan Y Kim, John H Fingert, and Young H Kwon. Automated segmentation of the optic disc from stereo color photographs using physiologically plausible features. *Investigative ophthalmology & visual science*, 48(4):1665–1673, 2007. 116

[ABC+13] Florencia Aguiree, Alex Brown, Nam Ho Cho, Gisela Dahlquist, Sheree Dodd, Trisha Dunning, Michael Hirst, Christopher Hwang, Dianna Magliano, Chris Patterson, et al. Idf diabetes atlas. 2013. 47, 48

[ADD+98] KGMM Alberti, Mayer B Davidson, Ralph A DeFronzo, Allan Drash, Saul Genuth, Maureen I Harris, Richard Kahn, Harry Keen, William C Knowler, Harold Lebovitz, et al. Report of the expert committee on the diagnosis and classification of diabetes mellitus. *Diabetes Care*, 21:S5, 1998. 47, 48

[AGAM10] Arturo Aquino, Manuel Emilio Gegúndez-Arias, and Diego Marín. Detecting the optic disc boundary in digital fundus images using morphological, edge detection, and feature extraction techniques. *Medical Imaging, IEEE Transactions on*, 29(11):1860–1869, 2010. 119

[AGS10] Michael D Abràmoff, Mona K Garvin, and Milan Sonka. Retinal imaging and image analysis. *Biomedical Engineering, IEEE Reviews in*, 3:169–208, 2010. 25, 26, 31, 41, 44, 46, 47, 48, 50, 51, 52, 54, 55, 56, 65, 90

[And] Peter E Andersen. Optical coherence tomography. 59

[ARQA07] Mohammed Al-Rawi, Munib Qutaishat, and Mohammed Arrar. An improved matched filter for blood vessel detection of digital retinal images. *Computers in Biology and Medicine*, 37(2):262–267, 2007. 86, 87, 107, 108, 109, 111

[AS95] Dan K Andersson and Kurt Svärdsudd. Long-term glycemic control relates to mortality in type ii diabetes. *Diabetes care*, 18(12):1534–1543, 1995. 48

[ASG+08] Christian Ahlers, Christian Simader, Wolfgang Geitzenauer, Geraldine Stock, Paul Stetson, Shawn Dastmalchi, and Ursula Schmidt-Erfurth. Automatic segmentation in three-dimensional analysis of fibrovascular pigmentepithelial detachment using high-definition optical coherence tomography. *British Journal of Ophthalmology*, 92(2):197–203, 2008. 139

[BAS+88] CI Blauth, JV Arnold, WE Schulenberg, AC McCartney, and KM Taylor. Cerebral microembolism during cardiopulmonary bypass. retinal microvascular studies in vivo with fluorescein angiography. *The Journal of thoracic and cardiovascular surgery*, 95(4):668–676, 1988. 54

[BFL06] Y. Boykov and G. Funka-Lea. Graph cuts and efficient n-d image segmentation. *International Journal of Computer Vision*, 70(2):109–131, 2006. 101, 129, 131, 132, 133

[BGLR08] Yvonne Buys, Ivan Goldberg, George N Lambrou, and Robert Ritch. World glaucoma day, 6 march 2008: tackling glaucoma internationally. *Eye*, 2008. 44

[Bis07] Christopher M Bishop. Pattern recognition and machine learning (information science and statistics). 2007. 79, 81

[BJ01] Yuri Y Boykov and M-P Jolly. Interactive graph cuts for optimal boundary & region segmentation of objects in nd images. In *Computer Vision, 2001. ICCV 2001. Proceedings. Eighth IEEE International Conference on*, volume 1, pages 105–112. IEEE, 2001. 95, 144

[BLHH07] Boel Bengtsson, M Cristina Leske, Leslie Hyman, and Anders Heijl. Fluctuation of intraocular pressure and glaucoma progression in the early manifest glaucoma trial. *Ophthalmology*, 114(2):205–209, 2007. 46

[BMDC00] George H Bresnick, Dana B Mukamel, John C Dickinson, and David R Cole. A screening approach to the surveillance of patients with diabetes for the presence of vision-threatening retinopathy. *Ophthalmology*, 107(1):19–24, 2000. 25

[CA09] Muhammed Gökhan Cinsdikici and Doğan Aydın. Detection of blood vessels in ophthalmoscope images using mf/ant (matched filter/ant colony) algorithm. *Computer methods and programs in biomedicine*, 96(2):85–95, 2009. 86, 87, 108, 111

[CBM+08] Michael F Chiang, Michael V Boland, James W Margolis, Flora Lum, Michael D Abramoff, and P Lloyd Hildebrand. Adoption and perceptions of electronic health record systems by ophthalmologists: an american academy of ophthalmology survey. *Ophthalmology*, 115(9):1591–1597, 2008. 55

[CCK+89a] S Chaudhuri, S Chatterjee, N Katz, M Nelson, and M Goldbaum. Detection of blood vessels in retinal images using two-dimensional matched filters. *IEEE transactions on medical imaging*, 8(3):263–269, 1989. 85, 86, 87

[CCK+89b] Subhasis Chaudhuri, Shankar Chatterjee, Norman Katz, Mark Nelson, and Michael Goldbaum. Detection of blood vessels in retinal images using two-dimensional matched filters. *IEEE Transactions on medical imaging*, 8(3):263–269, 1989. 67, 105, 106, 107, 111

[CDV+90] Heang-Ping Chan, Kunio Doi, CARL J VYBRONY, Robert A Schmidt, Charles E Metz, Kwok Leung Lam, Toshihiro Ogura, Yuzheng Wu, and Heber MacMahon. Improvement in radiologists' detection of clustered microcalcifications on mammograms: The potential of computer-aided diagnosis. *Investigative radiology*, 25(10):1102–1110, 1990. 39

[CF03] T. Chanwimaluang and G. Fan. An efficient blood vessel detection algorithm for retinal images using local entropy thresholding. In *Circuits and Systems, 2003. ISCAS'03. Proceedings of the 2003 International Symposium on*, volume 5, pages V–21. IEEE, 2003. 82

[CFSP05] Delia Cabrera Fernández, Harry M Salinas, and Carmen A Puliafito. Automated detection of retinal layer structures on optical coherence tomography images. *Optics Express*, 13(25):10200–10216, 2005. 139

[CLN+10] Stephanie J Chiu, Xiao T Li, Peter Nicholas, Cynthia A Toth, Joseph A Izatt, and Sina Farsiu. Automatic segmentation of seven retinal layers in sdoct images congruent with expert manual segmentation. *Optics express*, 18(18):19413–19428, 2010. 140

[CLW+11] Jun Cheng, Jiang Liu, Damon Wing Kee Wong, Fengshou Yin, Carol Cheung, Mani Baskaran, Tin Aung, and Tien Yin Wong. Automatic

optic disc segmentation with peripapillary atrophy elimination. In *Engineering in Medicine and Biology Society, EMBC, 2011 Annual International Conference of the IEEE*, pages 6224–6227. IEEE, 2011. 119

[CLX+13] Jun Cheng, Jiang Liu, Yanwu Xu, Fengshou Yin, Damon Wing Kee Wong, Ngan-Meng Tan, Dacheng Tao, Ching-Yu Cheng, Tin Aung, and Tien Yin Wong. Superpixel classification based optic disc and optic cup segmentation for glaucoma screening. 2013. 23, 29, 113, 114

[CSMJ+06] Rogério A Costa, Mirian Skaf, Luiz AS Melo Jr, Daniela Calucci, Jose A Cardillo, Jarbas C Castro, David Huang, and Maciej Wojtkowski. Retinal assessment using optical coherence tomography. *Progress in retinal and eye research*, 25(3):325–353, 2006. 149

[CWB+07] Michael F Chiang, Lu Wang, Mihai Busuioc, Yunling E Du, Patrick Chan, Steven A Kane, Thomas C Lee, David J Weissgold, Audina M Berrocal, Osode Coki, et al. Telemedical retinopathy of prematurity diagnosis: accuracy, reliability, and image quality. *Archives of ophthalmology*, 125(11):1531–1538, 2007. 26

[CZK98] O Chutatape, Liu Zheng, and SM Krishnan. Retinal blood vessel detection and tracking by matched gaussian and kalman filters. In *Engineering in Medicine and Biology Society, 1998. Proceedings of the 20th Annual International Conference of the IEEE*, volume 6, pages 3144–3149. IEEE, 1998. 69

[DLR77] Arthur P Dempster, Nan M Laird, and Donald B Rubin. Maximum likelihood from incomplete data via the em algorithm. *Journal of the Royal Statistical Society. Series B (Methodological)*, pages 1–38, 1977. 71, 79

[Doi07] Kunio Doi. Computer-aided diagnosis in medical imaging: historical review, current status and future potential. *Computerized medical imaging and graphics*, 31(4-5):198–211, 2007. 38, 39

[Doi14] Kunio Doi. Current status and future potential of computer-aided diagnosis in medical imaging. 2014. 38, 39

[EGSEB11] Ahmed Elnakib, Georgy Gimel'farb, Jasjit S Suri, and Ayman El-Baz. Medical image segmentation: A brief survey. In *Multi Modality State-of-the-Art Medical Image Segmentation and Registration Methodologies*, pages 1–39. Springer, 2011. 23, 39

[EL99] A.A. Efros and T.K. Leung. Texture synthesis by non-parametric sampling. *In Proceedings of the ICCV*, pages 1033–1038, 1999. 123

[FCS+03] K Fritzsche, Ali Can, Hong Shen, C Tsai, J Turner, H Tanenbuam, C Stewart, Badrinath Roysam, JS Suri, and S Laxminarayan. Automated model based segmentation, tracing and analysis of retinal vasculature from digital fundus images. *State-of-The-Art Angiography, Applications and Plaque Imaging Using MR, CT, Ultrasound and X-rays*, pages 225–298, 2003. 23, 65, 67

[FGR04] Marco Foracchia, Enrico Grisan, and Alfredo Ruggeri. Detection of optic disc in retinal images by means of a geometrical model of vessel structure. *Medical Imaging, IEEE Transactions on*, 23(10):1189–1195, 2004. 28

[FHKEZ95] Adolph F Fercher, Ch K Hitzenberger, G Kamp, and Sy Y El-Zaiat. Measurement of intraocular distances by backscattering spectral interferometry. *Optics Communications*, 117(1):43–48, 1995. 137

[FMW88] AF Fercher, K Mengedoht, and W Werner. Eye-length measurement by interferometry with partially coherent light. *Optics letters*, 13(3):186–188, 1988. 56

[FOM+04] David S Friedman, BJ O'colmain, Beatriz Munoz, SC Tomany, Cathy McCarty, PT De Jong, B Nemesure, Paul Mitchell, and John Kempen. Prevalence of age-related macular degeneration in the united states. *Arch ophthalmol*, 122(4):564–572, 2004. 49

[FR05] A Foster and S Resnikoff. The impact of vision 2020 on global blindness. *Eye*, 19(10):1133–1135, 2005. 44

[FU01] Timothy W Freer and Michael J Ulissey. Screening mammography with computer-aided detection: Prospective study of 12,860 patients in a community breast center 1. *Radiology*, 220(3):781–786, 2001. 38, 39

[GAK+08] Mona Kathryn Garvin, Michael D Abràmoff, Randy Kardon, Stephen R Russell, Xiaodong Wu, and Milan Sonka. Intraretinal layer segmentation of macular optical coherence tomography images using optimal 3-d graph search. *Medical Imaging, IEEE Transactions on*, 27(10):1495–1505, 2008. 140

[GAW+09] Mona Kathryn Garvin, Michael D Abràmoff, Xiaodong Wu, Stephen R Russell, Trudy L Burns, and Milan Sonka. Automated 3-d intraretinal layer segmentation of macular spectral-domain optical coherence tomography images. *Medical Imaging, IEEE Transactions on*, 28(9):1436–1447, 2009. 140

[Gla13] Eye Website, Heartlands NHS, December 2013 2013. 13, 45

[GM96] M Giger and H MacMahon. Computer-aided diagnosis. *Radiologic Clinics of North America*, 34:565–596, 1996. 38

[GPG+04] Enrico Grisan, Alessandro Pesce, Alfredo Giani, Marco Foracchia, and Alfredo Ruggeri. A new tracking system for the robust extraction of retinal vessel structure. In *Engineering in Medicine and Biology Society,*

2004. IEMBS'04. 26th Annual International Conference of the IEEE, volume 1, pages 1620–1623. IEEE, 2004. 70

[GSC07] Saurabh Garg, Jayanthi Sivaswamy, and Siva Chandra. Unsupervised curvature-based retinal vessel segmentation. In *Biomedical Imaging: From Nano to Macro, 2007. ISBI 2007. 4th IEEE International Symposium on*, pages 344–347. IEEE, 2007. 86, 87, 107, 108, 111

[GSH+03] Viviane Guedes, Joel S Schuman, Ellen Hertzmark, Gadi Wollstein, Anthony Correnti, Ronald Mancini, David Lederer, Serineh Voskanian, Leonardo Velazquez, Helena M Pakter, et al. Optical coherence tomography measurement of macular and nerve fiber layer thickness in normal and glaucomatous human eyes. *Ophthalmology*, 110(1):177–189, 2003. 137

[GSP+02] Metin N Gurcan, Berkman Sahiner, Nicholas Petrick, Heang-Ping Chan, Ella A Kazerooni, Philip N Cascade, and Lubomir Hadjiiski. Lung nodule detection on thoracic computed tomography images: preliminary evaluation of a computer-aided diagnosis system. *Medical Physics*, 29(11):2552–2558, 2002. 38, 39

[GUFG+02] Francisco Gómez-Ulla, Maria I Fernandez, Francisco Gonzalez, Pablo Rey, Marta Rodriguez, Maria J Rodriguez-Cid, Felipe F Casanueva, Maria A Tome, Javier Garcia-Tobio, and Francisco Gude. Digital retinal images and teleophthalmology for detecting and grading diabetic retinopathy. *Diabetes Care*, 25(8):1384–1389, 2002. 25

[Gul10] A Gullstrand. Neue methoden der reflexlosen ophthalmoskopie. *Berichte Deutsche Ophthalmologische Gesellschaft*, 36, 1910. 54

[HBK+99] Larry D Hubbard, Rosemary J Brothers, William N King, Limin X Clegg, Ronald Klein, Lawton S Cooper, A Richey Sharrett, Matthew D

Davis, and Jianwen Cai. Methods for evaluation of retinal microvascular abnormalities associated with hypertension/sclerosis in the atherosclerosis risk in communities study. *Ophthalmology*, 106(12):2269–2280, 1999. 51

[Hei] Genop Healthcare, Heidelberg Spectralis 2013. 13, 55

[HG03] A. Hoover and M. Goldbaum. Locating the optic nerve in retinal image using the fuzzy convergence of the blood vessels. *IEEE Transactions on Medical Imaging*, 22(8):951–958, 2003. 112

[HIF+10] Hans-Martin Helb, Peter Charbel Issa, Monika Fleckenstein, Steffen Schmitz-Valckenberg, Hendrik PN Scholl, Carsten H Meyer, Nicole Eter, and Frank G Holz. Clinical evaluation of simultaneous confocal scanning laser ophthalmoscopy imaging combined with high-resolution, spectral-domain optical coherence tomography. *Acta ophthalmologica*, 88(8):842–849, 2010. 26

[HKG00] A Hoover, V Kouznetsova, and M Goldbaum. Locating blood vessels in retinal images by piecewise threshold probing of a matched filter response. *IEEE Transactions on Medical Imaging*, 19(3):203–210, 2000. 102, 104, 105, 106, 107, 110

[HKG02] AD Hoover, V Kouznetsova, and M Goldbaum. Locating blood vessels in retinal images by piecewise threshold probing of a matched filter response. *Medical Imaging, IEEE Transactions on*, 19(3):203–210, 2002. 65, 83, 84, 85, 86

[HLB+02] Anders Heijl, M Cristina Leske, Bo Bengtsson, Leslie Hyman, Boel Bengtsson, and Mohamed Hussein. Reduction of intraocular pressure and glaucoma progression: results from the early manifest glaucoma trial. *Archives of ophthalmology*, 120(10):1268–1279, 2002. 46

[HSKG13] Valma Harjutsalo, Reijo Sund, Mikael Knip, and Per-Henrik Groop. Incidence of type 1 diabetes in finland. *Jama*, 310(4):427–428, 2013. 47

[HSL+91] David Huang, Eric A Swanson, Charles P Lin, Joel S Schuman, William G Stinson, Warren Chang, Michael R Hee, Thomas Flotte, Kenton Gregory, Carmen A Puliafito, et al. Optical coherence tomography. *Science*, 254(5035):1178–1181, 1991. 56, 58, 59, 137

[ISW+05] Hiroshi Ishikawa, Daniel M Stein, Gadi Wollstein, Siobahn Beaton, James G Fujimoto, and Joel S Schuman. Macular segmentation with optical coherence tomography. *Investigative Ophthalmology & Visual Science*, 46(6):2012–2017, 2005. 139

[JC04] Glenn J Jaffe and Joseph Caprioli. Optical coherence tomography to detect and manage retinal disease and glaucoma. *American journal of ophthalmology*, 137(1):156–169, 2004. 56, 57, 58, 60

[JM03] Xiaoyi Jiang and Daniel Mojon. Adaptive local thresholding by verification-based multithreshold probing with application to vessel detection in retinal images. *Pattern Analysis and Machine Intelligence, IEEE Transactions on*, 25(1):131–137, 2003. 86, 87, 108, 111

[JSK11] G Joshi, Jayanthi Sivaswamy, and SR Krishnadas. Optic disk and cup segmentation from monocular color retinal images for glaucoma assessment. *Medical Imaging, IEEE Transactions on*, 30(6):1192–1205, 2011. 116, 117, 118, 119

[JSKK10] Gopal Datt Joshi, Jayanthi Sivaswamy, Kundun Karan, and SR Krishnadas. Optic disk and cup boundary detection using regional information. In *Biomedical Imaging: From Nano to Macro, 2010 IEEE International Symposium on*, pages 948–951. IEEE, 2010. 118, 119

[JWA03] Julien Jomier, David K Wallace, and Stephen R Aylward. Quantification of retinopathy of prematurity via vessel segmentation. In *Medical Image Computing and Computer-Assisted Intervention-MICCAI 2003*, pages 620–626. Springer, 2003. 28

[KB05] V. Kolmogorov and Y. Boykov. What metrics can be approximated by geo-cuts, or global optimization of length/area and flux. *In Proceedings of Tenth IEEE International Conference on Computer Vision, ICCV.*, 1:564–571, 2005. 97, 98, 99

[KBR01] Dara Koozekanani, Kim Boyer, and Cynthia Roberts. Retinal thickness measurements from optical coherence tomography using a markov boundary model. *Medical Imaging, IEEE Transactions on*, 20(9):900–916, 2001. 31, 32, 139

[KGG+81] OG Kolterman, RS Gray, J Griffin, P Burstein, J Insel, JA Scarlett, and JM Olefsky. Receptor and postreceptor defects contribute to the insulin resistance in noninsulin-dependent diabetes mellitus. *Journal of clinical investigation*, 68(4):957, 1981. 48

[KKK+07] T Kauppi, V Kalesnykiene, J Kamarainen, L Lensu, I Sorri, A Raninen, R Voitilainen, H Uusitalo, H Kalviainen, and J Pietila. Diaretdb1 diabetic retinopathy database and evaluation protocol. *In Proceedings of British Machine Vision Conference.*, 2007. 129

[KMFL92] James L Kinyoun, Donald C Martin, Wilfred Y Fujimoto, and Donna L Leonetti. Ophthalmoscopy versus fundus photographs for detecting and grading diabetic retinopathy. *Investigative ophthalmology & visual science*, 33(6):1888–1893, 1992. 25

[KS00] DAVID C Klonoff and DANIEL M Schwartz. An economic analysis of interventions for diabetes. *Diabetes care*, 23(3):390–404, 2000. 48

[KSGL+13] Djibril Kaba, Ana G Salazar-Gonzalez, Yongmin Li, Xiaohui Liu, and Ahmed Serag. Segmentation of retinal blood vessels using gaussian mixture models and expectation maximisation. In *Health Information Science*, pages 105–112. Springer, 2013. 85, 86, 105, 106, 111

[KXM+96] Takeshi Kobayashi, Xin-Wei Xu, Heber MacMahon, Charles E Metz, and Kunio Doi. Effect of a computer-aided diagnosis scheme on radiologists' performance in detection of lung nodules on radiographs. *Radiology*, 199(3):843–848, 1996. 38

[Las14] Nidek, The Art of Eye Care, Laser Ophthalmoscope 2014. 13, 55

[LBG01] Marc Lalonde, Mario Beaulieu, and Langis Gagnon. Fast and robust optic disc detection using pyramidal decomposition and hausdorff-based template matching. *Medical Imaging, IEEE Transactions on*, 20(11):1193–1200, 2001. 120

[LC03] Huiqi Li and Opas Chutatape. A model-based approach for automated feature extraction in fundus images. In *Computer Vision, 2003. Proceedings. Ninth IEEE International Conference on*, pages 394–399. IEEE, 2003. 29, 113, 117, 119

[LCS+13] Andrew Lang, Aaron Carass, Elias Sotirchos, Peter Calabresi, and Jerry L Prince. Segmentation of retinal oct images using a random forest classifier. In *SPIE Medical Imaging*, pages 86690R–86690R. International Society for Optics and Photonics, 2013. 153

[LHS+04] James Lowell, Andrew Hunter, David Steel, Ansu Basu, Robert Ryder, Eric Fletcher, and Lee Kennedy. Optic nerve head segmentation. *Medical Imaging, IEEE Transactions on*, 23(2):256–264, 2004. 117

[Lic76] PR Lichter. Variability of expert observers in evaluating the optic disc. *Transactions of the American Ophthalmological Society*, 74:532, 1976. 60

[LLS+05] Qiang Li, Feng Li, Kenji Suzuki, Junji Shiraishi, Hiroyuki Abe, Roger Engelmann, Yongkang Nie, Heber MacMahon, and Kunio Doi. Computer-aided diagnosis in thoracic ct. In *Seminars in Ultrasound, CT and MRI*, volume 26, pages 357–363. Elsevier, 2005. 39

[LMS+12] Laurence S Lim, Paul Mitchell, Johanna M Seddon, Frank G Holz, and Tien Y Wong. Age-related macular degeneration. *The Lancet*, 379(9827):1728–1738, 2012. 50

[LWMW08] Gerald Liew, Jie Jin Wang, Paul Mitchell, and Tien Y Wong. Retinal vascular imaging a new tool in microvascular disease research. *Circulation: Cardiovascular Imaging*, 1(2):156–161, 2008. 13, 15, 26, 48, 49, 52, 91

[Mac14] Sep 2014. 49, 50

[MAGAB11] Diego Marín, Arturo Aquino, Manuel Emilio Gegúndez-Arias, and José Manuel Bravo. A new supervised method for blood vessel segmentation in retinal images by using gray-level and moment invariants-based features. *Medical Imaging, IEEE Transactions on*, 30(1):146–158, 2011. 86, 87, 105, 106, 108, 109, 111

[MC06a] A. M. Mendonca and A. Campilho. Segmentation of retinal blood vessels by combining the detection of centerlines and morphological reconstruction. *IEEE Transactions on Medical Imaging*, 25(9):1200–1213, 2006. 104, 105, 106, 107, 108, 109, 111

[MC06b] Ana Maria Mendonça and Aurélio Campilho. Segmentation of retinal blood vessels by combining the detection of centerlines and morphological reconstruction. *IEEE Trans Med Imaging*, 25(9):1200–13, Sep 2006. 66, 84, 85, 86, 87

[MCC+05] Mircea Mujat, Raymond Chan, Barry Cense, B Park, Chulmin Joo, Taner Akkin, Teresa Chen, and Johannes de Boer. Retinal nerve fiber layer thickness map determined from optical coherence tomography images. *Optics Express*, 13(23):9480–9491, 2005. 139, 140

[MDC+90] Heber MacMahon, Kunio Doi, Heang-Ping Chan, Maryellen Lissak Giger, Shigehiko Katsuragawa, and Nobuyuki Nakamori. Computer-aided diagnosis in chest radiology. *Journal of thoracic imaging*, 5(1):67–76, 1990. 38

[MHMT10] Markus A Mayer, Joachim Hornegger, Christian Y Mardin, and Ralf P Tornow. Retinal nerve fiber layer segmentation on fd-oct scans of normal subjects and glaucoma patients. *Biomedical optics express*, 1(5):1358–1383, 2010. 31

[MHT99] François Mendels, Conor Heneghan, and Jean-Philippe Thiran. Identification of the optic disk boundary in retinal images using active contours. In *Proceedings of the Irish Machine Vision and Image Processing Conference*, pages 103–115. Citeseer, 1999. 116, 117, 119

[ML06] Colin D Mathers and Dejan Loncar. Projections of global mortality and burden of disease from 2002 to 2030. *PLoS medicine*, 3(11):e442, 2006. 51

[MMR+01] K Muller, Sebastian Mika, Gunnar Ratsch, Koji Tsuda, and Bernhard Scholkopf. An introduction to kernel-based learning algorithms. *Neural Networks, IEEE Transactions on*, 12(2):181–201, 2001. 147

[Moo14a] Moorfields Eye Hospital, NHS, Supports World Glaucoma 2014. 44

[moo14b] Moorfields Eye Hospital, NHS 2014. 50

[MPHT+07a] M. E. Martinez-Perez, A. D. Hughes, S. A. Thom, A. A. Bharath, and K. H. Parker. Segmentation of blood vessels from red-free and fluorescein retinal images. *Medical image analysis*, 11(1):47–61, 2007. 68, 105, 106, 108, 111

[MPHT+07b] M. Elena Martinez-Perez, Alun D. Hughes, Simon A. Thom, Anil A. Bharath, and Kim H. Parker. Segmentation of blood vessels from red-free and fluorescein retinal images. *Medical Image Analysis*, 11(1):47 – 61, 2007. 85, 86, 87

[MPLK11] Shlomo Melmed, Kenneth S Polonsky, P Reed Larsen, and Henry M Kronenberg. *Williams textbook of endocrinology: Expert consult*. Elsevier Health Sciences, 2011. 48

[MPN+11] Shanthi Mendis, Pekka Puska, Bo Norrving, et al. *Global atlas on cardiovascular disease prevention and control*. World Health Organization, 2011. 51

[MS89] David Mumford and Jayant Shah. Optimal approximations by piecewise smooth functions and associated variational problems. *Communications on pure and applied mathematics*, 42(5):577–685, 1989. 118

[MS93] Ayyakkannu Manivannan and PF Sharp. Digital fundus imaging using a scanning laser ophthalmoscope. *Physiological measurement*, 14(1):43, 1993. 54

[MZB+05] Felipe A Medeiros, Linda M Zangwill, Christopher Bowd, Roberto M Vessani, Remo Susanna Jr, and Robert N Weinreb. Evaluation of retinal nerve fiber layer, optic nerve head, and macular thickness measurements for glaucoma detection using optical coherence tomography. *American journal of ophthalmology*, 139(1):44–55, 2005. 60

[NASC14] Eddie YK Ng, U Rajendra Acharya, Jasjit S Suri, and Aurelio Campilho. *Image Analysis and Modeling in Ophthalmology*. CRC Press, 2014. 25

[NAVG07] Meindert Niemeijer, Michael D Abràmoff, and Bram Van Ginneken. Segmentation of the optic disc, macula and vascular arch in fundus photographs. *Medical Imaging, IEEE Transactions on*, 26(1):116–127, 2007. 133

[NPS08] Jorge Novo, Manuel G Penedo, and J Santos. Optic disc segmentation by means of ga-optimized topological active nets. In *Image Analysis and Recognition*, pages 807–816. Springer, 2008. 117

[NSvG+04] Meindert Niemeijer, Joes Staal, Bram van Ginneken, Marco Loog, and Michael D Abramoff. Comparative study of retinal vessel segmentation methods on a new publicly available database. In *Medical Imaging 2004*, pages 648–656. International Society for Optics and Photonics, 2004. 70, 107, 108, 109

[NVT+13] Jelena Novosel, Koen A Vermeer, Gijs Thepass, Hans G Lemij, and Lucas J van Vliet. Loosely coupled level sets for retinal layer segmentation in optical coherence tomography. In *Biomedical Imaging (ISBI), 2013 IEEE 10th International Symposium on*, pages 1010–1013. IEEE, 2013. 139, 140, 155

[Ocu14] Ted Montgomery, Ocular Pathology Photos 1998-2014. 13, 49

[OKS+82] JERROLD M Olefsky, ORVILLE G Kolterman, JOHN A Scarlett, et al. Insulin action and resistance in obesity and noninsulin-dependent type ii diabetes mellitus. *Am J Physiol*, 243(1):E15–E30, 1982. 48

[OMTM02] Alireza Osareh, Majid Mirmehdi, Barry Thomas, and Richard Markham. Colour morphology and snakes for optic disc localisation. In *The*

6th medical image understanding and analysis conference, pages 21–24. BMVA Press, 2002. 117, 119

[Org06] World Health Organization. *Prevention of blindness from diabetes mellitus: report of a WHO consultation in Geneva, Switzerland, 9-11 November 2005*. World Health Organization, 2006. 48

[Oys99] Clyde W Oyster. *The human eye: structure and function*. Sinauer Associates, 1999. 112

[PAM+06] Niall Patton, Tariq M Aslam, Thomas MacGillivray, Ian J Deary, Baljean Dhillon, Robert H Eikelboom, Kanagasingam Yogesan, and Ian J Constable. Retinal image analysis: concepts, applications and potential. *Progress in retinal and eye research*, 25(1):99–127, 2006. 52

[Pod14] A Gh Podoleanu. Optical coherence tomography. 2014. 56

[PP93] Nikhil R Pal and Sankar K Pal. A review on image segmentation techniques. *Pattern recognition*, 26(9):1277–1294, 1993. 23, 39

[PR14] Enea Poletti and Alfredo Ruggeri. Graph search retinal vessel tracking. *Ophthalmological Imaging and Applications*, page 97, 2014. 69

[PRCC07] Renzo Perfetti, Elisa Ricci, Daniele Casali, and Giovanni Costantini. Cellular neural networks with virtual template expansion for retinal vessel segmentation. *Circuits and Systems II: Express Briefs, IEEE Transactions on*, 54(2):141–145, 2007. 86, 87, 107, 108

[QAG82] Harry A Quigley, Earl M Addicks, and W Richard Green. Optic nerve damage in human glaucoma: Iii. quantitative correlation of nerve fiber loss and visual field defect in glaucoma, ischemic neuropathy, papilledema, and toxic neuropathy. *Archives of Ophthalmology*, 100(1):135–146, 1982. 46

[QB06] Harry A Quigley and Aimee T Broman. The number of people with glaucoma worldwide in 2010 and 2020. *British Journal of Ophthalmology*, 90(3):262–267, 2006. 44, 46

[QL05] Jing Qin and Denis HY Leung. A semiparametric two-component "compound" mixture model and its application to estimating malaria attributable fractions. *Biometrics*, 61(2):456–464, 2005. 78

[RBDO76] Gerald M Reaven, Robert Bernstein, Bonnie Davis, and Jerrold M Olefsky. Nonketotic diabetes mellitus: insulin deficiency or insulin resistance? *The American journal of medicine*, 60(1):80–88, 1976. 48

[RHdC04] Neil Ryan, Conor Heneghan, and Philip de Chazal. Registration of digital retinal images using landmark correspondence by expectation maximization. *Image and Vision Computing*, 22(11):883–898, 2004. 28

[Rie00] Stephen J Riederer. Current technical development of magnetic resonance imaging. *Engineering in Medicine and Biology Magazine, IEEE*, 19(5):34–41, 2000. 56

[RP07] Elisa Ricci and Renzo Perfetti. Retinal blood vessel segmentation using line operators and support vector classification. *Medical Imaging, IEEE Transactions on*, 26(10):1357–1365, 2007. 108, 109, 111

[SAN+04a] Joes Staal, Michael Abràmoff, Meindert Niemeijer, Max Viergever, and Bram van Ginneken. Ridge-based vessel segmentation in color images of the retina. *IEEE transactions on medical imaging*, 23(4):501–509, 2004. 66, 83, 84, 85, 86, 87

[SAN+04b] Joes Staal, Michael D Abràmoff, Meindert Niemeijer, Max A Viergever, and Bram van Ginneken. Ridge-based vessel segmentation in color images of the retina. *IEEE Transactions on Medical Imaging*, 23(4):501–509, 2004. 102, 104, 105, 106, 107, 108, 109, 111, 129

[SBCW99] Chanjira Sinthanayothin, James F Boyce, Helen L Cook, and Thomas H Williamson. Automated localisation of the optic disc, fovea, and retinal blood vessels from digital colour fundus images. *British Journal of Ophthalmology*, 83(8):902–910, 1999. 112

[Sch14] OCT RESEARCH AT OBEL, INTRODUCTION TO OCT 2014. 14, 57

[Sco10] Scott Anthony, Review of Optometry, Jobson Medical Information 2010. 12, 17, 31, 140, 141

[SGLK12] Ana Salazar-Gonzalez, Yongmin Li, and Djibril Kaba. Mrf reconstruction of retinal images for the optic disc segmentation, 2012. 74

[SHA+95] Joel S Schuman, Michael R Hee, Adarsh V Arya, Tamar Pedut-Kloizman, Carmen A Puliafito, James G Fujimoto, and Eric A Swanson. Optical coherence tomography: a new tool for glaucoma diagnosis. *Current opinion in ophthalmology*, 6(2):89–95, 1995. 59, 137

[SIL+93] Eric A Swanson, JA Izatt, CP Lin, JG Fujimoto, JS Schuman, MR Hee, D Huang, and CA Puliafito. In vivo retinal imaging by optical coherence tomography. *Optics letters*, 18(21):1864–1866, 1993. 56

[SLC+06a] J. Soares, J. Leandro, R. Cesar, H. Jelinek, and M. Cree. Retinal vessel segmentation using the 2-d gabor wavelet and supervised classification. *IEEE Transactions on Medical Imaging*, 25(9):1214–1222, 2006. 66

[SLC+06b] Joao VB Soares, Jorge JG Leandro, Roberto M Cesar, Herbert F Jelinek, and Michael J Cree. Retinal vessel segmentation using the 2-d gabor wavelet and supervised classification. *Medical Imaging, IEEE Transactions on*, 25(9):1214–1222, 2006. 105, 106, 107, 108, 109, 111

[SLF+06] Richard F Spaide, Ketan Laud, Howard F Fine, JR JAMES M KLANCNIK, Catherine B Meyerle, Lawrence A Yannuzzi, John Sorenson, Jason

Slakter, Yale L Fisher, and Michael J Cooney. Intravitreal bevacizumab treatment of choroidal neovascularization secondary to age-related macular degeneration. *Retina*, 26(4):383–390, 2006. 50

[SLS+05] Kenji Suzuki, Feng Li, Shusuke Sone, et al. Computer-aided diagnostic scheme for distinction between benign and malignant nodules in thoracic low-dose ct by use of massive training artificial neural network. *Medical Imaging, IEEE Transactions on*, 24(9):1138–1150, 2005. 39

[SMA11] Mohamed Ben Salah, Amar Mitiche, and Ismail Ben Ayed. Multiregion image segmentation by parametric kernel graph cuts. *Image Processing, IEEE Transactions on*, 20(2):545–557, 2011. 140, 142, 143, 147

[SQY+08] Alison H Skalet, Graham E Quinn, Gui-Shuang Ying, Luz Gordillo, Luz Dodobara, Ken Cocker, Alistair R Fielder, Anna L Ells, Monte D Mills, Clare Wilson, et al. Telemedicine screening for retinopathy of prematurity in developing countries using digital retinal images: a feasibility project. *Journal of American Association for Pediatric Ophthalmology and Strabismus*, 12(3):252–258, 2008. 52

[SSPF07] Gabor Mark Somfai, Harry M Salinas, Carmen A Puliafito, and Delia Cabrera Fernandez. Evaluation of potential image acquisition pitfalls during optical coherence tomography and their influence on retinal image segmentation. *Journal of biomedical optics*, 12(4):041209–041209, 2007. 32

[SXY99] Joseph M Schmitt, SH Xiang, and Kin M Yung. Speckle in optical coherence tomography. *Journal of biomedical optics*, 4(1):95–105, 1999. 32

[SZE98] JG Sled, AP Zijdenbos, and AC Evans. A nonparametric method for automatic correction of intensity nonuniformity in mri data. *IEEE Transactions on Medical Imaging*, 17(1):87–97, 1998. 72, 73

[TAC+10a] Nicholas Tustison, Brian Avants, Philip Cook, Yuanjie Zheng, Alexander Egan, Paul Yushkevich, and James Gee. N4itk: Improved n3 bias correction. *IEEE Transactions on Medical Imaging*, 29(6):1310–1320, 2010. 71, 72

[TAC+10b] Nicholas J Tustison, Brian B Avants, Philip A Cook, Yuanjie Zheng, Alexander Egan, Paul A Yushkevich, and James C Gee. N4itk: improved n3 bias correction. *Medical Imaging, IEEE Transactions on*, 29(6):1310–1320, 2010. 140, 142

[TLvFG06] Yandong Tang, Xiaomao Li, Axel von Freyberg, and Gert Goch. Automatic segmentation of the papilla in a fundus image based on the cv model and a shape restraint. In *Pattern Recognition, 2006. ICPR 2006. 18th International Conference on*, volume 1, pages 183–186. IEEE, 2006. 118

[TLW+10] Ngan Meng Tan, Jiang Liu, Damon WK Wong, Zhuo Zhang, Shijian Lu, Joo Hwee Lim, Huiqi Li, and Tien Yin Wong. Classification of left and right eye retinal images. In *SPIE Medical Imaging*, pages 762438–762438. International Society for Optics and Photonics, 2010. 113

[TNPD95] B Thylefors, AD Negrel, Ramachandra Pararajasegaram, and KY Dadzie. Global data on blindness. *Bulletin of the World Health Organization*, 73(1):115, 1995. 44

[Top14] EMS, Topcon TRC-NW8 Non-Mydriatic Retinal Camera (Pre-Owned) 2014. 13, 55

[VGtHRV01] Bram Van Ginneken, Bart M ter Haar Romeny, and Max A Viergever. Computer-aided diagnosis in chest radiography: a survey. *Medical Imaging, IEEE Transactions on*, 20(12):1228–1241, 2001. 38

[VKR08] S. Vicente, V. Kolmogorov, and C. Rother. Graph cut based image segmentation with connectivity priors. *In Proceedings of IEEE Conference on Computer Vision and Pattern Recognition, CVPR*, 1:1–8, 2008. 97

[Vol14] Keelep Eye Shop, Volk Pictor, imaging unlimited 2014. 13, 55

[VSS92] Rohit Varma, William C Steinmann, and Ingrid U Scott. Expert agreement in evaluating the optic disc for glaucoma. *Ophthalmology*, 99(2):215–221, 1992. 60

[WHO14] World Health Organisation, Cardiovascular diseases (CVDs) 2014. 50

[wik14a] Wikipedia Eye Anatomy 2014. 13, 40

[Wik14b] Wikipedia Eye Anatomy, Retina 2014. 13, 42

[WLK+02] Maciej Wojtkowski, Rainer Leitgeb, Andrzej Kowalczyk, Adolf F Fercher, and Tomasz Bajraszewski. In vivo human retinal imaging by fourier domain optical coherence tomography. *Journal of biomedical optics*, 7(3):457–463, 2002. 59, 137

[WLL+08] DWK Wong, J Liu, JH Lim, X Jia, F Yin, H Li, and TY Wong. Level-set based automatic cup-to-disc ratio determination using retinal fundus images in argali. In *Engineering in Medicine and Biology Society, 2008. EMBS 2008. 30th Annual International Conference of the IEEE*, pages 2266–2269. IEEE, 2008. 117

[WLT+10] DWK Wong, J Liu, NM Tan, F Yin, BH Lee, and TY Wong. Learning-based approach for the automatic detection of the optic disc in digital retinal fundus photographs. In *Engineering in Medicine and Biology*

Society (EMBC), 2010 Annual International Conference of the IEEE, pages 5355–5358. IEEE, 2010. 113, 115

[WRG+04] Sarah Wild, Gojka Roglic, Anders Green, Richard Sicree, and Hilary King. Global prevalence of diabetes estimates for the year 2000 and projections for 2030. *Diabetes care*, 27(5):1047–1053, 2004. 47

[WSK+04] Tien Yin Wong, Anoop Shankar, Ronald Klein, Barbara EK Klein, and Larry D Hubbard. Prospective cohort study of retinal vessel diameters and risk of hypertension. *bmj*, 329(7457):79, 2004. 51

[WSK+10] D. Welfer, J. Scharcanski, C. Kitamura, M. Dal Pizzol, L. Ludwig, and D. Marinho. Segmentation of the optic disc in color eye fundus images using an adaptive morphological approach. *Computers in Biology and Medicine*, 40(1):124–137, 2010. 34, 121, 129, 131, 132, 133

[WWH+06] Nicholas Witt, Tien Y Wong, Alun D Hughes, Nish Chaturvedi, Barbara E Klein, Richard Evans, Mary McNamara, Simon A McG Thom, and Ronald Klein. Abnormalities of retinal microvascular structure and risk of mortality from ischemic heart disease and stroke. *Hypertension*, 47(5):975–981, 2006. 52

[WZL06] D. Wu, M. Zhang, and J. Liu. On the adaptive detection of blood vessels in retinal images. *IEEE Transactions on Biomedical Engineering*, 53(2):341–343, 2006. 93

[XCS+07] Juan Xu, Opas Chutatape, Eric Sung, Ce Zheng, and Paul Chew Tec Kuan. Optic disk feature extraction via modified deformable model technique for glaucoma analysis. *Pattern recognition*, 40(7):2063–2076, 2007. 118

[XL10] Lili Xu and Shuqian Luo. A novel method for blood vessel detection from retinal images. *Biomedical engineering online*, 9(1):14, 2010. 68

[XPP00] Chenyang Xu, Dzung L Pham, and Jerry L Prince. Image segmentation using deformable models. *Handbook of medical imaging*, 2:129–174, 2000. 116

[YBT10] Jing Yuan, Egil Bae, and Xue-Cheng Tai. A study on continuous max-flow and min-cut approaches. In *Computer Vision and Pattern Recognition (CVPR), 2010 IEEE Conference on*, pages 2217–2224. IEEE, 2010. 142, 143, 145, 148

[YHSS11] Azadeh Yazdanpanah, Ghassan Hamarneh, Benjamin R Smith, and Marinko V Sarunic. Segmentation of intra-retinal layers from optical coherence tomography images using an active contour approach. *Medical Imaging, IEEE Transactions on*, 30(2):484–496, 2011. 139, 140

[ZCS+10] Haogang Zhu, David P Crabb, Patricio G Schlottmann, Tuan Ho, and David F Garway-Heath. Floatingcanvas: quantification of 3d retinal structures from spectral-domain optical coherence tomography. *Optics express*, 18(24):24595–24610, 2010. 139, 140

[Zim92] Paul Z Zimmet. Kelly west lecture 1991 challenges in diabetes epidemiology—from west to the rest. *Diabetes care*, 15(2):232–252, 1992. 48

[ZK01] Frederic Zana and J-C Klein. Segmentation of vessel-like patterns using mathematical morphology and curvature evaluation. *Image Processing, IEEE Transactions on*, 10(7):1010–1019, 2001. 67, 86, 87, 107, 108, 111

[ZRSC94] Liang Zhou, Mark S Rzeszotarski, Lawrence J Singerman, and Jeanne M Chokreff. The detection and quantification of retinopathy using digital angiograms. *Medical Imaging, IEEE Transactions on*, 13(4):619–626, 1994. 69

[ZSCP08] Y. Zeng, D. Samaras, W. Chen, and Q. Peng. Topology cuts: a novel min-cut/max-flow algorithm for topology preserving segmentation in n-d images. *Journal of computer vision and image understanding.*, 112(1):81–90, 2008. 129, 131, 132, 133

[ZZM+02] Ran Zeimer, Shazhou Zou, Torre Meeder, Kevin Quinn, and Susan Vitale. A fundus camera dedicated to the screening of diabetic retinopathy in the primary-care physician's office. *Investigative ophthalmology & visual science*, 43(5):1581–1587, 2002. 52

[ZZZK10] Bob Zhang, Lin Zhang, Lei Zhang, and Fakhri Karray. Retinal vessel extraction by matched filter with first-order derivative of gaussian. *Computers in biology and medicine*, 40(4):438–445, 2010. 85, 86, 87, 105, 106, 107, 108, 111